UNIVERSITY OF IOANNINA

DEPARTMENT OF PHYSICS

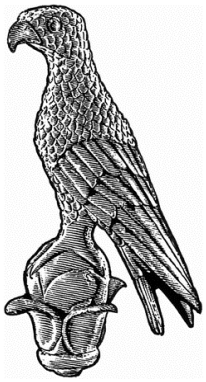

DEVELOPMENT OF DIGITALLY-CONTROLED HIGH-TEMPERATURE ELECTRON-PARAMAGNETIC-RESONANCE (EPR) SPECTROMETER

LOUKAS BELLES

MASTER'S IN STUDIES OF MODERN ELECTRONIC TECHNOLOGIES

SUPERVISOR: PROFESSOR YIANNIS DELIGIANNAKIS

IOANNINA
DECEMBER 2021

ΠΑΝΕΠΙΣΤΗΜΙΟ ΙΩΑΝΝΙΝΩΝ

ΤΜΗΜΑ ΦΥΣΙΚΗΣ

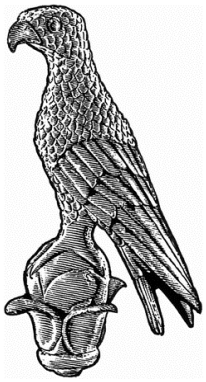

ΑΝΑΠΤΥΞΗ ΨΗΦΙΑΚΑ-ΕΛΕΓΧΟΜΕΝΟΥ ΦΑΣΜΑΤΟΜΕΤΡΟΥ ΗΛΕΚΤΡΟΝΙΚΟΥ-ΠΑΡΑΜΑΓΝΗΤΙΚΟΥ-ΣΥΝΤΟΝΙΣΜΟΥ (EPR) ΥΨΗΛΩΝ ΘΕΡΜΟΚΡΑΣΙΩΝ

ΛΟΥΚΑΣ ΜΠΕΛΛΕΣ

ΠΜΣ ΣΤΙΣ ΣΥΓΧΡΟΝΕΣ ΗΛΕΚΤΡΟΝΙΚΕΣ ΤΕΧΝΟΛΟΓΙΕΣ

ΕΠΙΒΛΕΠΩΝ: ΚΑΘΗΓΗΤΗΣ ΙΩΑΝΝΗΣ ΔΕΛΗΓΙΑΝΝΑΚΗΣ

ΙΩΑΝΝΙΝΑ

ΔΕΚΕΜΒΡΙΟΣ 2021

Abstract

This thesis describes a new digitally-controlled High-Temperature Electron-Paramagnetic-Resonance (H.T. EPR) spectrometer. While introducing microwave radiation at 9.4GHz range with subsequent sinusoidal modulation, the magnetic field range is up to 800mT (8000G) the High Temperature Cavity has a wide range of temperature from room temperature up to 1300K with the help of a flowing gas. Furthermore, the method of extracting the steady-state absorption spectra and the meaning of lineshape spectra is well explained and the change of the lineshape and linewidth in many systems. In that thesis three experiments are presented which can show and connect all the theory of lineshape. The fist experiment was at DPPH a radical with S=1/2 (which gave all the necessary information about S/N, the lock-in amplifier, the signal channel and the microwave bridge). The second experiment was at natural marble with S=5/2, I=5/2, which has Mn^{+2} (isolated spins) in the matrix of $CaO/CaCO_3$ which was the first one that carried out at high temperatures. The last experiment that carried out had to do with magnetic nanoparticles Fe_2O_3, those particles were measured up to 800K, they can give information about systems with spin domains such as the one we measured. Such systems of superparamagnetic nanoparticles are currently investigated by a large variety of techniques. Through that technique we can study and get information about the lattice in a faster way and especially for information about magnetic nanoparticles.

Περίληψη

Η παρούσα διατριβή περιγράφει ένα νέο ψηφιακά ελεγχόμενο φασματόμετρο Ηλεκτρονίου-Παραμαγνητικού Συντονισμού Υψηλών Θερμοκρασιών (Υ.Θ. Η.Π.Σ.). Εισάγοντας την ακτινοβολία μικροκυμάτων με συχνότητα 9,4 GHz με επακόλουθη ημιτονοειδή διαμόρφωση, σε εύρος μαγνητικού πεδίου έως και 800 mT (8000 G) και χρησιμοποιώντας κοιλότητα υψηλών θερμοκρασιών καταφέραμε μπορούμε να μετρήσουμε σε θερμοκρασιακό εύρος από θερμοκρασία δωματίου έως 1300 K. Επιπλέον, εξηγείται η έννοια των φασμάτων ως προς τον τύπο της απορρόφησης και η αλλαγή του σχήματος της γραμμής σε πολλά συστήματα. Σε αυτή τη διατριβή παρουσιάζονται τρία πειράματα. ΣΤο πρώτο πείραμα μετρήθηκε DPPH μια ρίζα με S=1/2 (που έδωσε όλες τις απαραίτητες πληροφορίες για το S/N, τον ενισχυτή, το κανάλι σήματος και τη γέφυρα μικροκυμάτων). Το δεύτερο πείραμα ήταν σε φυσικό μάρμαρο με S=5/2, I=5/2, το οποίο έχει Mn+2 (απομονωμένα σπιν) στη μήτρα του μαρμάρου (CaO/CaCO3) που ήταν το πρώτο που πραγματοποιήθηκε σε υψηλές θερμοκρασίες. Το τελευταίο πείραμα υψηλών θερμοκρασιών που πραγματοποιήθηκε είχε να κάνει με μαγνητικά νανοσωματίδια Fe2O3, μπορούν να δώσουν πληροφορίες για συστήματα με ομάδες από σπιν όπως αυτό που μετρήσαμε. Τέτοια συστήματα υπερπαραμαγνητικών νανοσωματιδίων διερευνώνται επί του παρόντος με μια μεγάλη ποικιλία τεχνικών. Μέσω αυτής της τεχνικής μπορούμε να μελετήσουμε και να πάρουμε πληροφορίες για το πλέγμα με πιο γρήγορο τρόπο και ειδικά για πληροφορίες σχετικά με τα μαγνητικά νανοσωματίδια.

Acknowledgements

This Master Thesis has been accomplished with the support of many individuals. I would like to thank and express my gratitude to my supervisor, Professor Yiannis Deligiannakis, Head of the Lab of Physical Chemistry of Materials and Environment for his flawless trust, deep knowledge, incessant assistance and support. His enthusiasm and our conversations inspired me and helped me in multiple ways all the time of research and writing this thesis.

Except my supervisor, I would like to thank Professor Vasilis Christofilakis for all his support on many embellishments and his concern all the time of my master. Also I would like to thank Professor Nikolaos Manthos for his willing to help in multiple ways.

Besides, my supervisor I would like to offer my special thanks to PhD candidate Areti Zindrou for her assistance and especially her support since my first day in the lab. And for all the conversations about Flame Spray Pyrolysis or photocatalytic systems or other projects that she specially knows and for the trust that she shows to me in multiple things. But mostly for her belief in me all that time.

I am also very grateful for the assistance given by PhD candidate Constantinos Moularas, for his advises on many projects that we shared all that time, for his friendship and especially for his patience of teaching me some details of the FSP world.

Moreover, I would like to thank Dr. Panagiota Stathi and ex-member Dr. Yiannis Georgiou for all the advice that they offered me from the very first day and for all the help particularly in the field of chemistry.

I am also very thankful to all the other members of our lab group for creating a friendly working environment and for their understanding of my stressful schedule.

My acknowledgment would be incomplete without having the support of my family. My parents Ipatia and Christos always support me and believe in me. They always supported me, and I do not think that they will ever stop even if they don’t understand

exactly what I am doing here. But their unconditional love, trust and enthusiasm are the ingredients of my strength.

CHAPTER 1

1. Electron Paramagnetic Resonance

1.1 Introduction

Nowadays much of the knowledge of the structure of molecules has been obtained from the analysis of molecular absorption spectra. Such spectra are obtained by measuring the attenuation versus frequency (or wavelength) of a beam of electromagnetic radiation as it passes through a sample of matter. Lines or bands in a spectrum represent transitions between energy levels of the absorbing species. The frequency of each line or band measures the energy separation of two levels.

When a photon is absorbed or emitted by an electron, atom or molecule, the energy and angular momentum of the combined (total) system must be conserved. For this reason, the propagation direction relative to the alignments of the photoactive chemical system is of crucial importance.

In 1921, Stern and Gerlach observed that a beam of silver atoms splits into two lines when it is subjected to a magnetic field [1]–[3]. While the line splitting in optical spectra, first found by Zeeman in 1896 [4], [5] could be explained by the angular momentum of the electrons, the s-electron of silver could not be subject to such a momentum, not to mention that an azimuthal quantum number $l = ½$ cannot be explained by classical physics. At that time, quantum mechanics was still an emerging field in physics and it took another three years until the anormal Zeeman effect was correctly interpreted by the joint research of Uhlenbeck, a classical physicist, and Goudsmit, a fellow of Paul Ehrenfest [6], [7]. They postulated a so-called ‘spin’, a quantized angular momentum, as an intrinsic property of the electron. This research marks the cornerstone of electron paramagnetic resonance (EPR) spectroscopy which is based on the transitions between quantized states of the resulting magnetic moment.

In the hydrogen atom, one has additional angular momentum arising from the proton nucleus. Breit and Rabi [8] described the resultant energy levels of a hydrogen atom in a magnetic field in 1931. Rabi et al [9]. studied transitions between levels induced by an oscillating magnetic field. This experiment was the first observation of magnetic resonance.

Cynically, the worst event in the twentieth century ultimately boosted the development of EPR spectroscopy as after World War II suitable microwave instrumentation was readily available from existing in radar equipment. This led to the observation of the first EPR spectrum (Figure 1) by the Russian physicist Zavoisky in 1944 [10], [11] , who discovered the phenomenon of EPR in the condensed phase. He studied aqueous and non-aqueous solutions of manganese salts using the radio-frequency field and checking the coefficient of paramagnetic absorption as a function of the applied static magnetic field. The curves he obtained showed a maximum of absorption1 in the region of weak fields (Figure 1). Under higher frequencies for the radio-frequency field, this maximum shifted toward the region of higher fields, already one year before the first nuclear magnetic resonance (NMR) spectrum was recorded [12]·[13]. More specifically the first observation of an electron paramagnetic resonance peak was made in 1945 when Zavoisky [14] detected a radiofrequency absorption line from a $CuCl_2 \cdot 2H_2O$ sample. He found a resonance at a magnetic field of 4.76mT for a frequency of 133 MHz; in this case the electron Zeeman g-factor is approximately 2. Zavoisky's results were interpreted by Frenkel [15] as showing paramagnetic resonance absorption. Later experiments at higher (microwave) frequencies in magnetic field of 100-300 mT (1000-3000G) showed the advantages of the use of high frequencies and fields.

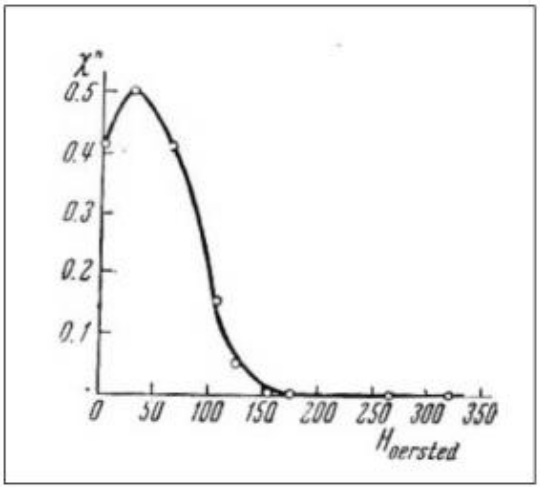

Figure 1: First EPR signal obtained for a solution of manganese chloride tetrahydrate in absolute methyl alcohol at the concentration 0.175 g/cm3 and room temperature.

The development of EPR and NMR went in the same pace during the first decade though NMR was by far more widely used. But in 1965, NMR spectroscopy experienced its final boost with the development of the much faster Fourier transform (FT) NMR technique which also opened the development of completely new methodologies in this field [16]. The corresponding pulse EPR spectroscopy suffered from expensive instrumentation, the lack of microwave components, sufficiently fast digital electronics and intrinsic problems of limited microwave power. Although the first pulse EPR experiment was reported by Blume already in 1958 [17], pulse EPR was conducted by only a small number of research groups over several decades.

In the 1980s, the required equipment became cheaper and manageable and the first commercial pulse EPR spectrometer was released to the market, followed only ten years later by the first commercial high field spectrometer [[18]]. This development of equipment promoted the invention of new and the advancement of already existing methods. Nowadays, a vast EPR playground is accessible to an ever-growing research community, which became as versatile as the spectroscopic technique itself.

While NMR is a standard spectroscopic technique for the structural determination of molecules, the closely related EPR spectroscopy is still sparsely known by many scientists. This discrepancy originates from the lack of naturally occurring paramagnetic systems because the formation of a chemical bond is inherently coupled to the pairing of electrons and a resulting overall electron spin of $S = 0$.

This lack of EPR-active materials is both the biggest disadvantage and the biggest advantage of the method. On the one hand, the method is restricted to few existing paramagnetic systems, radicals and transition metal complexes with a residual electron spin. On the other hand, this selectivity turns out advantageous in the study of complex materials, since only few paramagnetic species lead to interpretable EPR spectra.

Since most materials are diamagnetic, paramagnetic species must be artificially introduced as tracer molecules. Dependent on the manner of introduction, they are called spin labels or spin probes [19]. While spin labels are covalently attached to the system of interest, no chemical linkage is formed between spin probes and the material. In both cases, the tracer molecules are sensitive to

their local surrounding in terms of structure and dynamics and thus allow an indirect molecular observation of the material's properties [20].

Additionally, dipole–dipole couplings between two electrons allow for distance measurements in the highly relevant range of 1.5–8 nm [21],[22]. Attached to selected sites in biological and synthetic macromolecules, structural information of such complex materials becomes accessible [22]–[24]. This approach turns out especially powerful if the systems under investigation lack long -range order and scattering methods cannot be applied for structural analysis. Magnetic resonance techniques as intrinsically local methods do not require this constraint and EPR as one of only few methods allows for the structural characterization of these amorphous nanoscopic samples with a high selectivity and sensitivity [25], [26].

The EPR is wide known, because it's a spectrometry that can give information in plenty systems of many research fields such as physics (isolated atoms[27], atoms in fullerenes[28], transition metal ions[29], magnetic material[30]) chemistry (organic molecules[31], radicals[32]), biology(radicals in biological materials[33], metal centers in enzymes[34], metalloproteins[34]), medicine[35], food industry (radiation dosimetry[35], antioxidant properties of food[36]) and materials (degradation of materials[37]). All those systems, for reasons that are well explained in the second chapter of this thesis, are measured in low temperatures[38](4K or 77K). The temperature at an EPR spectrum suggests the spin dynamics of the measured sample. There are plenty models, like Curie, Raman, Orbach with each one of them explaining the dependence of the temperature with the lattice and the time relaxation. The High Temperature EPR is not so famous among the researchers. It is known that there are many EPR spectrometers all around the world but many few (~1/100) of High Temperature EPR which are less than 10 in all Europe and less than 10 in US. They can provide though very important information in explaining the role of defects in nanoparticles and ferromagnetic particles. The H.T. isn't used for biological systems yet or chemical systems until now because there they can't provide a lot, but it is a good technique to measure a system at a specific and stable temperature, below melting point, so there is a potential use for biological systems to be measured up to 360K or a chemical system up to 380K or at carbon -based materials to be measured up to 600K. There are many ways of increasing the temperature at a sample, i.e. one can increase it with the use of a laser (laser-heated H.T. EPR [39]) by decreasing the pressure (H.T. High Vacuum Pressure Transmitter EPR) or simply by adding a resistor in an

enclosed environment and by that way heat the sample. The scope of this thesis is to develop a digitally controlled spectrometer like the last one, more specifically, by using an X-band EPR set up and by adjusting it digitally with a temperature controlling unit (controller) and a high-power supply unit (source) on a tungsten filament in an enclosed environment we achieved to develop a flexible method of conducting in-situ heating EPR experiments, through LabVIEW, in all the range of temperatures. In that thesis three series of pilot experiments are presented which can show and connect all the theory of line shape, more specifically we measured a radical, a marble which is a system of isolated spins and ferromagnetic materials which has spin domains. The fist experiment was at DPPH a radical with S=1/2 (which gave all the necessary information about S/N, the lock-in amplifier, the signal channel and the microwave bridge). The second pilot experiment was at natural marble, which has Mn^{+2} in the matrix of $CaO/CaCO_3$, which is a system of isolated spins in the matrix. The last experiment that carried out was on magnetic nanoparticles Fe_2O_3, those particles were measured up to 800K. Such systems of superparamagnetic nanoparticles are currently investigated by a large variety of techniques. Through that technique we can study and get information about the lattice in a faster way and especially for information about magnetic nanoparticles.

Overall electron paramagnetic resonance is a potent and complicated method of investigating various materials and spin dynamics. There are many methods of conducting experiments, each one requiring highly sophisticated machines and deep knowledge to understand the observed phenomena. For the sake of simplicity, we now describe two general EPR techniques and give short descriptive introduction into the principles of the experiments. This section is by no means intended as a thorough description or division of the many various techniques and experiments used in the EPR field; it is rather intended as a soft introduction to the two specific aspects of EPR closely related to the high temperature EPR technology.

Continuous wave EPR

In continuous wave experiments (abbreviated as CW) the sample is put inside a magnet and the field is swept in such a slow manner that it can be considered steady. The microwave radiation is kept on a constant frequency (thus continuous wave) and after propagating through the optical path excites the spin system if the resonance condition is met. To improve the signal-to-noise ratio, a

low magnitude fast-oscillating external magnetic field is usually added to the main field. This is called" modulation" and causes the detection of a first derivative of the EPR lines. Not only this significantly improves the S/N ratio, but also allows the observer to be able to evaluate the spectra more easily.

This technique is used mainly as an analysis of a given material on a molecular level understanding intra-molecular phenomena such as the g-tensor anisotropy, hyperfine splitting or exchange interaction and the inter-molecular phenomena, such as dipolar coupling. No phenomena related to relaxation can be directly observed.

Pulsed EPR

The general principles of pulsed techniques in EPR are keeping the external field constant and administering a high-power, short microwave pulse to the spin system. In case of a specific (so-called 90◦) pulse, the magnetization M is completely flipped from z-direction to xy-plane, from where it then relaxes back to the z-direction while processing about the z-axis with Larmor frequency. The resulting trajectory of the magnetization vector was first observed in nuclear magnetic resonance by inserting a detection coil into the xy-plane and reading out the voltage induced by the nuclear magnetization vector movement; this is depicted in Figure 2. The curve depicted in fig.2.8 is called the free induction decay (FID). It generally follows a formula

Eq.1

where ω_s is the Larmor frequency, t denotes the time variable and T_2 is the spin-spin (transversal) relaxation time. The first term describes a circular precession about the z-axis.

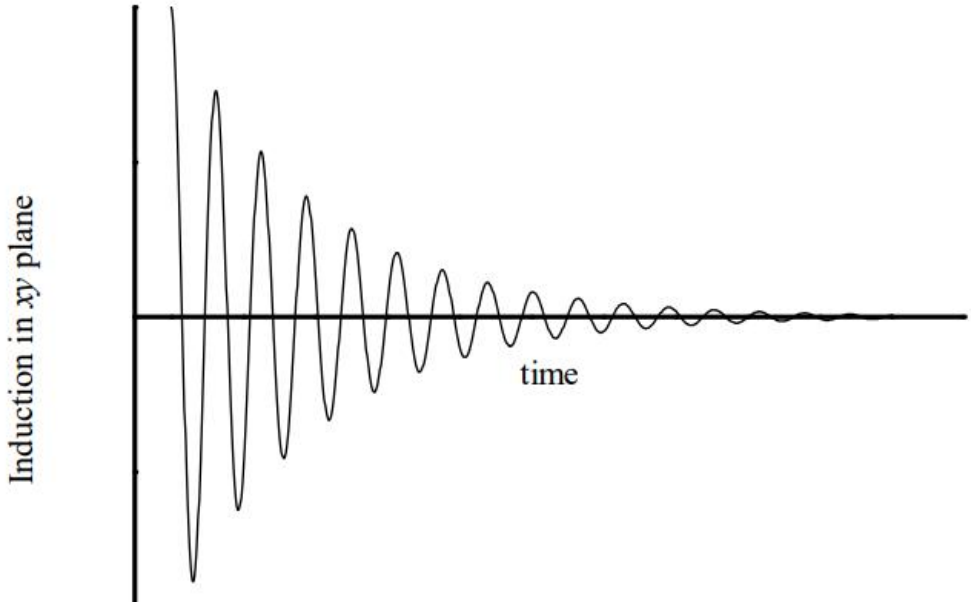

Figure 2: Observable relaxation of xy magnetization Mxy after a pulsed excitation. The exponential decay is proportional to T2. At first observed in nuclear magnetic resonance by inserting a detection coil into the xy-plane.

The pulsed techniques are generally highly demanding on instrumentation. The introduction of a resonant cavity precisely tuned to the specific frequency used is necessary, which brings a size limitation to the sample; at 10 GHz, $\lambda = 3$ cm, while at 300 GHz, $\lambda = 1$ mm. Also, a high-power microwave pulse source is required, which technologically limits the frequency range where the experiment can be conducted.

In both ways Microwave absorption occurs by varying the magnetic field in a limited range around a central value B_0, and the EPR spectrum in most cases consists of many absorption lines. The following main parameters and features characterize the spectrum: the positions of the absorptions, which are the magnetic field values at which the absorptions take place; the number, separation, and relative intensity of the lines; and their widths and shapes. All of these parameters and features are related to the structure of the species responsible for the spectrum, to their interactions with the environment, and to the dynamic processes in which the species are involved.

1.2 General Theory of EPR

1.2.1 Resonance Condition

Since energies are quantized, and a single unpaired electron has only two allowed energy states. It has a state of lower energy when the moment of the electron, μ, is aligned with the magnetic field and a higher energy state when m is aligned against the magnetic field as shown in Figure 3.
An electron in an atomic orbit carries an orbital angular momentum due to its motion about the nucleus. Associated with this angular momentum is an orbital magnetic dipole moment $\boldsymbol{\mu}_L$ proportional to the orbital angular momentum, which is denoted by **L**, in a manner,

Eq.2

where μ_B is the Bohr magneton, given by:

Eq. 3

where me is the electron mass.
The electron also possesses an intrinsic mechanical angular momentum called the electron spin. The two states are designated by the projection of the electron spin, m_s, on the direction of the magnetic field. Because the electron is a spin 1/2 particle, the parallel state has $m_s = -1/2$ and the antiparallel state has $m_s = +1/2$. As shown in Figure 3 The difference between energies of the two states (state 2 – state 1) caused by the interaction between the electron spin and the magnetic field B_0 which is explained from quantum mechanics Equation 2,3.

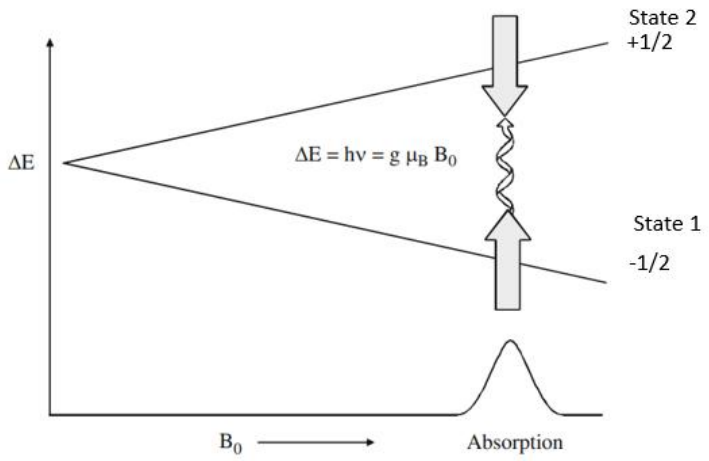

Figure 3: While magnetic field is scanned, the energies of the two spin states of an unpaired electron diverge. At the magnetic field for which the energy difference between the two electron spin states is equal to hv for the spectrometer, there is absorption of energy by the spins, which is called resonance.

These two states, which are the projection of the electron spin, differ only in the orientation of the angular momentum in space and not in the magnitude. Postulate of quantum mechanics states that definite components of the spin can be determined only in a specific axis. This means that the two spin states can be in only one axis usually around z-axis. At the absence of interactions between the electron spin with its environment, any choice for the direction in space of the z-axis is allowed. The electrons spin randomly, and the two states have the same energy; they are degenerate[40]. The electron spin angular momentum is associated with the magnetic moment by the formula:

Eq.4

where is Bohr's magneton and is the Lande factor or simply the g-factor. The energy of a magnetic moment when a constant magnetic field is applied is given by the scalar product between the magnetic moment and the magnetic field . The total magnetic dipole momentum is then

Eq.5

In atomic systems angular momenta (Equation 5) are quantized. The spin angular momentum obeys (Equation 6):

Eq.6

where S is the spin quantum number. Then the magnetic spin quantum number m_S in general follows mS = −S, (−S + 1), ..., +S. An electron has S = 1/2, therefore it can inhabit states given by magnetic quantum numbers of values $m_S = \pm 1/2$.

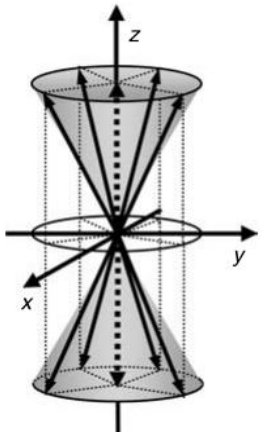

Figure 4: The electron spin angular momentum is a vector represented in the figure as a solid arrow, whose length is $|\boldsymbol{S}|=\sqrt{(3/4)}$. According to quantum mechanics, when a Cartesian frame x, y, z is chosen, only a component of the spin vector (usually assumed as the z component) has a definite value S_z of either 1/2 or -1/2 .

The energy of a magnetic dipole in a static magnetic field $\mathbf{B}_0$ oriented along the z-axis, where $\mathbf{B}_0 = (0, 0, B_0)$ is (Equation 7)

Eq.7

If a nucleus has simultaneously even number of protons and even number of neutrons, it has no spin value. In other cases, it has a spin and the same principles as for the electron spin apply. Generally, the nuclei can possess spin numbers ***I*** of integer or half-integer values, and consequently the magnetic spin quantum numbers are $m_I = -I, -I+1, ..., +I$. This will be useful later when we discuss hyperfine splitting.

1.2.2 The Zeeman Effect

The Zeeman effect[41] describes splitting of energy levels of electrons with energies E_2 and E_1 as shown in Equation 8 and nuclei induced by a static external magnetic field. The energy difference between two spin states is

Eq. 8

from which the fundamental equation of paramagnetic resonance, the resonance condition, is produced. This equation states that a photon can excite the spin of an electron into a higher energy state if its energy equals the energy gap (Equation 9) between the two states:

Eq. 9

Spin comes along the z-axis as discussed earlier and therefore the scalar product reduces to a single term if the magnetic field is applied into z-direction. This reads as:

Eq. 10

Since spin (=1/2) has two states $m_S = +1/2$ or ($\uparrow$) and $m_S = -1/2$ or ($\downarrow$) by substituting in Equation 10, we take the following expression:

Eq. 11

and

Eq.12

where $g_e \approx 2$ is Lande splitting factor, μ_B is Bohr magneton ($\mu_B = 9.2732 \times 10^{-21}$ erg·gauss^{-1}) and B_0 the applied magnetic field, the energies of the spin states diverge linearly as the magnetic field increases and the energy difference depends linearly on the magnetic field. But when the magnetic field is zero the two spin states have the same energy hence there is no energy difference. As can be seen from the equation 3 the same result could happen changing the frequencies, the two spin states can be varied by changing the magnetic field strength, there are two potential approaches to

obtaining spectra. The magnetic field could be held constant while the frequency of the electromagnetic radiation is scanned.

Absorption of energy occurs when the magnetic field "tunes" the two spin states such that the energy difference matches the energy of the applied radiation. This field is called the "field for resonance". Because of difficulties in scanning microwave frequencies and because of the use of a resonant cavity for signal detection, most EPR spectrometers operate at constant microwave frequency and scan the magnetic field. As shown in Figure 5 before the applied magnetic field the $m_s=\pm 1/2$ is at the same energy but when we apply magnetic field we have the difference of energies which means that the absorption and the emission are equal and the populations of states in each level of energy are going to be equal at the limit but one population in the order of 10^{-3} (1 out of 1000) at the lower level is going to be stable because of relaxation phenomena.

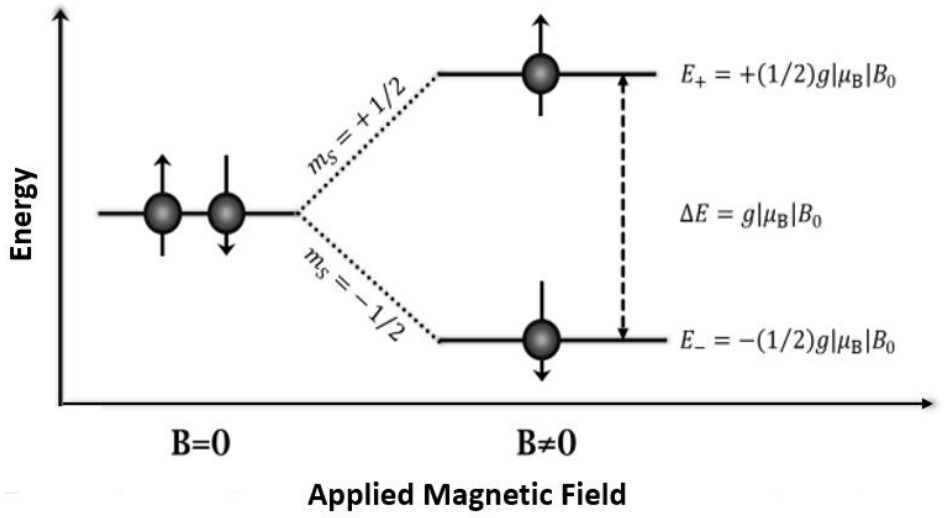

Figure 5: Splitting energy levels with the appliance of magnetic field.

The spectrum as we will see in next chapter is plotted as the first derivative of the absorption versus the magnetic field. The parameter used as a fingerprint for each molecule would be the g-factor since it's the only factor that can remain constant at different frequencies and magnetic fields.

It helps distinguish and identify types of samples. Using the g-factor expression is very useful which is:

Eq.13

The g-factor is independent from the frequency *v* e.g. for a free electron the g factor is equal with 2.0023 no matter which frequency is used, and for that reason at EPR spectroscopy the g-factor is more used than the magnetic field of resonance. For a system like that with 9GHz as a microwave frequency the magnetic field resonate at approximately 3300 Gauss. In some complex systems the real magnetic field at the paramagnetic center isn't necessarily the externally applied static magnetic field **B**. Usually there are local field $\mathbf{B_{local}}$, which are added to the **B** as shown in Figure 6 and so the magnetic field that interacts with the paramagnetic center is the $\mathbf{B_{eff}}$ and its equal with:

$$\mathbf{B_{eff}} = \mathbf{B_{res}} + \mathbf{B_{local}} \qquad \text{Eq.14}$$

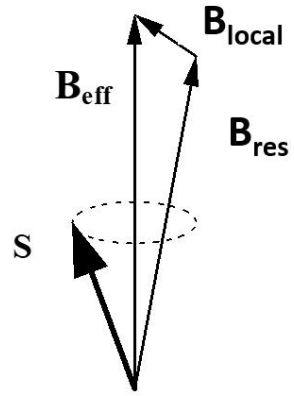

*Figure 6: All the local magnetic fields $\boldsymbol{B_{local}}$ are added to the externally applied magnetic field **B**, which interacts with the spin **S**.*

In the case of resonance:

$$g_e\, B_{eff}\, \beta_e = hv$$

$$* \qquad g_e\, (B_{res}+B_{local})\, \beta_e = hv \qquad *$$

Eq.15

At the real EPR experiment we record the intensity of the external magnetic field where resonance is happening (Equation 15), so the determinant g-factor (Equation 16) is the one which is calculated by the:

Eq.16

The understanding of the origin and calculation of local field sizes is one of the main tasks in EPR spectroscopy[42]. These fields mainly come from:

- the orbital torque
- the field of substituents in metal complexes
- interactions with nuclear spins
- interactions between neighboring paramagnetic centers.

In systems with an unpaired electron, such as organic radicals, the local fields are usually very small and therefore the g_{eff} value for organic radicals remains close to 2. In contrast with metals where local fields can be very strong, and usually come from the orbital torque and the effect of substituents (ligand field). Values of g_{eff} in metals can deviate greatly from the value g = 2 e.g., values g_{eff} = 9.2 and g_{eff} = 1.6 are typical for high spin Fe^{3+} triple iron (S = 5/2) and iron-sulfur centers (Fe-S).

1.3 The EPR Spectrum

As I mentioned earlier at the EPR experiment we record the intensity of the absorption of the microwaves at a frequency ν (Y-axis) versus the intensity of the external magnetic field (X-axis)

and absorbance of the energy exists only when the splitting of the energy levels is equal with the energy of the microwaves hv as shown in Figure 7.

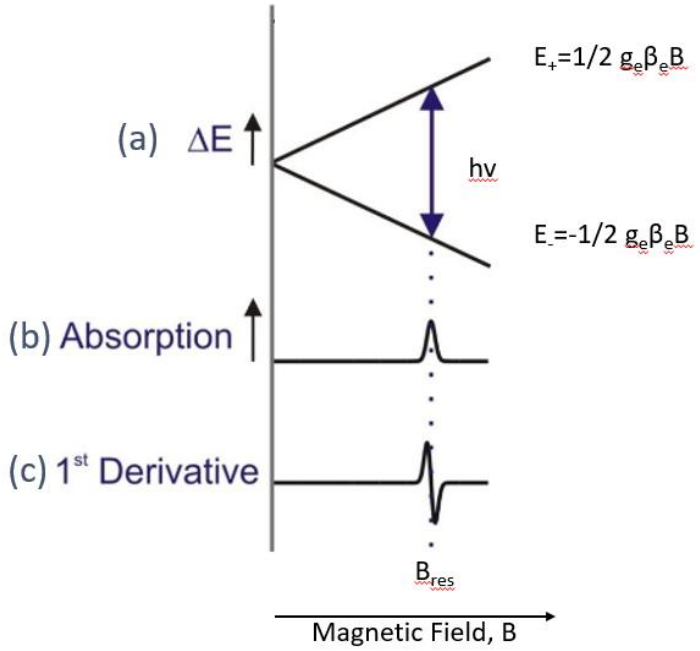

Figure 7: The EPR spectrum records the intensity of microwave absorption as a function of the external magnetic field. (a) In the simplified, ideal case the absorption is monochromatic. However, in real systems the absorption line widens (b) and absorption occurs for a field distribution. The main causes of 'widening' are interactions with adjacent spins, and the heterogeneity of the environment of paramagnetic centers. (c) Due to the modulation application, 'modulation', when the signal is detected, the first derivative of the signal is finally recorded (b).

Firstly, the two spin states have the same energy in the absence of a magnetic field. Secondly, the energies of the spin states diverge linearly as the magnetic field increases. These two facts have important consequences for spectroscopy:

1) Without a magnetic field, there is no energy difference to measure.
2) The measured energy difference depends linearly on the magnetic field.

Because we can change the energy differences between the two spin states by varying the magnetic field strength, we have an alternative means to obtain spectra. A radiation source for radar waves

produces only a very limited spectral region. In EPR such a source is called a klystron. A so-called X-band klystron has a spectral band width of about 8.8-9.6 GHz. This makes it impossible to continuously vary the wavelength similarly to optical spectroscopy. It is therefore necessary to vary the magnetic field, until the quantum of the radar waves fits between the field-induced energy levels.

On a practical level, this absorption gives a faint signal that usually coexists with random 'noise'. The signal we are interested in is selectively amplified through (a) suitable amplifiers and (b) the 'field modulation' technique, where a small additional oscillating magnetic field is applied to the external magnetic field at a typical frequency of 100 kHz. By detecting the peak-to-peak amplitude the first derivative of the absorption is measured. By using phase sensitive detection only signals with the same modulation (100 kHz) are detected. This results in higher signal to noise ratios. Note field modulation is unique to continuous wave EPR measurements and spectra resulting from pulsed experiments are presented as absorption profiles.

It should be noted that the application of the configuration for the detection of EPR signals results in the eventual recording of the first derivative of the signal, Figure 7c, and not the absorption, Figure 7b. The resonant field is easily located from the zero point of the derivative intensity. The EPR absorption signal in this CW is a Lorentzian function, which represents the shape of the EPR resonance line.

1.3.1 Isotropic Hyperfine Interaction in EPR Spectrums

Many elements of the periodic table have stable isotopes with non-zero nuclear spin ***I*** e.g. ^{1}H (I=½), ^{14}N (I=1), ^{19}F (I= ½), $^{63,65}Cu$ (I=3/2), ^{51}V (I= 7/2) ... As an example of the effect of nuclear spin on EPR spectra we will consider the energy levels of a system with electronic and nuclear spin

S= ½ and I= ½ respectively. The interaction between the electron spin S and the nuclear spin I leads to the decomposition of each of the energy levels of S into 2I +1= 2*1/2+1= 2 levels. The relative energies and contributions of each magnetic interaction as shown below and in Figure 8 are:

$E_{\uparrow, m_I=+½}$ =	$+½g_e \beta_e B$	$- ½g_\nu \beta_\nu B$	$+ ¼ A_{iso}$
$E_{\uparrow, m_I=-½}$ =	$+½g_e \beta_e B$	$+ ½g_\nu \beta_\nu B$	$- ¼ A_{iso}$
$E_{\downarrow, m_I=-½}$ =	$-½g_e \beta_e B$	$+ ½g_\nu \beta_\nu B$	$+ ¼ A_{iso}$
$E_{\downarrow, m_I=+½}$ =	$-½g_e \beta_e B$	$- ½g_\nu \beta_\nu B$	$- ¼ A_{iso}$
	Zeeman Electronic	**Zeeman Nuclear**	**Hyperfine Interaction**

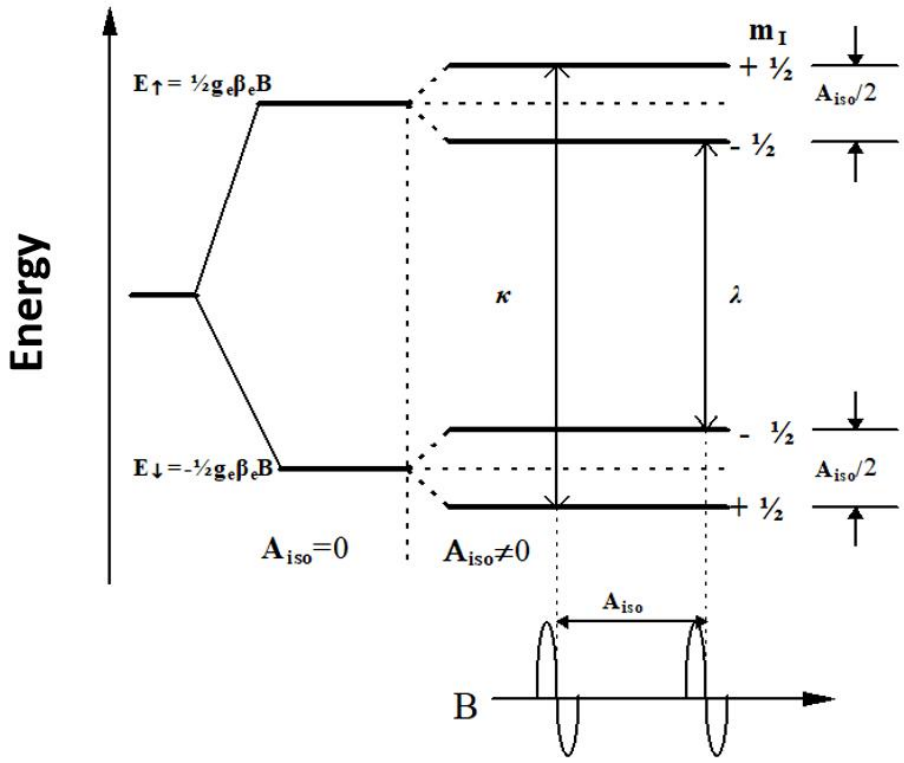

Figure 8: System energy levels with an unpaired electron S = ½ and nuclear spin I = ½. (e.g. hydrogen vapor), in the presence of a strong external magnetic field B. The isotropic ultra-fine interaction is A_{iso}. The

two permissible transitions λ and κ connect states $\Delta_{ms} = \pm 1$, $\Delta_{mI} = 0$ and occur in magnetic fields B κ, $\lambda = h\nu/g_\beta \pm A_{iso}/2$. The distance between the two peaks in the EPR spectrum is equal to A_{iso}.

The "Zeeman Electronic" and "Zeeman Nuclear" terms are used to describe the interaction of the applied magnetic field B with the magnetic dipole moments of electronic and nuclear spin respectively. The interaction between electronic and nuclear spin, which is called Hyperfine Interaction and it's defined by the size of the parameter of A_{iso}. The permissible EPR transfers are determined by the selection rules as shown in Equations 17a and 17b:

$$\Delta m_s = \pm 1 \qquad \text{Eq. 17a}$$

$$\Delta m_I = 0 \qquad \text{Eq. 17b}$$

According to all above the permissible transitions have energies:

$$(E\uparrow, m_I=+½) - (E\downarrow, m_I=+½) = h\nu = g_e \beta_e B + ½A_{iso} \quad \text{(transition } \kappa\text{)} \qquad \text{Eq. 18a}$$

$$(E\uparrow, m_I=-½) - (E\downarrow, m_I=-½) = h\nu = g_e \beta_e B - ½A_{iso} \quad \text{(transition } \lambda\text{)} \qquad \text{Eq. 18b}$$

And the corresponding fields of resonant are:

$$B_\kappa = h\nu/g_e \beta_e + A_{iso}/2g_e\beta_e \quad \text{(transition } \kappa\text{)} \qquad \text{Eq. 19a}$$

$$B_\lambda = h\nu/g_e \beta_e - A_{iso}/2g_e\beta_e \quad \text{(transition } \lambda\text{)} \qquad \text{Eq. 19b}$$

I.e. the EPR Spectrum is characterized by two symmetrical signals which are far apart $A_{iso}/g_e\beta_e$ in magnetic field units (Gauss) and when its expressed at units of energy the hyperfine split of the two signals is equal to A_{iso}.

When there is a second equivalent nucleus (with the same nuclear spin $I_2 = ½$ and the same A_{iso}) interacts with the S and then every one of the four new states is splitting by $A_{iso}/2$ as shown in Figure 9. The final states are characterized by the *total nuclear spin* which is the result of the combination of I_1 and I_2 as:

$I_{συνολικό} = I_1 + I_2 = 1$

M_I	m_{I1}	m_{I2}
+1	+1/2	+1/2
0	+1/2	-1/2
-1	-1/2	-1/2

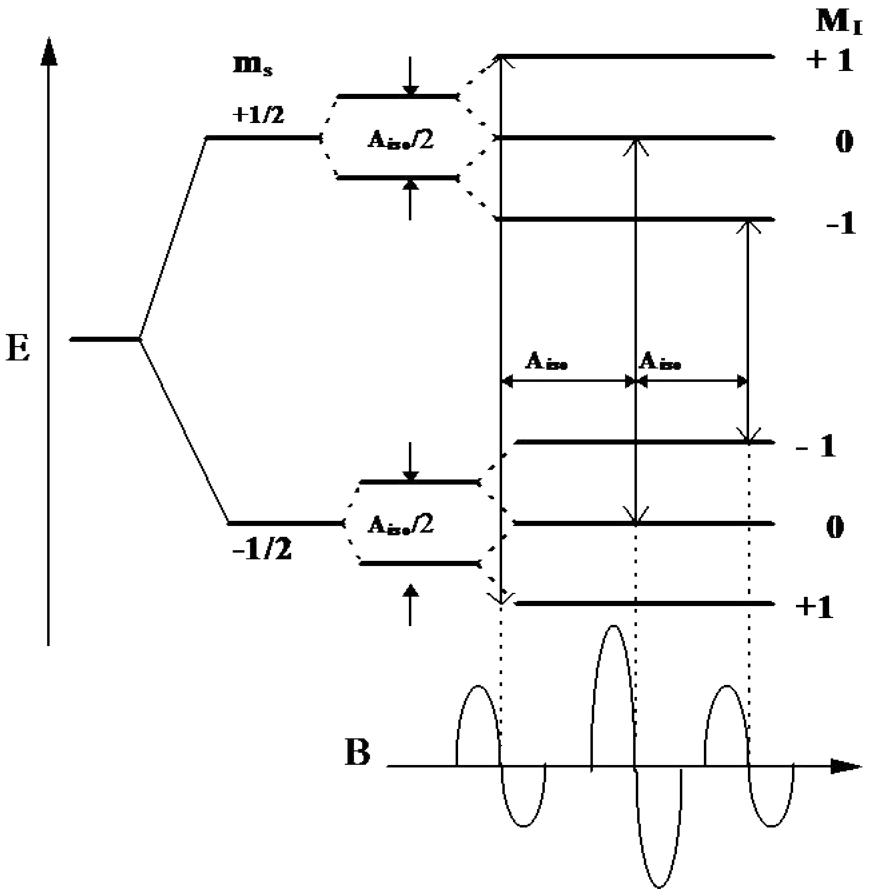

Figure 9: Energy levels and transitions for S = ½ with one or two equivalent nuclei I = ½. The EPR signal consists of three peaks. The states MI = 0 are doubly degenerate and therefore the transition signal 0 ↔ 0 has twice the intensity of +1 ↔ +1, -1 ↔ -1.

As shown in Figure 9 in the case of the two nuclear spins there is a double degeneration of the stations with MI = 0, for both m_s. Due to this double degeneration the middle peak (M_I= 0) in the

EPR spectrum has twice the intensity of M_I= + 1 and M_I= -1. For N equivalent spin I_i=1/2, with ΣI_i=I, the EPR spectrum will include 2I+1 peaks with relative intensities given by the coefficients of the binomial expansion $(1+x)^N$ (Pascal's triangle) [43] as shown in Table 1.

Nuclei Number	Number of lines at EPR spectrum	Relative Intensities
0	1	1
1	2	1 1
2	3	1 2 1
3	4	1 3 3 1
4	5	1 4 6 4 1
5	6	1 5 10 10 5 1
…	…	…

Table 1: A table which shows the nuclei number versus the number of lines that we will see in an EPR spectrum and their relative intensities which are given by the binomial expansion $(1+x)^N$, Pascal's triangle.

1.3.2 Anisotropy at EPR spectrum

The cases that been examined till now were about systems in which the interactions of the electronic spin with the environment are isotropic. With that term is meant that the interactions that determine the resonance fields, and therefore the spectrum, are independent of the direction of external B with respect to the axes of symmetry of the system. On the other hand, in many systems, especially in the solid state, these interactions are anisotropic. Typical cases of anisotropy are those of g-factor and hyperfine interaction.

Zeeman anisotropy refers to the phenomenon in which energy levels depend on the orientation of the external magnetic field B with respect to the axes of symmetry of the paramagnetic center. As a result of this anisotropy, for a paramagnetic center the value of the resonance field changes depending on the orientation of B. If for example B in the orientation of x-axis is bigger than in the orientation of z-axis a similar EPR spectrum as shown in Figure 10 will be shown.

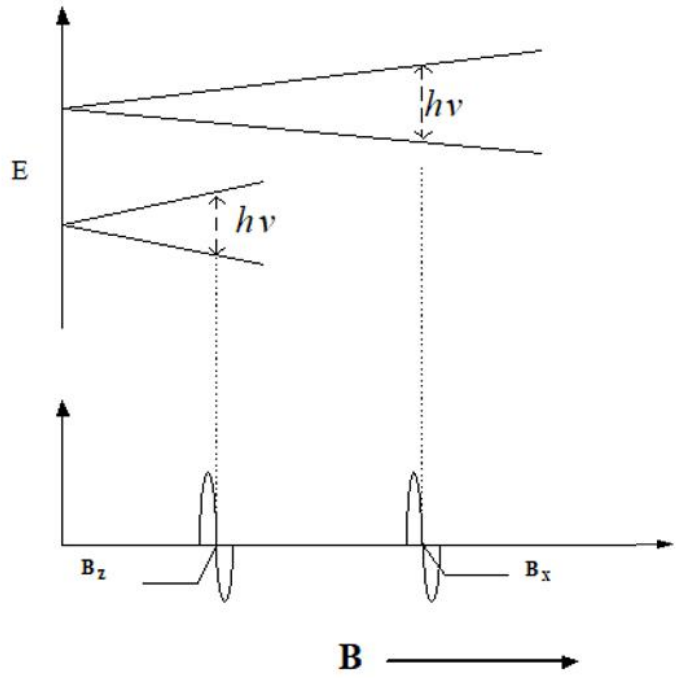

Figure 10: Zeeman anisotropy: Energy levels of the system act differently for two characteristic addresses of B, i.e. for $B_x > B_z$ the peaks are varied accordingly of the orientation of the resonant field.

In the case where for the three directions X, Y, Z three different fields of resonance $B_X \neq B_Y \neq B_Z$ are recorded, then the Zeeman anisotropy is characterized as 'rhombic'. When for the two addresses e.g. $B_X = B_Y \neq B_Z$, the resonance fields coincide, Zeeman anisotropy is characterized as 'axial', while in the 'isotropic' case only one resonance field $B_X = B_Y = B_Z$ is recorded [43]. Since molecules are oriented in space, mixing them would make the analysis direction dependent. This is expressed in observable parameters with the anisotropy of the g-factor. The g-factor has a set of

principal axis system labeled as $_x$, $_y$ and $_z$. Depending on the values of the g-factor we have different line shapes in an EPR spectrum as shown in Figure 11.

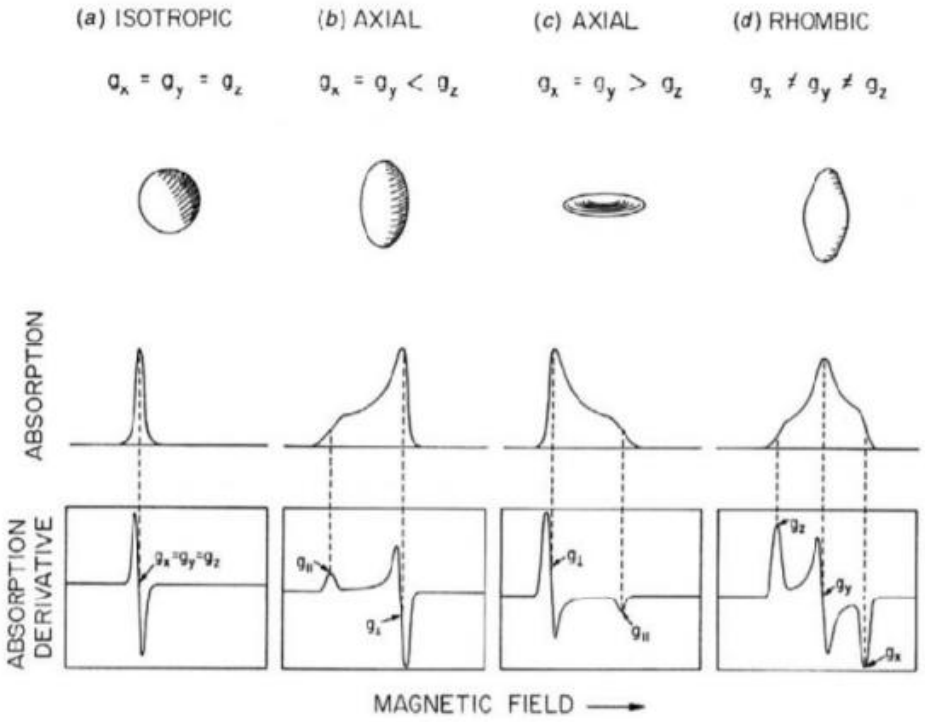

Figure 11: Schematic representation of g-tensor and the corresponding absorption and EPR spectra. Depending on the g-values we have different classes of anisotropy. Equal g-values in 3 directions results in isotropic g-factor (a). An axial class has one component different than the others (b,c) . The rhombic class has g-tensor with different components in 3 directions (d). [40]

In cases such as the solid sample or the icy solution, the paramagnetic centers have random orientations in space. In this case the EPR spectrum comes from paramagnetic centers for which the external magnetic field B, statistically has all possible directions. Such an EPR spectrum is called a 'dust spectrum'.

At the case of a system with Zeeman anisotropy at the dust spectrum the tunings for all possible B are recorded. In the case of axial symmetry ($B_X = B_Y \neq B_Z$), all the centers for which B is anywhere on the XY plane have the same resonance field, $B_\perp = B_X = B_Y$, as shown in Figure 12a. The centers where B//Z are statistically less than the centers contributing to the $B_\perp$. A continuous distribution of EPR signal intensities is observed in intermediate orientations of B. In fact, the recorded EPR spectrum is the outline of all absorptions, as the dashed line shows in Figure 12b.

In the EPR experimental spectrum where the first derivative is recorded, there are only two characteristic signals with the values of g-factor $g_{\perp} = h\nu/B_{\perp}\beta_e$ and $_{gz} = h\nu/B_z\beta_e$.

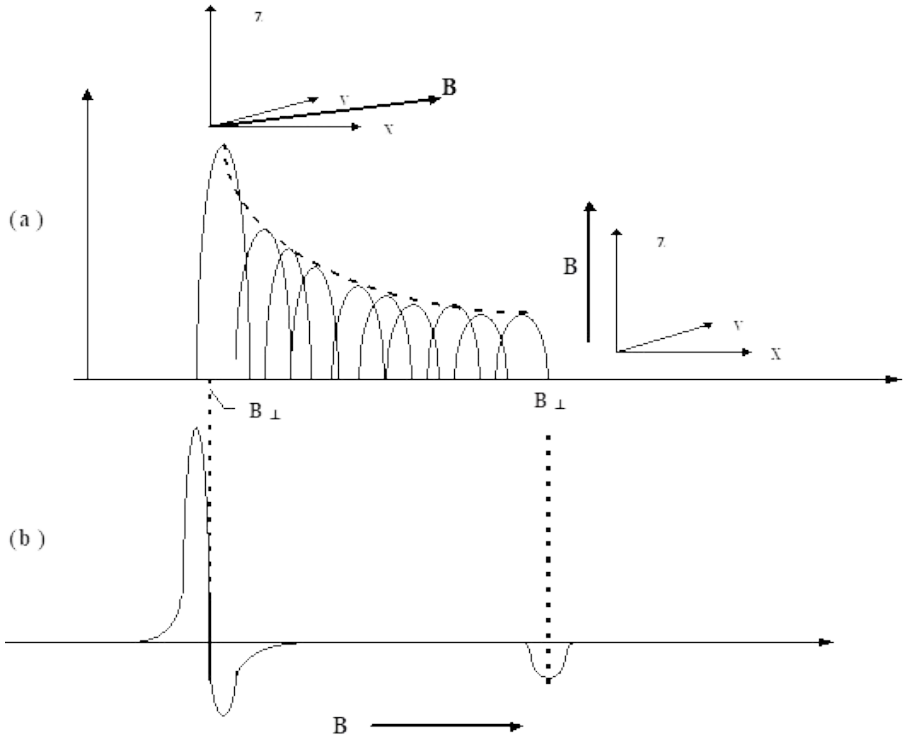

Figure 12: EPR spectrum of (a) absorption and (b) first derivative of a Zeeman axial symmetry anisotropy system for a resonance field, $B_{\perp} = B_X = B_Y$.

In the general case of axial symmetry, the value of g is given by the Equation 20a

$$g_{eff}^2 = (g_{\perp} \sin\theta)^2 + (g_z \cos\theta)^2 \quad (\textit{axial symmetry}) \qquad \text{Eq. 20a}$$

where θ is the angle of B with the axis of symmetry Z of the system.
In the case of the rhombic symmetry is given by the Equation 20b:

$$g_{eff}^2 = (g_X \cos\theta_{B,X})^2 + (g_Y \cos\theta_{B,Y})^2 + (g_Z \cos\theta_{B,Z})^2 \quad \textit{(rhombic symmetry)} \qquad \textit{Eq.20b}$$

As shown in Figure 13 in the EPR spectrum of the rhombic symmetry there are three characteristic signals with values of g factor as $g_x = h\nu/B_X\beta_e$, $g_y = h\nu/B_Y\beta_e$, $g_z = h\nu/B_Z\beta_e$.

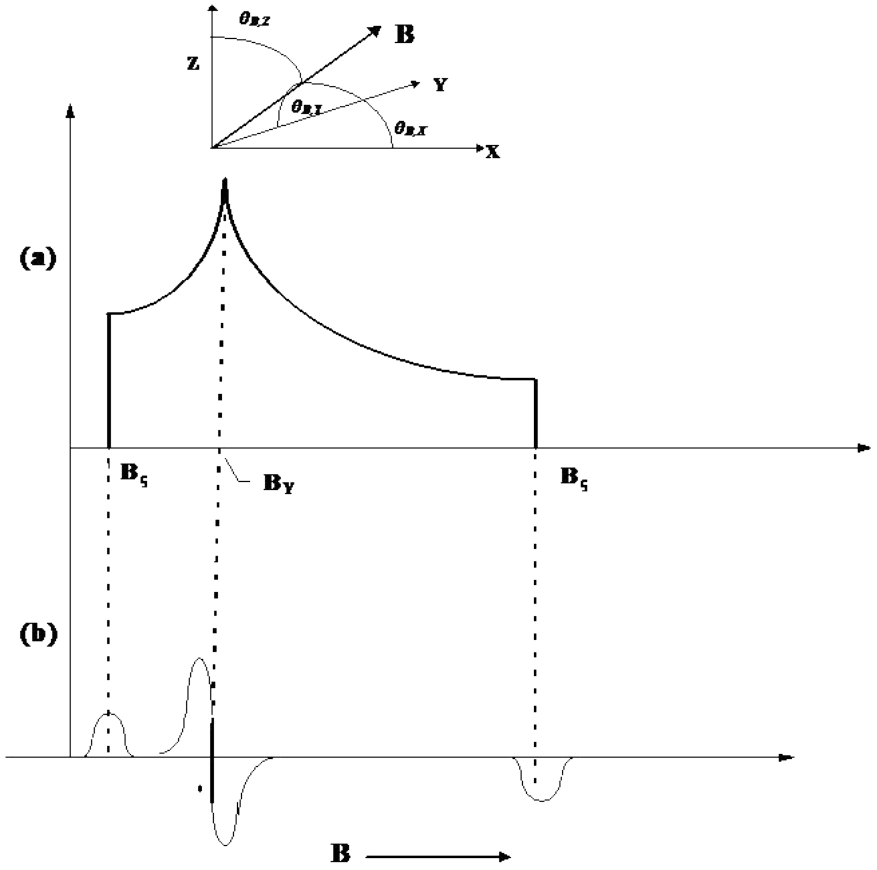

Figure 13: EPR spectrum (a) absorption and (b) first derivative of a system with Zeeman anisotropy of rhombic symmetry.

In the most general case instead of factor g, we are talking about tensor g which has main values g_x, g_y, g_z and can be written in table format as shown in Equation 21.

$$\mathbf{g} = \begin{bmatrix} g_X & 0 & 0 \\ 0 & g_Y & 0 \\ 0 & 0 & g_Z \end{bmatrix} \qquad \text{Eq.21}$$

The necessity and usefulness of this formalism is understood in the context of the Hamiltonian spin (Hamin spin) which we discuss below.

1.4 Spin Hamiltonian Formalism

Every spectral phenomenon requires an accurate understanding of the energy states of the system. The problem of calculating the energy states of a quantum mechanical system is detected:

(a) in the construction of the energy operator, , known as the Hamilton operator (Equation 22)
(b) solving the problem of the eigenvalues of

$$|\psi_i> = E_i |\psi_i> \quad \text{Eq.22}$$

where E_i is the eigenvalues and $|\psi_i>$ the eigenfunctions of *H*. The eigenvalues E_i are the permissible system energy values. In the case of atoms or molecules the eigenfunctions $|\psi_i>$ are the known atomic or molecular orbitals respectively.

The problem of the construction of the energy operator includes all the interactions that affect the system's energy such as Coulomb interactions between electrons, interactions of magnetic moments (S,L,I) with the existing magnetic fields (Zeeman interactions), interactions between magnetic moments (as hyperfine S-I, spin-orbit S-L) and more. The solution of a problem like that can be accomplished only my numerical methods which are extremely time consuming. On the other hand, with the approach of the Hamiltonian Spin is very efficient in making the problem simpler. The basic cases which the Hamiltonian spin uses are:

- The phenomena observed in the EPR spectroscopy come from the lower energy state of the system (ground state).
- This condition has no orbital degeneration i.e. we consider that **L**=0. The degeneration of this condition is due to the spin. This condition seems very restrictive since the majority of cases in the periodic table are L> 0. However, in most cases the interactions with solids cause the phenomenon of 'quenching' of the orbital momentum. Thanks to the damping of

the orbital torque, which is analyzed in the next paragraph, the lower state ends up being characterized by L = 0 and this allows the use of the Hamiltonian spin.

- This condition is described by an 'apparent' S_{eff} which is selected so that $2S_{eff}+1$ is equal to the number of system energy levels. So a system with two energy levels is described by $S_{eff} = ½$, but for six energy levels the spin that must be used is the Hamiltonian spin of $S_{eff}=5/2$.

In this context, the energy operator H is constructed to contain, in addition to parameters, only spin operators, hence the name 'Hamiltonian of spin'.

As for the quenching of angular moment we can assume with non-zero orbital torque. In its simplest form this is a system of p (l = 1) or d (l = 2) orbitals. In the absence of any interaction the three p-orbitals or five d-orbitals have the same energy. In addition, there are operations of symmetry that transform any orbital into another of the same group e.g. p_X in p_Y or in p_Z and similarly a d in another d orbital. Thus, in the absence of interactions, the three p-orbitals as well as the five d-orbitals, respectively, are fully equivalent or in quantum mechanical language are $2l + 1$ degenerate due to orbital torsion. In the case of interactions e.g. ionic, covalent, etc., the equivalence of these orbitals is abolished and the degeneration is removed. In the case of d-orbital of metal ions this removal of degeneration is due to the field of substituents (ligand field). In the case of p-orbital to organic molecule a typical cause of removal of orbital degeneration is the formation of bonds with adjacent p-orbitals.

In any case, the removal of orbital degeneration means that due to the interactions the levels are characterized by degeneration $2l+1 = 1$, i.e. they have $l = 0$ hence the term 'damping' of the orbital rotation.

The Simpler Hamiltonian Spin is:

$$H= \beta_e \, \mathbf{S} \cdot \mathbf{g} \cdot \mathbf{B} \qquad \text{Eq. 23}$$

where **S** is the operator of spin, **g** is the tensioner g and is given by the Equation 21 and **B** is the vector of the external magnetic field with B_X, B_Y, $B_Z=|B|$ ($cos\theta_{B,X}$, $cos\theta_{B,Y}$, $cos\theta_{B,Z}$). That operator is describing the Zeeman interaction between **S** and **B**, and in a more detailed way as:

$$H = \beta_e \begin{bmatrix} S_X & S_Y & S_Z \end{bmatrix} \cdot \begin{bmatrix} g_X & 0 & 0 \\ 0 & g_Y & 0 \\ 0 & 0 & g_Z \end{bmatrix} \cdot \begin{bmatrix} B_X \\ B_Y \\ B_Z \end{bmatrix} \Rightarrow H = \beta_e [S_X g_X B_X + S_Y g_Y B_Y + S_Z g_Z B_Z] \quad \text{Eq. 22}$$

In case of S=1/2, from Equation 22 the energies i.e. the eigenvalues of H are:

$$E_{\pm ½} = \pm ½ \beta_e [(g_X \cos\theta_{B,X})^2 + (g \cos\theta_{B,Y})^2 + (g_Z \cos\theta_{B,Z})^2]^{½} B \quad \text{Eq.23}$$

And so, from Equation 15 at the EPR experiment we have resonance at:

$$E_+ - E_- = h\nu = \beta_e g_{eff} B \quad \text{Eq.24}$$

where

$$g_{eff} = [(g_X \cos\theta_{B,X})^2 + (g \cos\theta_{B,Y})^2 + (g_Z \cos\theta_{B,Z})^2]^{½} \quad \text{Eq. 25}$$

and so the magentic field at resonance is described by the Equation 26

$$B = h\nu / \beta_e g_{eff} \quad \text{Eq. 26}$$

In that simple way we can be driven in fast results and by adding more interactions we can procceed to an accurate solution.

As in the case of hyperfine interaction if we use Spin Hammilotnian as shown in Equation 27 we have:

$$H = \beta_e \mathbf{S} \cdot \mathbf{g} \cdot \mathbf{B} + \beta_v \mathbf{I} \cdot g_n \cdot \mathbf{B} + \mathbf{I} \cdot \mathbf{A} \cdot \mathbf{S} \quad \text{Eq.27}$$

where exept the electronic Zeeman interaction as before we added the Nucleic Zeeman as mentioned earlier, by adding the term $\beta_v \mathbf{I} \cdot g_n \cdot \mathbf{B}$ and the term of interaction between electronic and nuclear spin, by adding $\mathbf{I} \cdot \mathbf{A} \cdot \mathbf{S}$. The ultra-fine interaction tensor A is characterized by one, two or

three main values depending on whether the ultra-fine interaction is isotropic, axial or rhombic respectively. In the general case of rhombic symmetry, **A** is written as:

$$\mathbf{A} = \begin{bmatrix} A_X & 0 & 0 \\ 0 & A_Y & 0 \\ 0 & 0 & A_Z \end{bmatrix} \quad \text{Eq.28}$$

1.5 Calculating g-tensor based on Perturbation Theory

The description of the g- tensor so far has been based on classical concepts which allow the description of the basic phenomena of magnetic resonance in a relatively simple way. In this section we will give a strictly quantum mechanical description of the tensor g which is based on the pertrubation theory. This formality allows accurate calculations and extraction of quantitative data from experimental EPR spectra.

In the presence of a magnetic field a system with spin S and orbital rotation L has the following Hamiltonian:

$$H = \beta_e \, g_e \cdot \mathbf{S} \cdot \mathbf{B} + \beta_e \, \mathbf{L} \cdot \mathbf{B} + \zeta \, \mathbf{L} \cdot \mathbf{S} \quad \text{Eq.29}$$

We note that is the most "reliable" Hamiltonian and not a spin Hamiltonian, since it explicitly contains the orbital **L**-rotation, the real Zeeman interaction $\beta_e \, g_e \cdot \mathbf{S} \cdot \mathbf{B}$, as well as the spin-orbit interaction $\zeta \, \mathbf{L} \cdot \mathbf{S}$. When the ground state is characterized by zero orbital torque, then the terms be L. B have no effect on the state of the system. In the language of EPR spectroscopy this means that the resonance simply corresponds to the value of the free electron. On the contrary, the introduction of the term $\zeta \, \mathbf{L} \cdot \mathbf{S}$ causes the mixing of the higher states to the basic. Applying first order disruptor theory the basic state $|\psi\rangle$ for spin ↑ or ↓ is differentiated and it is presented in Equations 30,31:

$$|+>=|\psi_o\uparrow> -\sum_n \frac{<\psi_n|\zeta LS|\psi_o>}{E_n - E_o}|\psi_n>$$

$$|+>=|\psi_o\uparrow> -\frac{1}{2}\zeta\sum_n \frac{<\psi_n|L_w|\psi_o>}{E_n - E_o}|\psi_n\uparrow> \\ -\frac{1}{2}\zeta\sum_n \frac{<\psi_n|L_x + iL_y\,|\,\psi_o>}{E_n - E_o}|\psi_n\downarrow>$$

Eq.30

and in the same way

$$|->=|\psi_o\downarrow> -\frac{1}{2}\zeta\sum_n \frac{<\psi_n|L_w|\psi_o>}{E_n - E_o}|\psi_n\downarrow> \\ -\frac{1}{2}\zeta\sum_n \frac{<\psi_n|L_x + iL_y\,|\,\psi_o>}{E_n - E_o}|\psi_n\uparrow>$$

Eq.31

On the basis of disturbed situations |+> and | > the Hammiltonian $H= \beta_e$ g_e **S B** + β_e **L**·**B** for B=B_z (**B**//z axis) has non zero table elements

$$<+| \quad \beta B<+|L_z + g_e S_z|+> \qquad \beta B <+|L_z + g_e S_z|->$$

$$<-| \quad \beta B <-|L_z + g_e S_z|+> \qquad \beta B <-|L_z + g_e S_z|->$$

which is excactly the same with the elements of the table of spin Hammiltonian so:

$$H= \beta_e \, \mathbf{S_{eff}} \, \mathbf{g_{eff}} \, \mathbf{B}$$

when we take the case of $\mathbf{S_{eff}}$=1/2

$$g_z = 2 <+|L_z + g_e S_z|+>$$

which can be written as:

$$g_z = g_e - 2\zeta \sum_n \frac{< \psi_o | Lz | \psi_n >< \psi_n | Lz | \psi_o >}{E_n - E_o}$$

Eq. 32

Similar relationships can be derived for the g_x and g_y components following a similar procedure. The Equation 32 is one of the cornerstones of EPR theory as it allows the accurate calculation of the apparent values g from the system's wavefunctions.

The equation 32 states that the cause of the deviation of the values g from the value of the free electron g_e is the mixing of the higher states due to the orbital rotation.

So as we understand till now the tensioners **A** and **g** are very important to the EPR expirement, those two tensioners are determined by the wavefunction of the unpaired electron. As we saw earlier at the Equations 21 and 28 both of those tensioners can be represented as a matrix at each case where all the values are zero except the diagonal values of those matrixes those values are called as main 'values'. The diagonal shape of the arrays only occurs when they are expressed in the axial system, known as 'principal axes system'. The usefulness of the principal axis system lies precisely in the fact that in this system A and g have the simple diagonal form and this greatly facilitates the analysis of the EPR spectra. In general, finding the orientation of the main axis system with respect to the molecular axes of symmetry is a rather complex problem. Only in systems with high symmetry e.g. flat aromatic rings, porphyrin complexes, there is an easy correlation of the two systemic axes.

The deviation of g from the value g_e= 2.0023 which characterizes the free electron, is determined by the contribution of the orbital rotation to the wavefunction. Since for the s electrons the orbital rotation is zero, values g≠2.0023 occur only for systems with p or d electrons.

CHAPTER 2

In this chapter the spin dynamics will be described and how they affect lineshape and linewidth also, we will analyze various relaxation times that characterize the interaction of electron spins with the surroundings (spin lattice interactions) and with each other (spin-spin interactions). In some cases, the lifetime of the individual spin-orientation state in a radical or the spin-orientation of the radical itself or that of a paramagnetic particle or even of a magnetic particle, may be so short that the linewidth is affected. So, from the change of the lineshape many kinetic information can be obtained. In other cases, the relaxation is dependent on the concentration of the paramagnetic species; in those cases, the information can be obtained by the changes in intensity. These effects can arise from electron exchange and transfer between molecular species, intramolecular motions, chemical reactions and so on. Without the understanding of the linewidth effects an EPR spectrum can be extremely difficult in understanding it. As the magnetic field approaches the region of an absorption line, the frequency shift of the resonator first is negative, then increases rapidly through zero at the center of an absorption line to a maximum and finally decreases asymptotically to zero. It will be described by starting from the simplest case of statical approach and its dependence by temperature. In that case where there are no spin dynamics Boltzmann distribution describes the system and the signal's intensity is affected by the difference of the populations. In the case of spin dynamics, we have the case of spin hopping because of spins interactions, where in that case the B_{res} is changing and the lineshape of peaks also. We will also describe the case of separated spins in a matrix versus temperature of Mn^{+2} ions in a matrix of $CaO/CaCO_3$. In that case the temperature will affect the lattice which will affect the spins and the relaxation time. Depending on how the relaxation time changes through the changes of temperature we can get information and much it with one of the already existing mechanisms like Curie, Raman or Orbach. At the last case we will explain how the temperature changes a ferromagnetic material which has spin domains. On this case when we measure materials like those, we see broad signals, but with the increase of temperature each spin domain reorientates before the melting point and like that the linewidth is getting smaller and the signal intensity is increasing. In Figure 14 we present the changes from an EPR spectrum where the y-axis is showing the increase of temperature and we see that we start from 77K where we have sharp (Lorentz type lineshape) and strong signal because of the maximum difference of spin populations and that at RT the signal is getting smaller and wider because of the Gauss type lineshape and again at 900K we get a sharp and strong signal.

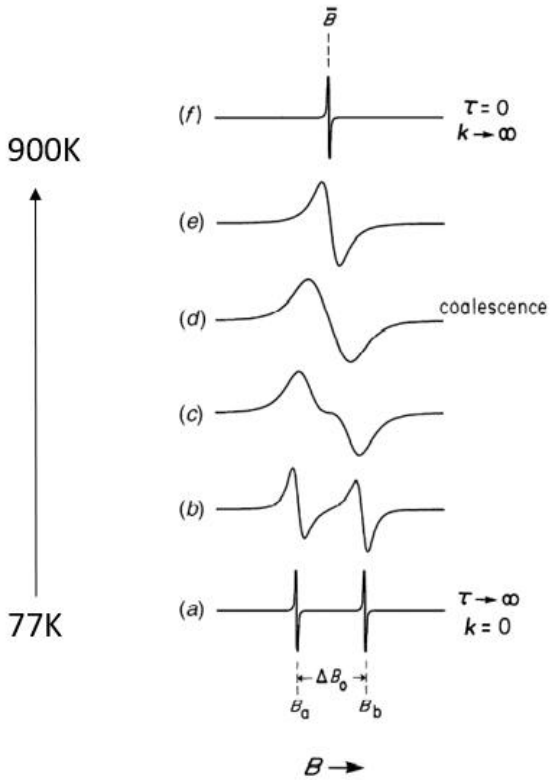

Figure 14: EPR spectrum on different temperatures and the change of lineshape and linewidth as we move from 77K up to 900K.

2.1 Statical Approach - Spin Temperature and Boltzmann Distribution

In this section the properties of a two-level spin system are examined. The system is defined as an ensemble of spins with S = 1/2 (electrons or protons), which are isolated (direct spin-spin interactions are negligible). A uniform external magnetic field is assumed, so the two energy levels are separated by $\Delta E = E_{upper} - E_{lower}$, where the ”upper” and ”lower” subscripts denote the upper and lower energy level, respectively. Only the corresponding Zeeman term in the spin Hamiltonian is considered, so that $\Delta E = g_e \mu_B B_0$. EPR samples consist of collections of many paramagnetic species, and not single isolated paramagnetic centers. If the population of radicals is in

thermodynamic equilibrium, its statistical distribution is described by the Maxwell–Boltzmann equation 33:

Eq.33

where N_{upper}, N_{lower} is the number of paramagnetic centers occupying the upper energy state and the lower state respectively, k_B is the Boltzmann constant, and T is the thermodynamic temperature. At 298K, the X-band microwave frequencies (v=9.75GHz) give $N_{upper}/N_{lower} \approx 0.998$, meaning that the upper energy level has a slightly smaller population than the lower one. Therefore, transitions from the lower to the higher level are more probable than the reverse, which is why there is a net absorption of energy.

Eq. 34

If the spin system is subjected to a pulse of electromagnetic radiation of energy matching the energy difference ΔE between the spin energy levels, the resulting EPR energy absorption by the spins cause a change in the populations – the ratio N_{upper}/N_{lower} is altered. The spin has gained energy, therefore it can be considered" hot" compared to its surroundings. The spin system then undergoes various interactions with its surroundings by which it cools down (loses energy) and its spin temperature T_S is eventually restored to the temperature T of the surroundings.

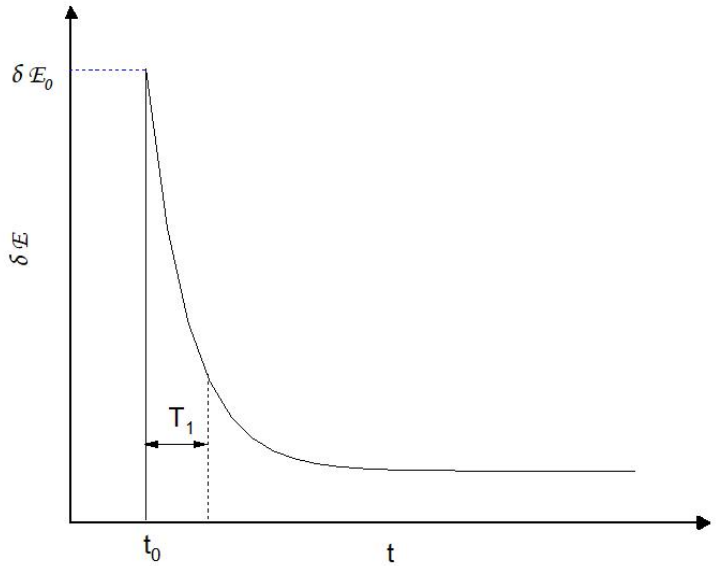

Figure 15: Plot of temporal decay of the extra energy δE_0 in the system. Here t_0 denotes the time of energy influx into the system and T_1 stands for a measure of connection of the spin system to its surroundings.

The loss of energy, considering the system receives an extra energy δE_0 by irradiating at time $t = t_0$, is depicted in Fig. 15 and is also described by exponential decay

Eq.35

Where T_1 is the characteristic time for the energy flow from the spin system into the surroundings. This relaxation time T_1 reflects the degree of connection of the spin system to its surroundings.

The final state ($t \rightarrow \infty$) then is one for which Ts =T, and we note from Equation 34 that the spins only then attain the Maxwell–Boltzmann distribution valid at temperature T.

2.2 Difference of spin population

If we examine the population difference:

$$\Delta N = N_{lower} - N_{upper} \qquad \text{Eq.36}$$

as a single variable ΔN (B, T_S). Then

$$N_{upper} = 1/2\ (N - \Delta N) \qquad \text{Eq.36a}$$

$$N_{lower} = 1/2\ (N + \Delta N) \qquad \text{Eq.36b}$$

where $N = N_{upper} + N_{lower}$ is to total population of spin species.

Let the probabilities per spin in unit time for upward and downward transitions be $Z_{\uparrow}$ and $Z_{\downarrow}$. It is assumed that the spins are isolated from each other, the differential rate law for this kinetic system is shown in Equation 37.

The first term on the right is the rate of upward transitions and the second the rate of downward transitions. The factor 2 appears because an upward or downward transition changes ΔN by 2 as shown in Figure 16.

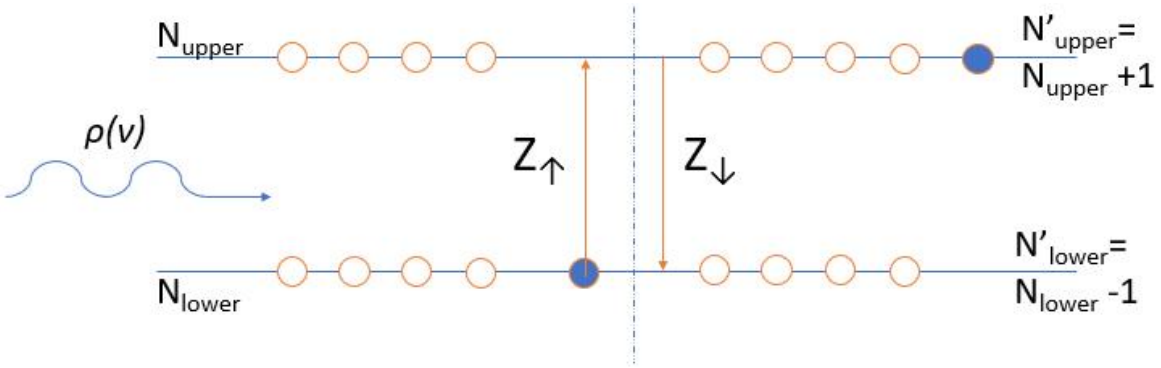

Figure 16: Two level spin system: N_{upper} and N_{lower} are the occupancy numbers in the upper and lower levels, $Z_{\uparrow}$ and $Z_{\downarrow}$ are the transition probabilities per unit time for upward and downward transitions, ΔU is the energy separation of the two levels, and ρ_v is the radiation density, at frequency $v = \Delta U/h$, to which the system is exposed. In Equation 36 the factor 2 for examples for an upward transition appears because $\Delta N' = N'_{lower} - N'_{upper} = N_{lower} - 1 - (N_{upper} + 1) = \Delta N - 2$ with a probability of $Z_{\uparrow}$.

The Equation 37 can be rewritten as:

Eq.38

The spin system approaches a steady state, that is, $d\Delta N/dt = 0$. Thus, from Equation 36a we obtain that for a steady state ('ss'):

Eq.39

and from Equation 38 for a steady state spin system, we obtain:

Eq.40

The quantity of has dimensions of time and is by definition the relaxation time $\boldsymbol{\tau_1}$. The equation XXXX5 then becomes as:

Eq.41

More often one can use the approximation (i.e. from Equation 39 $\Delta N^{SS}/N$ is small), so that $\tau_1 \approx (2Z)^{-1}$. In that case we note that τ_1 is a statical parameter, not to be associated with individual spins. The Equation 40 is a first-order kinetic equation with the solutions as shown:

Eq.42

$\Delta N(t)$ evolves exponentially from $(\Delta N)_0$ toward ΔN^{ss} with a rate constant $k_1=\tau_1^{-1}$, where τ_1 is now seen to be the time that is required for ΔN to change by $[\Delta N^{SS}-(\Delta N)_0][1-e^{-1}]$. From the definition of

τ_1 as the inverse of the sum of the transition probabilities per unit time (Equation 41), it is clear that τ_1 is related to the mean lifetime of a given spin-orientation state. This lifetime limitation has an effect on linewidth. All quantum-mechanical transitions have a limiting **non-zero** spectral width, called lifetime broadening, which arises from the finite lifetime of any excited state. That width is numerical and spreads to Heisenberg uncertainly principle where in general $\delta\tau \bullet \delta E \geq \hbar/2$, where δE is the uncertainty in the energy of the system due to the non-zero probability Z per second of its decay and $\tau=Z^{-1}$ is its mean lifetime. The quantity $|\delta E| \approx \hbar/(2\tau)$ is called the width of the energy level considered. For example, if $\tau_1=10^{-9}s=1$ ns, then $|\delta E| \approx 10^{-25}$ J or $\Delta\nu \approx 10^{8} sec^{-1}$, corresponding to EPR linewidth of about 6.0 mT=60 Gauss. Lifetime broadening is one of the contributions to the homogeneous linewidth and defines the minimum linewidth for a given system.

2.3 Relaxation time and Mechanism of τ_1

The nature of the transition probabilities $Z_\uparrow$ and $Z_\downarrow$ can be explained by several mechanisms which can contribute to these terms, as expressed by the Equations XXX.

Eq. 43a

Eq. 43b

where ρ_ν is the time-averaged radiation density[42] to which the spin system is exposed, $W_\uparrow$ and $W_\downarrow$ are the upward and downward probabilities per unit time for transitions induced by the surroundings (i.e., the lattice), A_{ul} is the Einstein coefficient for spontaneous photon emission, and B_{ul} and B_{lu} are the Einstein coefficients for stimulated emission and absorption, here applied to magnetic dipole transitions (note that $B_{ul}=B_{lu}$).
So by substituting Equation 43a and Equation 43b into Equation 40 and Equation 41, we obtain the following equations:

Eq. 44

and

Eq. 45

We note that τ_1^{-1} can be regarded as the sum $\Sigma_i(\tau_{1i})^{-1}$ over distinct relaxation mechanisms. We consider the following cases:

A) The spin system is removed from its surroundings, including impinging radiation [44]. Then the B and W terms in Equations 44 and 45 are zero. Thus, ΔN decays with a rate constant $t_1 = A_{ul}^{-1}$. In this case $\tau 1$ is very long (10^4 years for EPR when field B=1 T, for a set of uncorrelated spins), but eventually ($t \rightarrow \infty$) the system decays to $\Delta N^{ss} = N$, that is, with no spins in the upper level. In other words, the temperature of the surroundings is effectively 0 K.

B) The isolated spin system is exposed to radiation from a source at temperature T. Now the B terms in Equations 44 and 45 are non-zero. When the source is a blackbody, then ρ_v is given by the Planck blackbody law. Now the spin system comes to equilibrium with the radiation source at temperature T, even though there are no other surroundings. Thus, the final ratio N_u/N_l of the spin populations is given by Equation 34 with T_s=T. However, at 3 K [44] τ_1 is still very long (now about 10^3 years). When the source furnishes an excitation field B1 oscillating at a well-defined frequency, the spins attain a value of Ts, which can be said to define the effective temperature of that source.

C) The normal surroundings (electrons and nuclei) are now restored, so that the probability terms W are present and dominate in Equations 44 and 45. The relaxation of the spin system, with the spin-lattice relaxation time τ_1 [45], occurs primarily through electron-spin flips induced by dynamic interactions with the surrounding matter (‘lattice’). This can be anything from the molecule itself to the surrounding solvent or lattice (if in a crystalline solid—hence the origin of the name). The lattice generally can be assumed to have infinite

heat capacity, so that its temperature can be taken as constant throughout the EPR experiment. Approach of τ_1 to zero now implies approach to thermal equilibrium between the spins and the lattice, that is, 'instant' energy transport from ρ_ν to the latter.

If the radiation density (ρ_ν) term dominates in $Z_\uparrow$ and $Z_\downarrow$, then these become equal and $\Delta N \rightarrow \Delta N^{ss} \rightarrow 0$ (Equations 42 and 44). Hence there will be no net absorption of radiation by the spins; that is, the EPR signal disappears. This important tendency is called 'power saturation', and points to the importance of having an adequate spin-lattice relaxation mechanism and of applying only a moderate B_1 field.

Experimentally, τ_1 values are typically about 1ms so that the W terms must be of the order of 10^6 s^{-1} . Since $A_{ul} \approx 3\ 10^{-12} s^{-1}$, A_{ul} can be neglected compared to the W terms. The $2B_{ul}\rho_\nu$ term can be made as large or small as desired according to the intensity of the exciting radiation. When this term increases and becomes greater than the W terms, the system is said to approach saturation. For the moment we assume that the system is not saturated (so that $Z_\uparrow = W_\uparrow$ and $Z_\downarrow = W_\downarrow$).

Typically, the transitions between the spin levels are stimulated by fluctuations in local magnetic fields arising from motions of the spin-bearing molecules or of the surrounding structure. These fluctuations have a spectrum of frequencies that range over many orders of magnitude with varying intensities (a spectral density). However, only those fluctuations with a frequency that matches the EPR frequency are capable of inducing transitions.

2.4 Spin Relaxation: Bloch Model

In a solid to describe spin relaxation we will use Bloch equations [46] that describe the time dependence of the total spin magnetization vector **M** in the presence of static and oscillating magnetic fields externally applied. The usage of the Bloch equations is happening because they:

- Furnish a visual and intuitive model, in terms of vectors and torques, of the magnetic-resonance phenomenon. This is especially helpful when an understanding of the effects of microwave pulses in EPR is required. An introduction to the rotating frame also ensues.
- simplify the very complex subject of the spin interaction with the atomic surroundings by gathering together these aspects into just two empirical parameters, the relaxation times τ_1 and τ_2.
- introduce the important concepts of absorption and dispersion.
- Lead gracefully into the topic of interconversion between two ensembles of different spin-state populations, for example, chemical exchange.

The Bloch equations apply to any pair of energy levels, more or less adequately, of course, they have limitations in their usefulness, they are a set of macroscopic equations that are used to calculate the nuclear magnetization $\mathbf{M} = (M_x, M_y, M_z)$ as a function of time when relaxation times τ_1 and τ_2 are present. These are phenomenological equations that were introduced by Felix Bloch in 1946 [46].

2.5 Magnetization in a Static Magnetic Field

In the absence of an external magnetic field, the bulk magnetization M, if present, is fixed in space, with components Mx, My and Mz in an arbitrary cartesian coordinate system. When the ensemble of magnetic moments is exposed to a static and homogeneous magnetic field **B**, in the absence of relaxation, it is in a dynamic equilibrium [47]. However, here M is not fixed in space, moving according to the equation of motion so:

Eq.46

where γ_e is the electronic magnetogyric ratio, equal to $g\beta_e/\hbar$. Let's assume that **B** is along with **z-**axis the Equations XXXXX-XXXXX can be obtained as shown below.

Eq.47a

Eq.47b

Eq.47c

with solutions:

Eq. 48a

Eq. 48b

Eq. 48c

to these equations reveal that **M** processes about **B** with an angular frequency $\omega_B=-\gamma_e B$ (the classical Larmor frequency) if is non-zero. The longitudinal magnetization M_z is constant. Here the field was taken to be static; the effects of modulating it sinusoidally lead to more complex solutions.

As mentioned earlier the Bloch equations include relaxation effects. If the system is subjected to a sudden change in the magnitude and/or direction of B, then M_x, M_y and M_z (referenced to the new field direction) in general relax to their new equilibrium values at different rates. For instance, if the magnetic field is suddenly turned on (B=0 at $t=t_0$), then ΔN initially is 0 and it as well as the component M_z follow an exponential rise with time.

By also assuming (as is usual) that the transverse components M_x and M_y relax with the same rate constant, which is the inverse of a new characteristic time τ_2 called the transverse relaxation time. Thus:

Eq. 49a

Eq. 49b

Eq. 49c

The solutions of these empirical equations feature the decay of the components M_x and M_y to zero. Note that both τ_1 and τ_2 in the Bloch formulation are empirical bulk (ensemble) properties. Note that in the absence of relaxation effects i.e., τ_1 and τ_2 equal to ∞ and hence we retrieve the Equations 47a-47c.

2.6 Magnetization in an Oscillating Magnetic Field

In the case of an oscillating magnetic field $\mathbf{B_1}$ with the components as shown below:

$$B_{1x}=B_1\cos(\omega t) \quad \text{Eq.50a}$$

$$B_{1y}=B_1\sin(\omega t) \quad \text{Eq.50b}$$

$$B_{1z}=0 \quad \text{Eq.50c}$$

we take ω to be positive and with the use of the above B_1 components we take the complete equations of motion (the Bloch equations) which are [46]:

Eq.51a

Eq.51b

Eq.51c

Because **M** is continuously precessing about **B**, it is easier to visualize the time dependence of **M** if we transform to a coordinate frame that is rotating about z (azimuthal angle φ) at the angular frequency ω with the same sense as that of $\mathbf{B_1}$ taking the new x axis xφ to be along $\mathbf{B_1}$. The components of M in this new coordinate frame are called $M_{x\varphi}$, $M_{y\varphi}$ and M_z. The Bloch equations in the rotating frame then are:

Eq.52a

Eq.52b

Eq.52c

where $\omega_{B=} -\gamma_e B$. The energy of the spin moment in a magnetic field depends on the rotational frame selected; that is, the fields seen by the particle differ. It turns out that the spin temperature T_s and also the spin-lattice relaxation time τ_1 are somewhat dependent on the rotational speed.
The transverse magnetization can be defined in Equation 53 as:

Eq.53

if the equation 54 is combined to yield then:

Eq.54

where,

Eq.55

Equations 52 (a-c) are a set of coupled linear differential equations with constant coefficients and can be solved in a straightforward manner. The steady-state solutions are

Eq.56a

Eq.56b

Eq.56c

Note that the response $M_{x\varphi}$ is in phase with B_1, whereas $M_{y\varphi}$ is 90º out of phase. The magnitudes of $M_{x\varphi}$ and $M_{y\varphi}$ tend to be small compared to that of M_z^0. For sufficiently small values of B_1, the last term in each denominator may be neglected. This power-saturation term predicts that **M** vanishes as B1 (i.e., ρ_v) increases indefinitely [48]. The solutions in Equations 56 apply only for a field $\mathbf{B_1}$ rotating in the same sense as **M**. The usual experimental setup has $\mathbf{B_1}$ oscillating linearly in the (say) x direction, with B_{1x} only non-zero term as ($B_{1x}=2B_1\cos(\omega t)$) and ω taken positive, that term of course can be decomposed in two equal-magnitude and oppositely rotating fields as shown in the Equation 57 below:

$$\mathbf{B_1}= \mathbf{B_1}(+)+ \mathbf{B_1}(-)=B_1(\cos(\omega t)\mathbf{i}+\sin(\omega t)\mathbf{j})+B_1(\cos(\omega t)\mathbf{i}-\sin(\omega t)\mathbf{j}) \quad \text{Eq.57}$$

where $\mathbf{B_1(+)}$ rotates in the same direction as the Larmor precession, so that $\omega_B-\omega$ is small and the resonance effects predicted by Equations 56. However, $\mathbf{B_1(-)}$ rotates in the opposite direction, and its effects being small are neglected herein. The effects of the imposition of the oscillating field $\mathbf{B_1}$ are often described in terms of dynamic (volume) susceptibilities x' and x'' (often called the 'Bloch susceptibilities').

$$\chi'=+\kappa\mu_0 M_{x\varphi}/B_1 \quad \text{Eq.58}$$

$$\chi''=-\kappa\mu_0 M_{y\varphi}/B_1 \qquad \text{Eq.59}$$

where κ is the relative permeability of the medium and B_1 the amplitude of the linearly polarized magnetic field. Thus, by combing the Equation 59 and Equations 56 the below Equations are:

Eq.60

Eq.61

where χ^0 is the static magnetic susceptibility $\kappa\mu_0 N_v g^2\beta_e^2/4k_BT$ and T the lattice temperature. Note that $\chi''=\chi'/[(\omega_B-\omega)\tau_2]$ and that both depend on B as well as on B_1 via the power-saturation term [49].

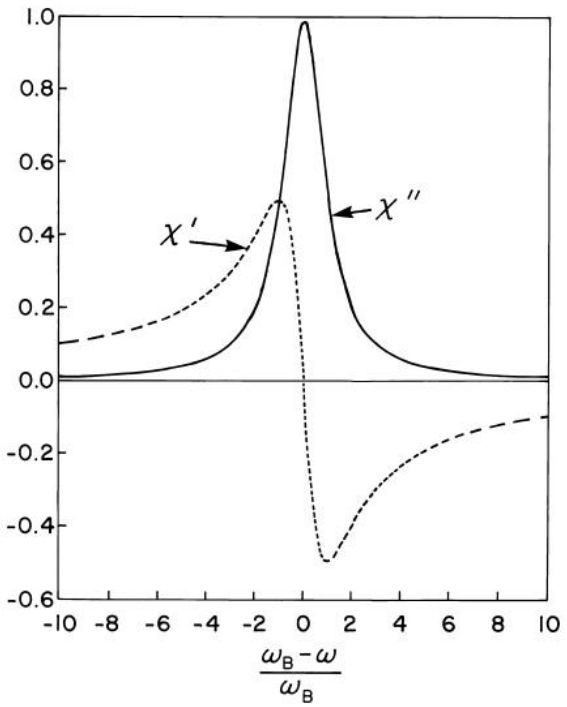

Figure 17: The in-phase (χ') and out-phase (χ'') components of the dynamic magnetic susceptibility versus the angular frequency deviation.

The EPR absorption signal is proportional to the component of the magnetization measured perpendicular to B_1, which is M_y, obtained by solving Equation 52 (a-c). If the perturbation attributable to the microwave field is a continuous one and it is small, the Bloch equations are solved in the stationary regime by placing the time derivatives of the magnetization components equal to zero. In this CW regime the solution for M_y is:

Eq.62

From Equation 61 which is a function of ω called Lorentzian function, which represents the shape of the EPR resonance line. The width of the line is inversely proportional to relaxation time τ_2 (Equation 62).

2.7 LINEWIDTHS

Every spin is a Lorentzian function, but the total spectra of $Y(\omega-\omega_B)$ is a normalized Lorentzian function and the power P_α absorbed by the linearly polarized excitation field per unit sample volume [50] is:

Eq.63

Hence by combining the Equation X555 and Equation 60 and 61 the final equation is as below:

Eq.64

Depends on the experimental conditions i.e. on the applied magnetic field B_1 via the linewidth as shown in Equation 64.

Eq.65

The increase in linewidth as saturation sets in can be discussed in terms of 'lifetime broadening'. Increasing the microwave power produces spin transitions at a faster rate and hence decreases the mean spin-orientation lifetime. As B_1 becomes very large, τ_1 becomes proportional to B_1^{-2} and hence Γ becomes insensitive to B_1 (when τ_2 is non-zero).

As long as the term $\ll 1$, the saturation term can be neglected, and both P and dP/dB are proportional to B_1^2. When the absorption line is strongly saturated i.e. $\gg 1$, according to the Bloch theory, both χ' and χ'' decrease with increasing power P_0 and P_a becomes constant. However, the theory fails for $B_1 > B$ and $\tau_1 \neq \tau_2$ as in solids. All the equations here are written in terms of ω and ω_B, though in EPR, ω is held constant and B is scanned. It is easy to switch to B as the variable [50] with $\omega = \omega_B$ (resonance state) held fixed; now ω_B is the angular frequency at a particular value B as given by the resonance condition. So by switching to field sweep conditions, the lineshape function, now $Y(B-B_{res})$, is a Lorentzian with half width at half-height given by:

Eq.66

Linewidths can be classified as *homogeneously broadened* and *in-homogeneously broadened*.

2.7.1 Homogeneous Broadening of Linewidth

At homogeneous line broadening for a set of spins occurs when all these see the same net magnetic field and have the same spin-Hamiltonian parameters. (More correctly, the local fields need not be identical at any one instant but need only give the same time averaged field over sufficiently short intervals.) This means that the lineshape (i.e., the transition probability as a function of magnetic field) is the same for each dipole. The resulting line usually has a Lorentzian shape This is in accord with the predicted Bloch absorption lineshape as we mentioned earlier, which is Lorentzian with a linewidth (half-width at half-height) in frequency ω units of τ_2^{-1} under non-saturating conditions. In general, an effective τ_2 can be defined by equating it to $|\kappa\gamma_e\Gamma|^{-1}$ where

Γ (mT or G) now is the half the linewidth at half-height in the absence of microwave power saturation and κ is a factor that depends on the lineshape (for example for Lorentzian lines $\kappa=1$ and for Gaussian lines $\kappa=(\pi \ln 2)^{1/2}$).

Spin-Spin Interaction

To visualize one possible contribution to $\tau 2$, one can return to consideration of the individual spins. It has been established that $\tau 2$ often is a measure of the interaction between spins. In this case, on one hand if $\tau_2=\infty$ it means that the spins are completely isolated from each other, on the other hand whereas $\tau_2=0$ implies very strong coupling, such that there are no local variations in the spin temperature.

The spins can interact via magnetic dipolar coupling. Note that mutual spin flips of paired spins cause no change in energy of the spin system but do affect the lifetime (τ_1) of each spin. The propagation of magnetization through the lattice via such flips, called *spin diffusion*, causes equilibration to the same spin temperature throughout the system of equivalent spins; τ_2 is a measure of this rate.

Another model invoking random sudden fast events considers collisions (e.g., in gas-phase radicals) that reorient the spin magnetic moments. This leads to Bloch type equations where now $\tau_1=\tau_2$ is the mean time period between collisions.

As we mentioned earlier in Equation 64 the linewidth is determined by adding term in the equation so the new one will be:

Eq.67

The lifetime broadening produced by the first term is missing in the Bloch formulation (which predicts a Dirac d-function absorption in the limit $\tau_2 \rightarrow \infty$).

In the absence of nuclear and/or paramagnetic electron motions, it is expected that the width of the EPR lines should not change drastically as a function of temperature below room temperature.

However the expansion of the material's lattice should be taken into account, since T_2 , where $r_{e\text{-}X}$ is the average distance between a paramagnetic electron and its nearest-neighbor paramagnetic electron, it follows that:

Eq.68

where α a is the linear expansion coefficient.

2.7.2 In-Homogeneous Broadening of Linewidth

At in-homogeneous broadening the line-broadening mechanism distributes the resonance frequencies over an unresolved band, without broadening the lines arising from individual equivalent spins. Generally, the unpaired electrons in a sample are not all subjected to exactly the same B values. Thus, at any given time, only a small fraction of the spins is in resonance as the external magnetic field is swept through the 'line'. The observed line is then a superposition of a large number of individual components (referred to as 'spin packets'), each slightly shifted from the others. The resultant envelope often has approximately a Gaussian shape as shown in Figure 18 above [51]. It thus is possible to choose B_1 so as to power saturate some selected portion of the EPR line, decreasing its intensity there (this is known as 'hole burning').

Some causes of in-homogeneous broadening for a given spin (chemical) species:

1. An inhomogeneous external magnetic field.
2. Anisotropic interactions in randomly oriented systems in the solid state. Here the distribution of local magnetic fields resulting from the anisotropic g and hyperfine interactions gives rise to the inhomogeneity.
3. Dipolar interactions with other fixed paramagnetic centers. These may impose a random local field at a given unpaired electron, arising from dipolar fields from other electron spins.

Any dynamic process in and around the paramagnetic center can cause lineshape effects. Some such processes are hindered rotation, tumbling of the molecule in a viscous liquid, interactions with other paramagnetic species and chemical reactions (e.g., acid-base equilibria and electron-transfer reactions). This broadening arises from dynamic fluctuations in the local field at the unpaired electron(s). If the changes occur sufficiently slowly, one observes lines assignable to distinct species (e.g., conformers). However, as the rate of fluctuations increases, the EPR lines broaden and finally coalesce into a single line (or set of lines), the position of which is the weighted average of the original line positions.

Consider that a radical can exist in either of two distinct forms or environments, a and b (i.e., each has a distinctive EPR spectrum). For the sake of simplicity, assume that the probabilities for these forms are f_a and f_b (where fa+fb = 1) and that each form gives rise to a single EPR line of Lorentzian shape, one at resonance field B_a and the other at a higher field B_b as shown in Figure 18. The line separation is $\Delta B_0 = B_b - B_a$ and often depends on **B**. In other words, the two species generally have different g factors. When we use the word slow or fast, we mean interconversion rates (e.g., local magnetic-field fluctuations) that are slow or fast compared to the characteristic parameter $|\gamma_e \Delta B_0|$. The actual time taken for a molecule to react to such an event is assumed to be very short compared to the inverse of this.
Relaxation times τ_{2a} and τ_{2b} represent the inverse linewidths for forms a and b in the absence of dynamic processes (and of power saturation). These are taken to be independent of temperature. We note that $\gamma_a \neq \gamma_b$ implies ga ≠ gb.

Eq.69

and the total complex transverse magnetization G is then given by:

Eq.70

where $\alpha_{\alpha,b}$ are complex numbers. Consistent with the chemical balance condition $f_\alpha k_\alpha = f_b k_b$, the population fractions obey the relations $f_\alpha = \tau_\alpha/(\tau_\alpha+\tau_b)$ and $f_b = \tau_b/(\tau_\alpha+\tau_b)$. By using $\tau_\alpha^{-1} = k_\alpha$ as well as $\tau_b^{-1} = k_b$ and by defining an inverse lifetime $\tau^{-1} = \tau_\alpha^{-1} + \tau_b^{-1}$.

The functions G_α and G_b can be considered in the same sense as concentrations in chemical kinetics.

Thus, for the reaction : .

The Equation 69 can be rewritten now as shown below (Equation 70):

Eq.71

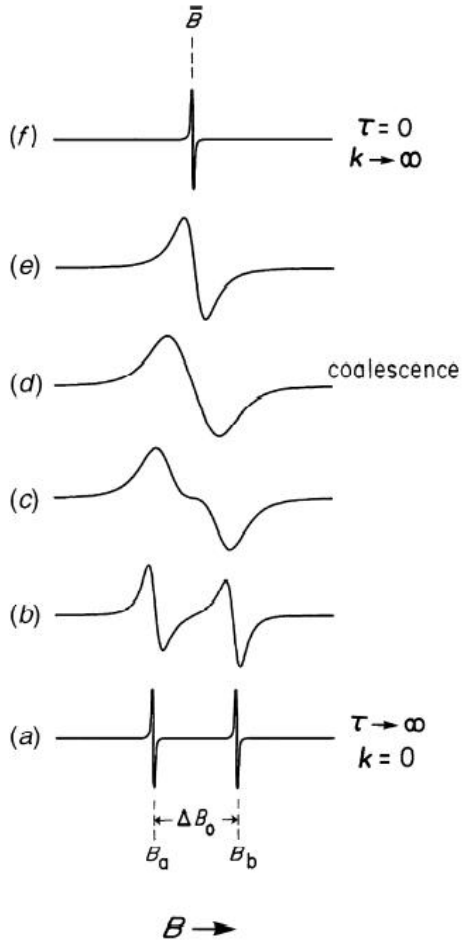

Figure 18: Synthetic first-derivative spectra showing the effect of increasing rate of interconversion between species a and b of an unpaired-electron species: (a) slow-rate limit (τ→∞); (b) moderately slow rate τ>>|ΔB₀| ; (c) faster rate showing spectral lineshifts; (d) coalescence point; (e) fast-rate limit (τ→0) , where it was assumed that $\Gamma_{0a}=\Gamma_{0b}(=\Gamma_0)$ and that $f_\alpha=f_b$.

Now we will explain each of the cases shown in Figure 18 that shows the effect of increasing rate of interconversion between species a and b of an unpaired-electron species.

- We start with Slow Dynamics, as shown in Figure 18a, where lifetimes τ_a and τ_b are long compared to $|\gamma_e \Delta B_0|^{-1}$ and because of that we expect two separate lines. For instance, when B is near $B_\alpha = -\omega/\gamma_\alpha$, and $G_b=0$ that line shape is Lorentzian with an absorption half-width at half-height of:

$$\Gamma_\alpha = \Gamma_{0\alpha} + |\gamma_\alpha \tau_\alpha|^{-1} \quad \text{Eq.72}$$

where τ_α is the average lifetime of the form α. There is an exactly analogous lineshape expression for b form. At Figure 18b we see that each line is broadened (but not shifted) by the onset of the dynamic process. By measuring the increase in linewidth, one can determine the rate constants for the dynamic process.

- Also, for the Intermediate Dynamics, as the system progresses from the slow-rate region into the intermediate region, the two lines are seen not only to broaden but also to shift inward as shown in Figure 18c. one can derive that the separation of the two lines is given [21] by

Eq.73

valid when the first right-hand term dominates. Eventually, the two lines coalesce into a single broad line centered at as shown in Figure 18d. The coalescence point (defined as the point at which the second derivative of the absorption changes sign at B=) is found to occur at a τ value, as shown below as:

Eq.74

Note that this value (which is in s rad^{-1}, since γB is an angular frequency) generally depends on the measurement frequency used, since ΔB_0 does. The coalescence phenomenon is a manifestation of the lifetime-broadening relation. If one writes this as $\Delta t \Delta\omega \approx 1$, where Δω is the separation of the two lines in angular frequency units, then Δt

represents the smallest average time period during which the states a and b may be distinguished. If the lifetime τ is less than Δt, then only one central line is observed, since the two states cannot be distinguished.

- Now, when the two forms are interchanging very rapidly, such that τ_α and τ_b are very short the τ terms can be neglected and the line shape is Lorentzian with an absorption half-width at half-height is given as:

Eq.75

where the weight average is:

Eq.76

Eq.77

and represents a Lorentzian line of width (half-width at half-height) which is centered at A more detailed analysis shows that, as the system approaches the fast limit, the lineshape is centered at B with a Lorentzian lineshape, as shown in Figure 17e but that the linewidth is given by:

Eq.78

Thus, again kinetic rate constants can be obtained from the changes in the linewidth of the single line.

We see, then, that EPR spectroscopy can yield rate data even for a chemical system in a steady-state condition. Thus, via lineshape simulations (usually produced by computer) of spectra taken

over an appropriate range of temperatures T and using the exact formula for im[G(τ)], one can assemble an Arrhenius plot of $\ln(\tau^{-1})$ versus T^{-1}, the slope of which yields the activation energy for the chemical process at hand. Linewidths $\Gamma_{0\alpha}$ and Γ_{0b} must be known and must not be too temperature-sensitive; the same is true for the equilibrium constant $K=f_a/f_b$, obtainable from the relative areas of the absorption curves available until they merge.

When there is observable zero-field splitting (e.g., hyperfine effects at either site), the Bloch formalism for the EPR lineshape of chemically or physically dynamic species is not adequate.

2.7.3 Why we need High Temperature EPR?

The temperature is a factor that influences the magnetic characteristics of a material. With the increase of the temperature, the vibrations in the lattice are also increased and so the magnetic torques of the atoms are free to rotate faster till the point where they disorganize and so the material loses its magnetism. The temperature that the ferromagnetic materials lose their magnetism is called Curie Temperature (Tc) and above T_c they behave as paramagnetic. All the magnetic phenomena that can happen at a material can be changed if we change the size, at the nanoscale, new magnetic phenomena are popping up like the superparamagnetism [52]. More specifically superparamagnetism is the result of the influence of the size to the magnetic properties of the materials and it exists when the size is getting tiny. Superparamagnetism is a property that is appearing at a single domain of magnetic particles. In general, when a magnetic field is applied to the magnetic material, the Weiss walls are moved and so the materials magnetism is changing, at the nanoscale though the Weiss wall construction isn't favored energetically and so the material is characterized as single domain. The thermal energy (k_BT) increases the thermal interactions and under a critical size $d_{critical}$ that energy is greater than the energy of magnetic anisotropy (as shown in Figure 19), which is the ability of a material to be magnetized under an applied magnetic field and its depended of the direction that its measured. At nanomaterials the magnetic anisotropy is happening for two reasons: firstly, at the coupling of the magnetic torques of the electrons with the

potential of the crystalline lattice and secondly the nanomaterials don't have a sphere shape and the orientation of the magnetism is favored to the direction of the bigger axis.

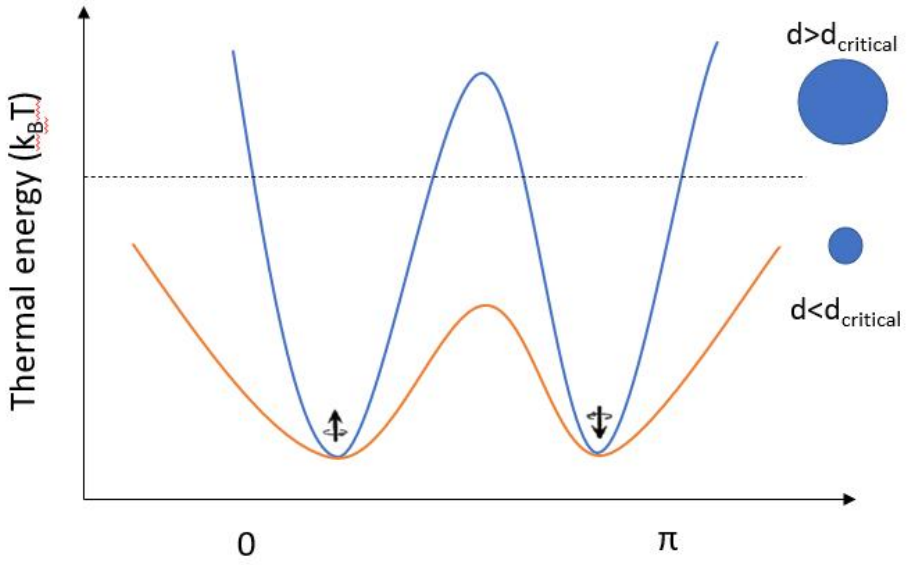

Figure 19: Magnetic anisotropy versus thermal energy with the decrease of the nanomaterial's size.

The time between the change between two magnetic torques changes is called relaxation time and is known as Neel relaxation and is calculated by the Equation 79, as shown below:

Eq.79

where τ_0 is the characteristic time of the material as for example for maghemite (γ-Fe_2O_3 that time is 10^{-9} sec= 1ns). The temperature where the material is transferring from the ferromagnetic to the superparamagnetic status is called blocking temperature.

Another factor who influences the magnetic properties at the nanoscale is the surface anisotropy [REF], which is based on the number of unit cells of the surface of the nanomaterial versus their number inside. As the size of the nanoparticle is decreased the percentage of the surface lattices is increased and vice versa.

For many studies it is necessary to vary the temperature of the sample. Temperature control may be needed to hold a sample in a well-defined state of equilibrium or to study at a series of

temperatures. Cryogenic temperatures may be needed for transition metal ions with short relaxation times such that lines are too broad to detect at 298 K.

For substances that obey the Curie law, susceptibility is proportional to 1/T with T in K. This includes most S=1/2 species except those with thermally accessible excited states. The relative population of two energy levels, such as the two energy levels of an electron spin in a magnetic field, is given by the Boltzmann distribution function as presented earlier.

As is shown in standard texts, the ratio of spins in the high-energy state to those in the low-energy state is:

Eq.80

Since the population difference is very small, the difference in populations that is measured in EPR above 4 K, is accurately approximated as $g_{\beta}B/2kT$. Since the energy level differences are very small, at X-band and above 4 K it is a reasonable approximation to say that the spin magnetic moment is:

Eq.81

Hence, relative intensities of signals that are not power saturated can be corrected for the Boltzmann population effect by multiplying by the ratio of the temperatures. The importance for quantitative EPR is that in variable temperature studies if all changes in Q, etc., have been accounted for, the EPR integrated intensity multiplied by the absolute temperature should be constant. This calculation is a good check to perform on VT EPR studies. Deviations could be due to violation of the assumption of independent spin behavior, or to partial saturation of some of the spectra. Large changes in temperature also result in changes in the bulk magnetization for interacting spin systems. Crippa et al. (1971) reported the temperature dependence of the integrated EPR intensity for DPPH, Varian pitch, and lignite. The ratio of the areas depends on the temperature because these samples exhibit different magnetic behaviors.

2.8 Line-Broadening-Shape Mechanisms Connection with Temperature

Some reasons of changing EPR spectral lineshape are the thermal effects and that's why under certain conditions, linewidths can vary with temperature, and from one line to another in a given spectrum. The result is a departure of the proportionality between the first-derivative amplitude and the line intensity since the derivative amplitude is inversely proportional to the square of the linewidth. Thus, small changes in linewidths can cause large changes in the relative amplitudes of various lines in the spectrum.

The paramagnetic electron spin-lattice relaxation time is an indicator of the strength of the thermal contact between the paramagnetic electron spin system and the heat reservoir, i.e., the lattice. REF

There are several mechanisms by which the spin-lattice interaction can take place in condensed phases and help in understanding the dependence of temperature versus the relaxation time.

They all involve interaction of the spin system with vibrations (phonons) of the lattice. The phonon density in the lattice obeys a Boltzmann distribution law. Thus, there is a slightly higher phonon density at the energy of the lower energy level than at the energy of the upper level. This is the origin of the inequality in the W probabilities. The detailed description of the specific interactions leading to τ_1 is beyond the scope of this book, but the following are some of the most important mechanisms:

The most important and most used mechanisms for such interactions leading to τ_1 are the following [53]:

1. ***Direct Process or Curie Process***. This involves direct phonon-assisted non-radiative transitions between the spin levels. In the high-temperature approximation ($hv/k_BT << 1$), which is valid for almost all experimental conditions, τ_1 is predicted to vary as $B^{-4}\ T^{-1}$ for S = 1/2 systems and as $B^{-2}\ T^{-1}$ for S > 1 2 systems. This mechanism is found to be dominant only at very low temperatures.
2. ***Raman Process***. As with Raman processes in electronic spectroscopy, this process involves 'virtual' excitation followed by deexcitation to phonon states much higher in energy than the spin levels. Depending on the details of the interaction, the temperature

dependence of τ_1 can vary from T^{-5} to T^{-9}, and thus this process becomes increasingly more important as the temperature increases.

3. ***Orbach Process.*** If a low-lying spin level exists at an energy Δ above the ground manifold, a Raman process involving that state can dominate the spin-lattice relaxation. In this case τ_1 is predicted to vary as $\exp(\Delta/k_BT)$, from which Δ can be obtained. This process was first described by Orbach.

DIRECT PROCESS

When a crystal lattice vibrates, the interatomic distances are modulated at the frequency of the lattice vibration, resulting in an oscillating magnetic field. Those lattice vibrations with a frequency at the Larmor frequency of the electrons can induce a flip of an electron spin. This process, referred to as the direct process, results in a spin-lattice relaxation rate given by [REF]

Eq.82

where ρ is the mass density, ν the oscillator frequency, u_0 the velocity of sound in crystal, r_0 the lattice separation and β the Bohr magneton. In order to connect the Equation 81 it follows that:

Eq.82

where H_0 is the magnitude of the external magnetic field. The direct process is a weak relaxation mechanism, since the acoustic spectrum of a solid at $\sim 10^{10}$ Hz is weak and acoustic waves of this frequency have long wavelengths, in contrast with the relatively small displacements of atoms. For example, in diamond the speed of sound is relatively high ($\sim$1.33 x 10^3 m/s) [54] and the u^5 dependence of the relaxation rate results in a low relaxation rate. Substituting the relevant values, yields $T_1 \approx 10^5$s at 4.3 K.

As a result, in the direct process where a single lattice phonon causes a flip of an electron, leading to a linear dependence of the relaxation rate on temperature when:

$$T >> \hbar\omega_0 / k$$

where ω_0 is the electron Larmor frequency as mentioned earlier. Depending on the details of the interaction, the temperature dependence of τ_1 is T^{-1} as shown in Figure 20a.

RAMAN PROCESS

The Raman process or two-photon process involves the inelastic scattering of a higher frequency lattice phonon by the flipping electron spin. when a phonon n is scattered by a paramagnetic impurity, and the difference between initial and final phonon energies is equal to $\hbar\omega_0$. The relaxation rate is proportional to the seventh power of the temperature below the Debye temperature [55], but within a multiplet of closely spaced levels, the relaxation rate could be proportional to the fifth power of the temperature. At temperatures $T<<\theta_D$, where θ_D is the Debye temperature of the crystal the relaxation time rate is given by:

Eq.83

The relaxation rate is now proportional to the tenth power of the speed of sound in the crystal. For example, for diamond, in order to understand the difference of mechanisms, the relatively high speed of sound will result in a relatively low relaxation rate for the Raman process. Substitution of the relevant values yields $T_1 \approx 100$ s at 300 K. Depending on the details of the interaction, the temperature dependence of τ_1 can vary from T^{-5} to T^{-9} as shown in Figure 20b.

ORBAN PROCESS

The Orbach process could be effective in systems with more than two energy levels [47]. A phonon with energy Δ results in a transition between two energy levels with a separation Δ. The electron then makes a transition to a level with an energy $\Delta+\omega_0$ lower than that of the previous level and a phonon with energy $\Delta+\omega_0$ is emitted. The relaxation rate is given by:

Eq.84

where K is a constant.

Depending on the details of the interaction, the temperature dependence of τ_1 can vary from T^{-9} to T^{-11} as shown in Figure 20c.

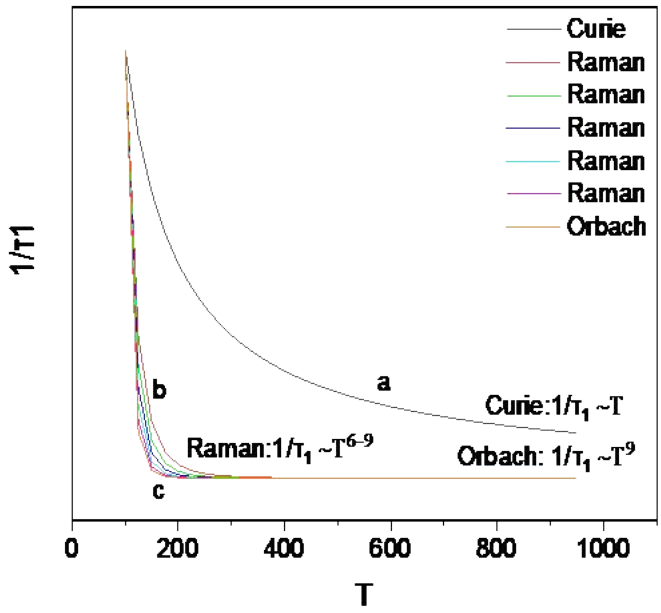

Figure 20: Relaxation time plotted as a function of temperature for the most common mechanism where (a) is for the Curie or direct process mechanism, (b) is for the Raman process from T^{-5} to T^{-9} and (c) is for the Orbach mechanism as explained.

For the analysis of a High Temperature EPR spectrum there are several key-parameters that have to be considered. Those parameters are presented below:

- **The linewidth change (*ΔH*),**
- **lineshape factor ($S_{L/G}$ Lorentzian/Gaussian factor) change,**
- **the signal's intensity (*I*) change.**

We will show in figures the meaning of those factors and the differences for each one in order to connect that information with our experimental data.

First of all, in an EPR spectrum the change on the linewidth can give us a lot information about the material. Overall, at the High Temperature EPR the increase of temperature the linewidth surely will change and the temperature region where that change becomes apparent as T approaches the T_N [56], the size of the linewidth change might be from some Gauss up to hundreds of Gauss as shown in Figure 21, where two H.T EPR spectrums are presented. The black one is at room temperature (300K) and the red one is measured in-situ at 450K. It is an important factor in

determining whether or not, in a crystal of a given magnetic symmetry, where a critical-like divergence will be manifest.

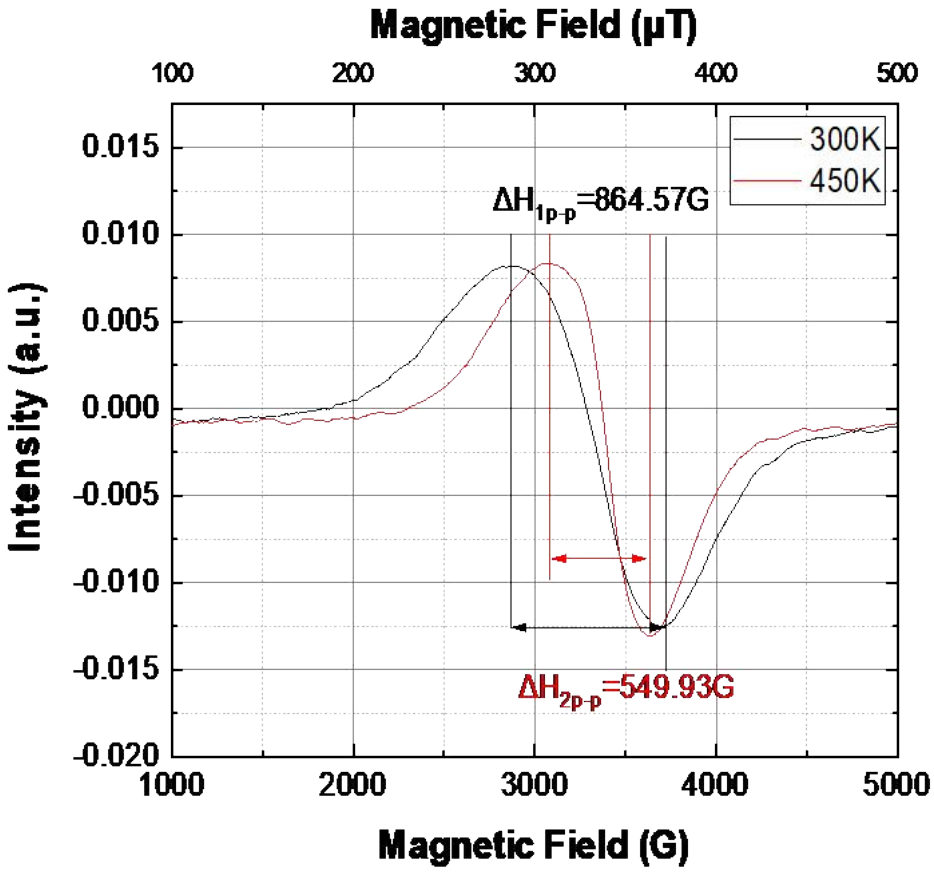

Figure 21: In this Figure we show the change of one of the factors-parameters in a material due to the temperature change as it starts from room temperature and moving to the 450K, the linewidth is changing from 864.57G to 549.93G where the black is at RT and the red at 450K.

For the other two factors we have to take in account other parameters too, like spin dynamics as mentioned before. As for the intensity, in the simplest case where there are no spin dynamics and when we have isolated spins the signal's intensity is the difference of spin populations as we showed earlier in the static case of dynamics as shown in the equation XXXXX. In order for that to be more understandable we constructed some figures to explain the changes of spin populations as shown in Figures 22 (a-c). In these figures we show graphically that the difference of the populations increases or decreases signal's intensity, i.e. when the "upper"

populations are max the maximum signal intensity is received by the detector and when they are equal, i.e. their difference is equal to zero, the signal is also zero.

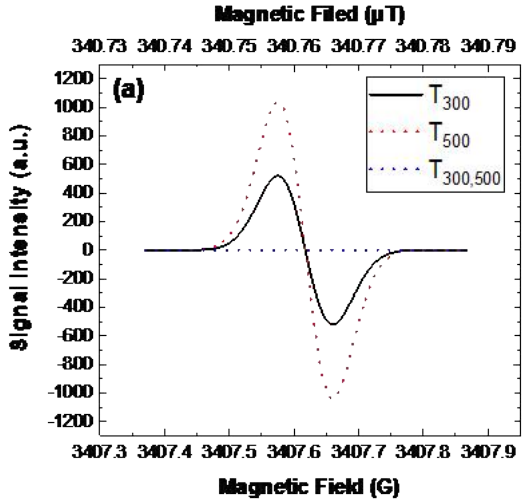

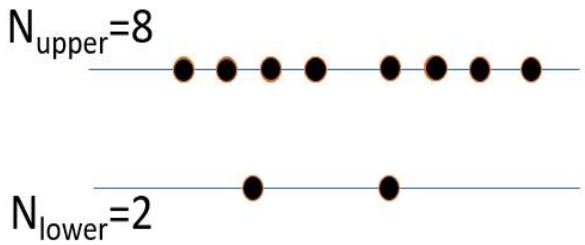

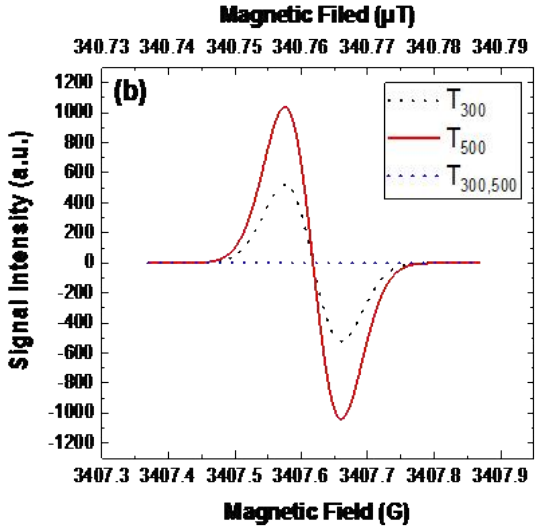

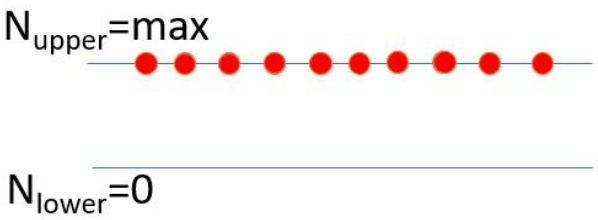

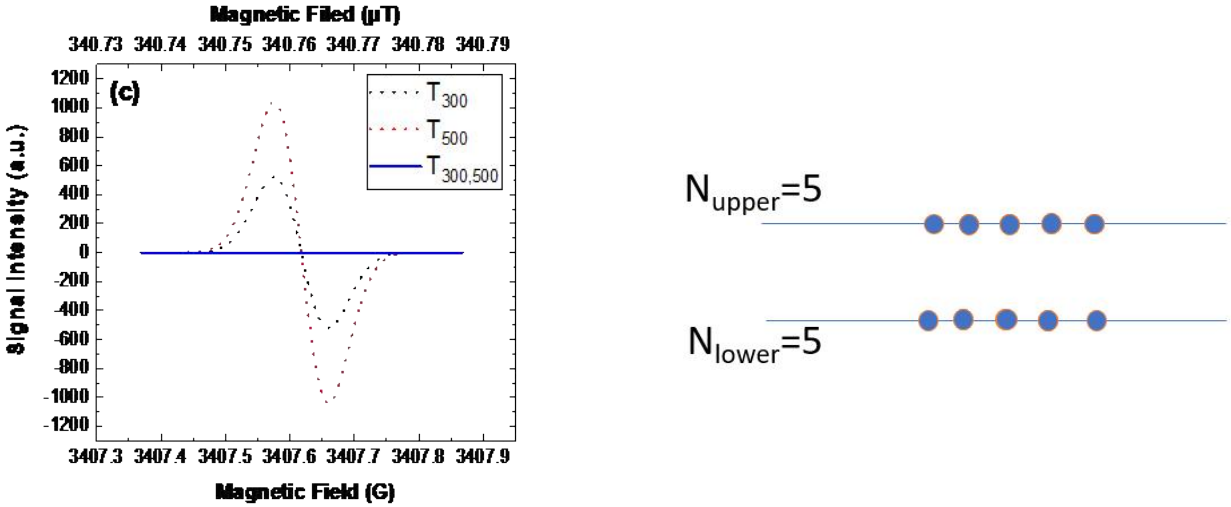

Figure 22: In this series of Figures a-c we show the change of intensity versus the difference of spin populations in (a) we demonstrate the case of measuring at RT, in (b) we demonstrate the case where we have a system (like ferromagnetic materials) in which with the increase of the temperature the difference population is getting to its peak and we have increased signal's intensity the same figure could be used for 4K with he difference that the signal will be bigger, in (c) we have the case in which the temperature doesn't matter because the spin populations is equal to zero and so the absorption will be zero and so the first derivative which is the signal. Its case is a simulation to show the importance of the difference between spin populations.

It has been proved via the Figure 22 that the temperature changes may not change the H.T. EPR signal but the difference of spin populations may increase it or decrease it, that's happening in a system though with isolated spins in a matrix for example in natural marble. In all systems though when temperature is decreasing down to 4K the signal's intensity is increasing while temperature is increasing the signal's intensity will be smaller that's because of the populations difference and the relaxation time of the system, as shown in Figure 23 below.

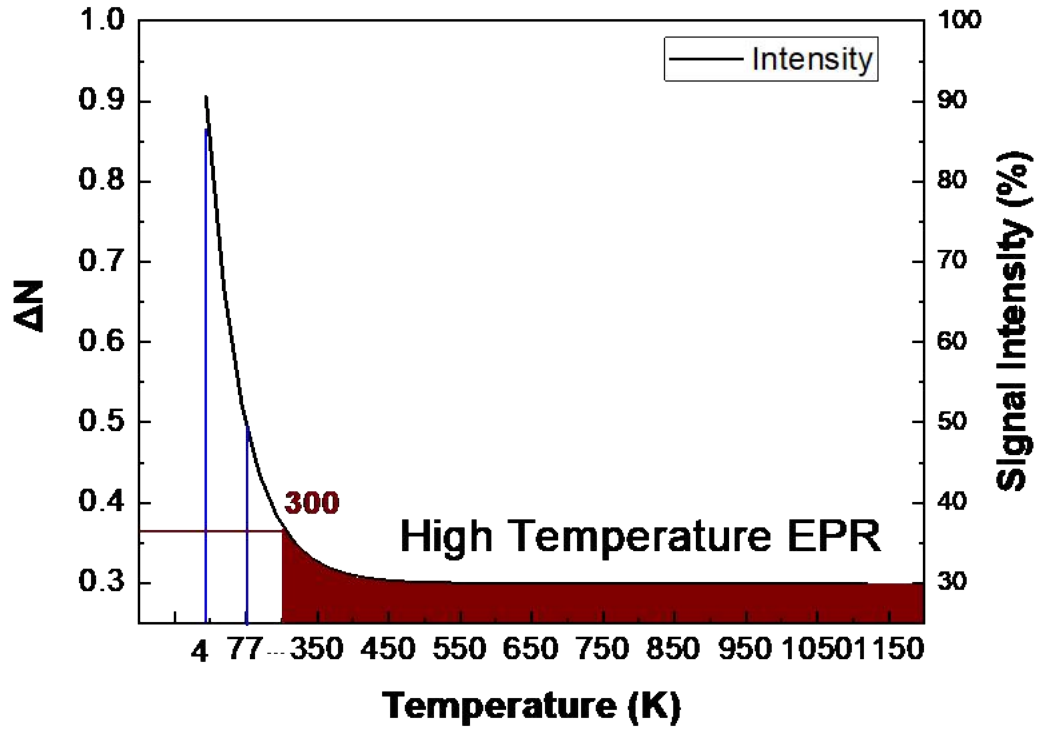

Figure 23: In this Figure we show the dependence of temperature versus signal intensity, which is dependent of the difference of populations as we explained in Figure 22, also here we can see that when we measure in 4K we receive the 0.9 or 90% of maximum signal intensity because the relaxation time is smaller and the difference of spin populations is bigger, while in RT the intensity is much smaller because the relaxation time is faster and the difference of spin populations is smaller. The line that each material follows depends on the material, for example a radical will get destroyed near 360K (depending on the radical), near its melting point the intensity will be near zero because the rings will get destroyed, a marble for example with melting point 1100K will have a curve like the one shown here in which the line will start to decrease in a temperature near Neel's temperature point.

Now in our set-up we are able to control digitally all that temperature range starting from room temperature and up to 1350K. In our results we will show some materials that follow that line. Its important to understand the case we investigate and what to expect and at which point of temperature. We can take many information by all the parameters that we analyze here. The intensity factor versus temperature will be discussed in Figure 24.

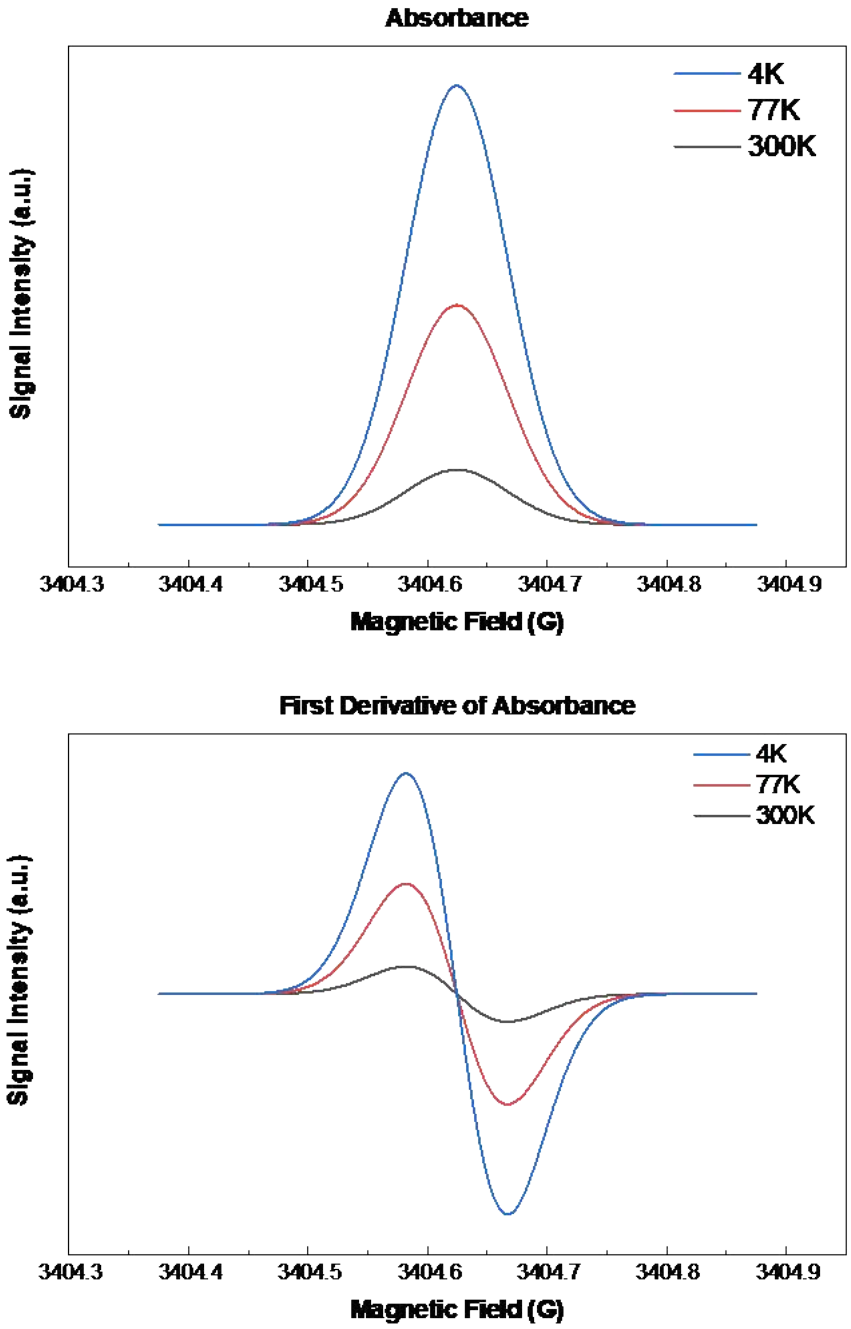

Figure 24: An EPR simulated spectrum which shows the absorbance (first) in three different temperatures, 4K, 77K and 300K. Below the first derivative of absorbance is presented as the signal that we would take in real EPR experiment.

The total lineshape of an EPR signal can be a Gaus, a Lorentzian or a mix of both, in general. That's because every spin has a Lorentzian character and lineshape. Let's assume that we have a material which at a constant temperature, the spin populations are matched like those at the Figure 25 below. For the example we chose three packs of spins A, B and C, in order to simulate each signal of those packs.

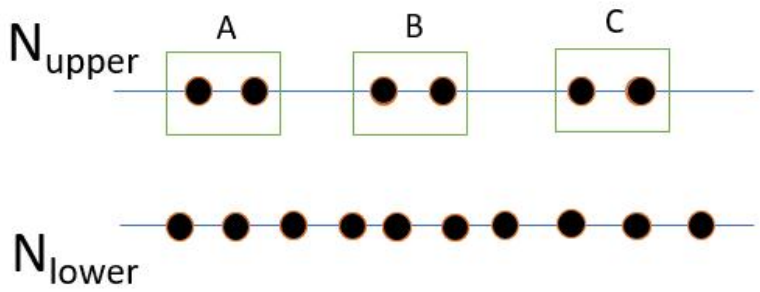

Figure 25: In this Figure we show a case of difference of populations at constant temperature, in order to show the changing of lineshape, therefore three packs of spins A, B and C, in order to simulate each signal of those packs in next Figure 26.

Therefore, the difference of spin populations will give a signal at the EPR spectrum at a constant temperature. For that example, the center of resonance will be 3405.9G we expect three different Lorentzian lines for each one of the three different packages of spins. Depending of how far the spin packages are from resonance center they will behavior as a Gaus or as a Lorentz or as a mix of them. In order to represent those two more figures were made Figure 26 and Figure 27. In each of those figures the first graph is the absorbance for each one of those spin packages (A, B, C) and the total of them is the simulated signal, then the second graph in each figure is the first derivative of total signal of the absorbance. In Figure 26 each one of the spin packages has a Lorentzian character but A and C have a shift from the resonance center because of that shift the lineshape of the total signal, even if each one of the packages is Lorentzian, will be Gauss. In Figure 27 as earlier each one of the spin packages has a Lorentzian character but now A and C have a much smaller shift than in Figure 26 from the resonance center because of that shift the lineshape of the total signal, even if each one of the packages is Lorentzian, will be more Lorentz shaped.

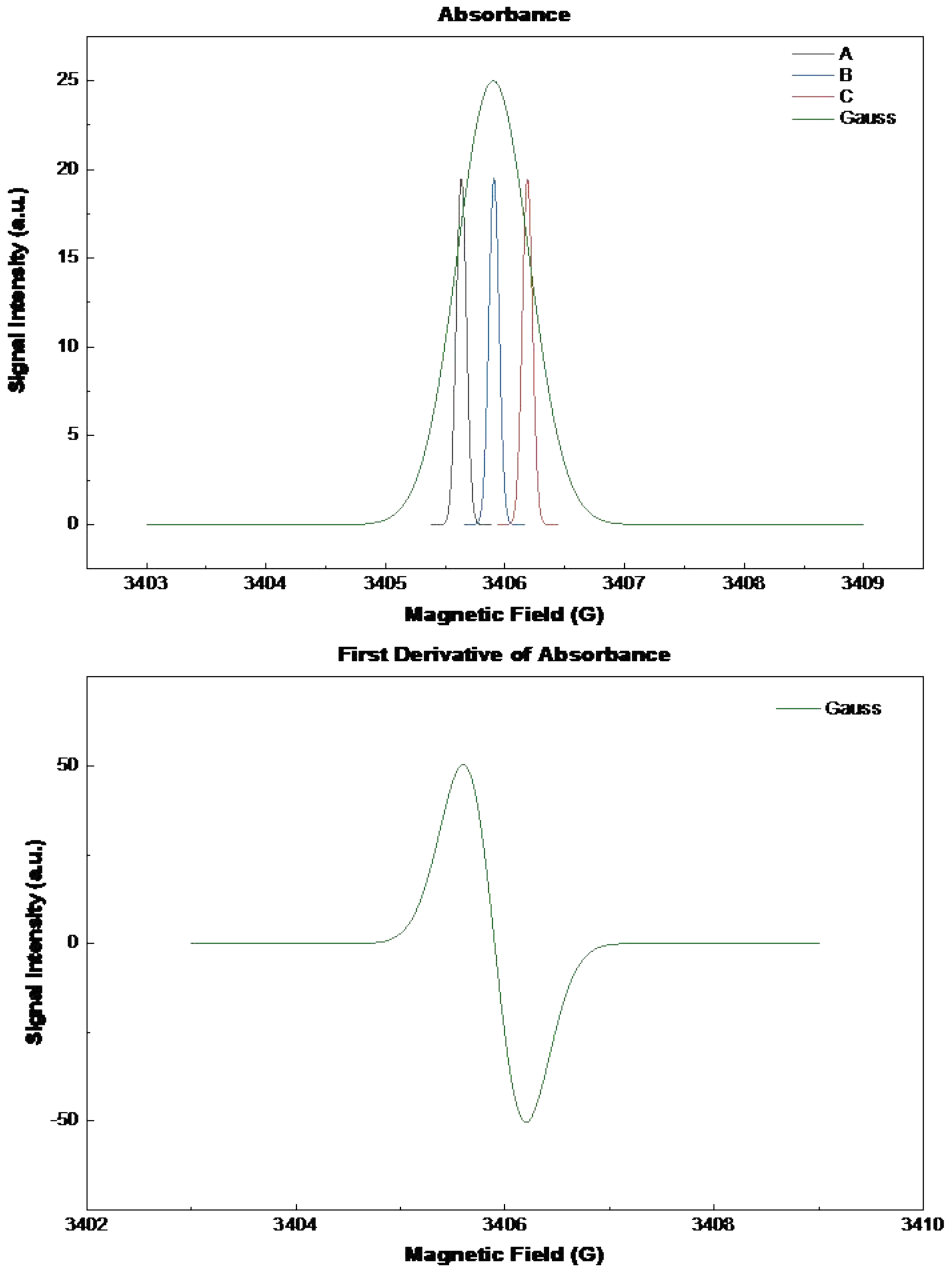

Figure 26: In this Figure we present the importance of the distance from the resonance for three groups of spin packages where they are separated and even if each one of those has a Lorentz character they behave as a Gauss afterall.

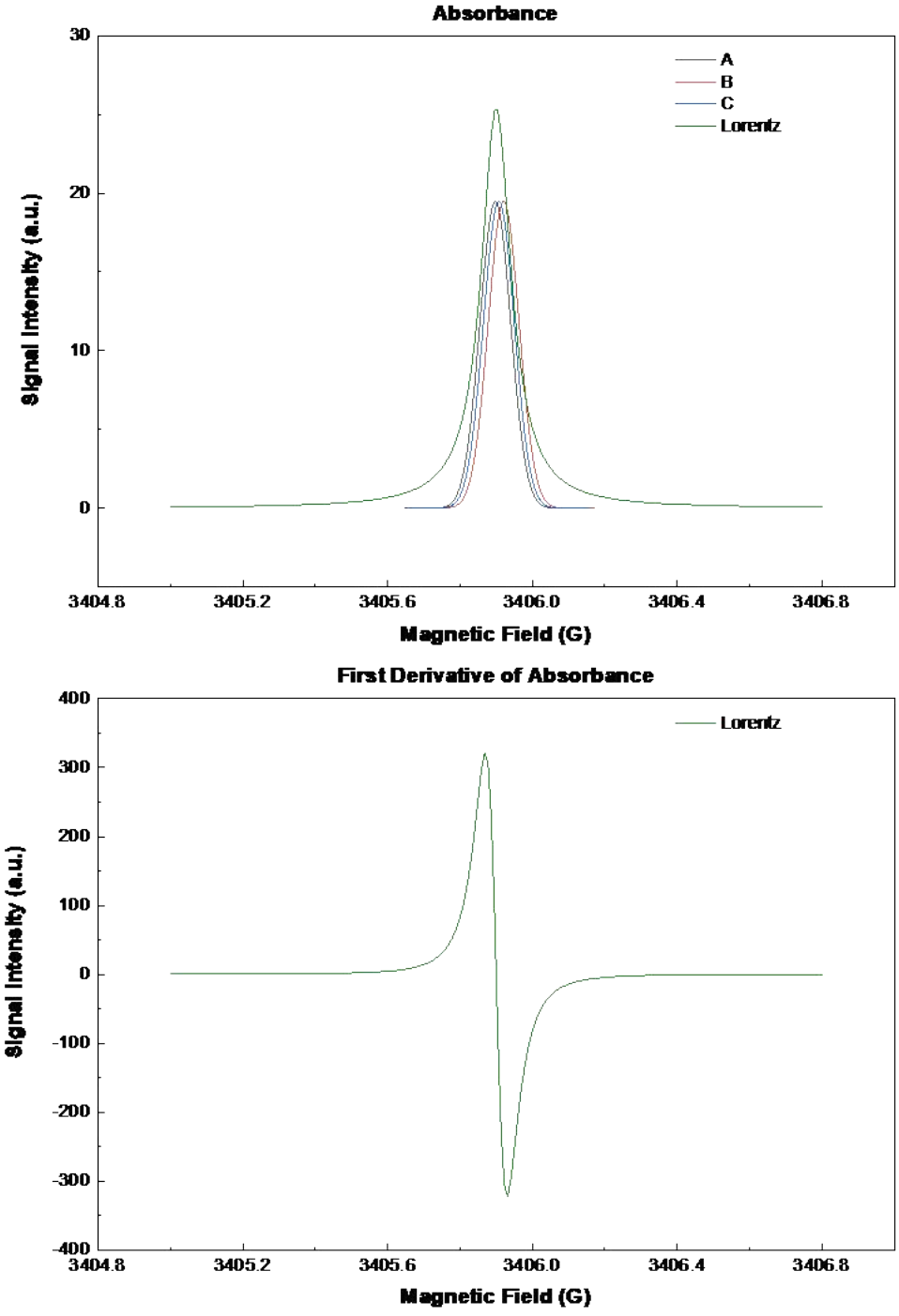

Figure 26: In this Figure we present the importance of the distance from the resonance for three groups of spin packages where they are not separated and each one of those has a Lorentz character, they keep the lineshape and behave as a Lorrentzian afterall.

Earlier we took the simplest case where spins are isolated and there are no spin dynamics. The structure and widths of EPR lines provide information on the amplitude and spectral density of the local field fluctuations from which certain characteristic properties of the electronic spin correlation functions in dense magnetic systems may be inferred. Now in the opposite case of non-stable spin dynamics and spin hopping, which is happening in high density spin systems, when there are spin domains in the material and when the lattice is loose. In that case the following Figures 27 and 28 will represent the changes of the signal peaks on the spectrum because of the change of resonant magnetic field versus temperature. The first figure 27 is for the case of 4K where the spins are "still" and we have three signals in the absorption (a, b, c). In that case as we described earlier the intensity will be higher and has a Gaussian lineshape.

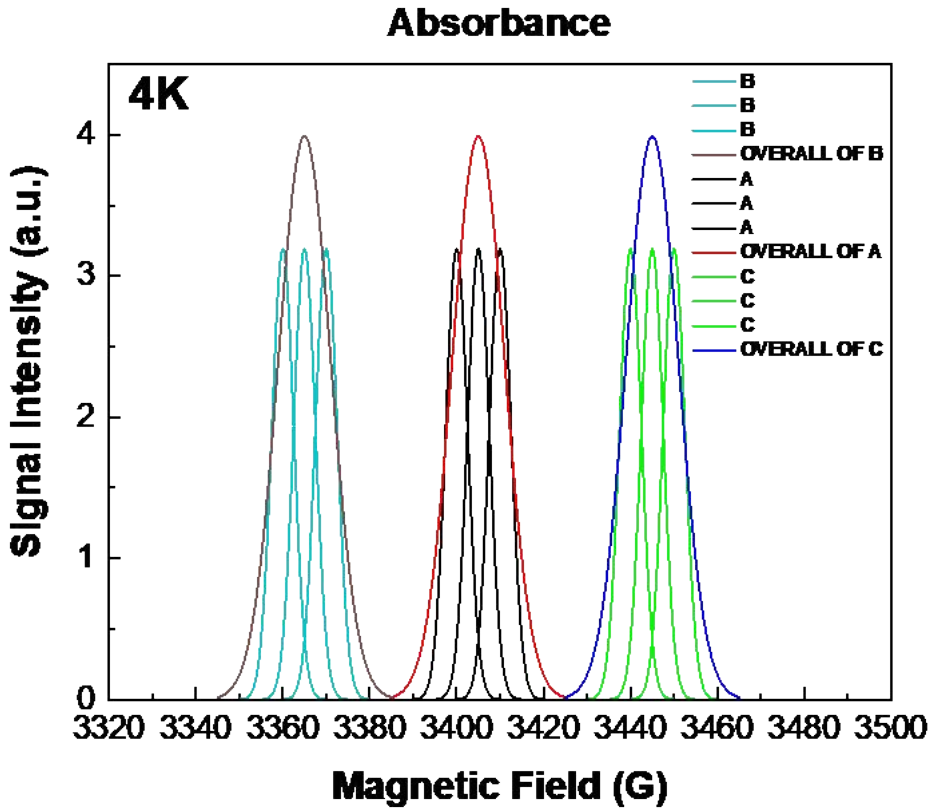

Figure 27: Here we represent the case where we have spin-spin interactions and as we did earlier we take three packages (a, b, c). Again, each one of spins have a Lorentzian-shape character and depending how far they are they behave as Lorentz or Gauss.

At 77K where most of the spins are "still" and we have three signals in the absorption (a, b, c) and the spins start to be a little more mobile than at 4K. In that case as we described earlier the intensity will be higher. The intensity is lower than before, but it keeps the same Gauss lineshape. Also, at 300K we have even lower intensity and more mobile spins which will reduce the signal's intensity but still it will keep a Gauss characteristic lineshape. With the increase of the temperature, the signal intensity is reducing that's something that we discussed about earlier but what changes is that at high temperature the lineshape can change from a Gauss lineshape to a Lorentz lineshape, that's because at high temperatures spins are merging around the resonant magnetic field and they create a Lorentz character. In the Figure 28 below we show that change by showing a simulated curve and because of the merging at 700K the intensity is increasing until a melting point or until there is an increment population difference (intensity) and because of the shift (ΔH).

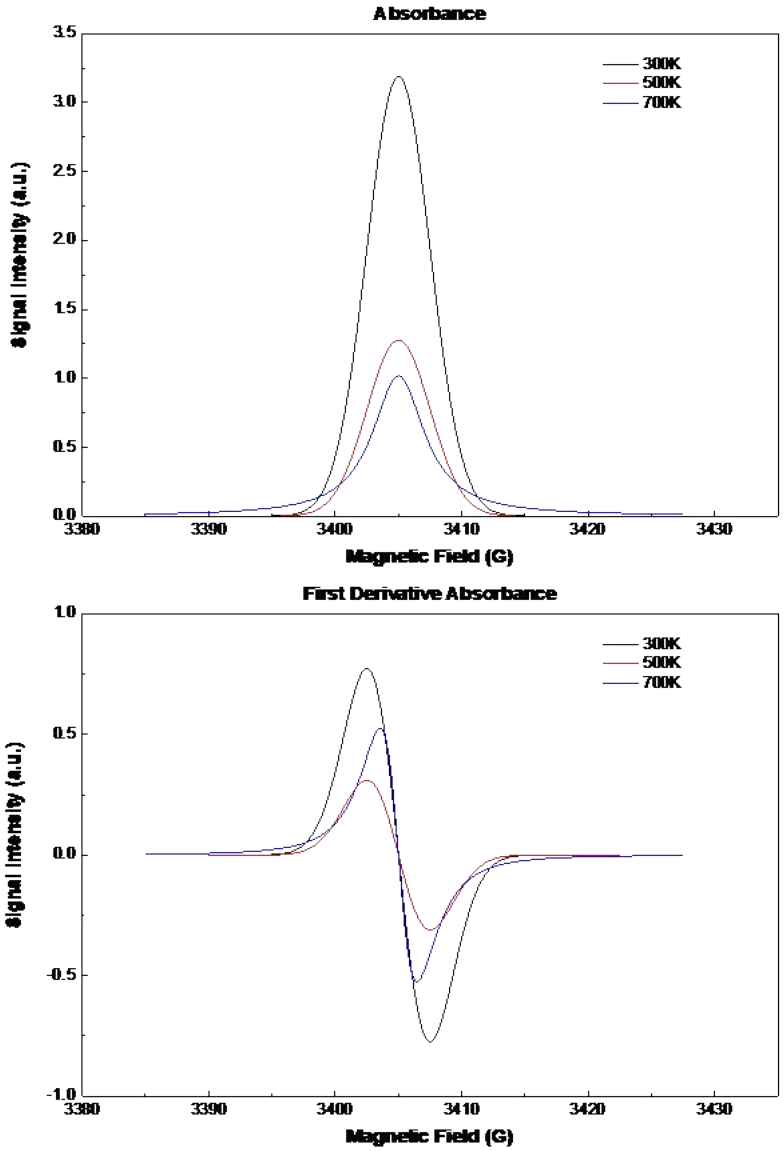

Figure 28: In that Figure we show the change of simulated curves because merging starting from 300K up to 700K. The intensity is increasing until a melting point or until there is an increment population difference (intensity) and because of the shift (ΔH).

In the case of systems with magnetic behavior, which are consisting of isolated single-domain particles depends on the relative magnitude of the thermal energy with respect to the anisotropic part of the magnetic energy of the particles. When these two energies are comparable, the direction of magnetization of the particles undergoes thermal fluctuations. {Berger 1977 REF} In a system

for example where we have small particles in a diamagnetic matrix three kinds of interactions are applied: a) with matrix, b) with other particles, c) with the applied filed. Interactions with the diamagnetic matrix are essentially nonmagnetic and thus have no direct effect on the resonance phenomenon. However, the matrix does play an important role; it keeps the particles in place, so that they cannot rotate when an external field is applied. Therefore, the magnetic resonance behavior of the system is different from that of an assembly of "free" magnetic particles. When ferromagnetic single-domain nanoparticles are dispersed in a diamagnetic matrix, a specific type of magnetic behavior, called superparamagnetism is observed [57]. Nanoparticles of relatively greater sizes may incorporate several magnetic domains; however, below ca. 10 nm they are typically single-domain particles [57]–[59] We consider a statistical assembly of disordered single-domain magnetic nanoparticles whose characteristics vary from one particle to another. At room temperature each magnetic domain has a different magnetic momentum orientation, however with the increase of the temperature the spins in the domains start to reorientate as shown in Figure 29.

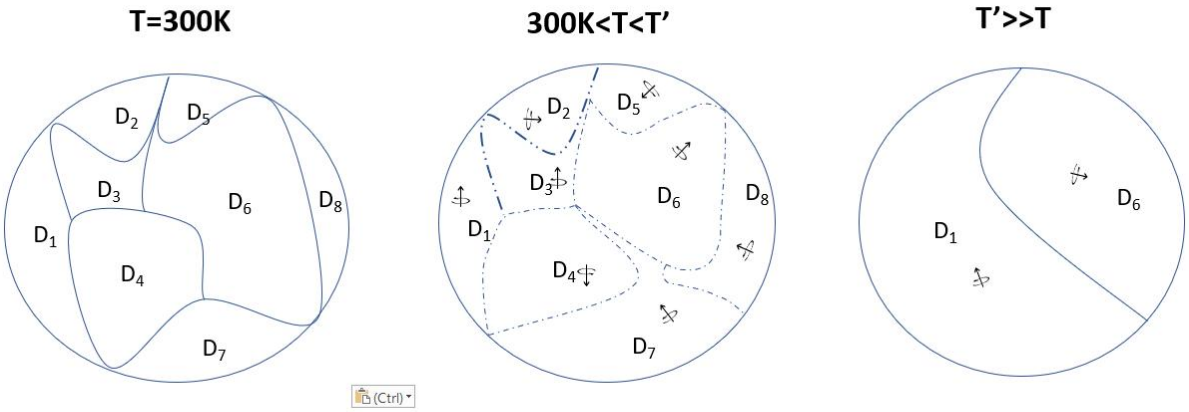

Figure 29: Here we show a ferromagnetic material which has spin domains. According to Berger those materials are separated in to domains with each domain having a different orientation. In this figure for example we start at RT by having 8 different spin domains and we see that with the increase of temperature they start to reorientate until a T'>>T where they are made two different domains. That will increase intensity of course.

At T′ temperature bigger than room's they are separated in two domains and if an increase of the difference of populations exists the signal's intensity is enhanced. We have to note that at the last step where there are only two domains the signal, we have a Lorentz lineshape for reasons that we discussed earlier. In Figure 29 we demonstrated a particle with separate spin domains as shown in

Figure 30 that's a typical EPR spectrum for a ferromagnetic material, as we can see it has a Gauss Lineshape and the signal is broad.

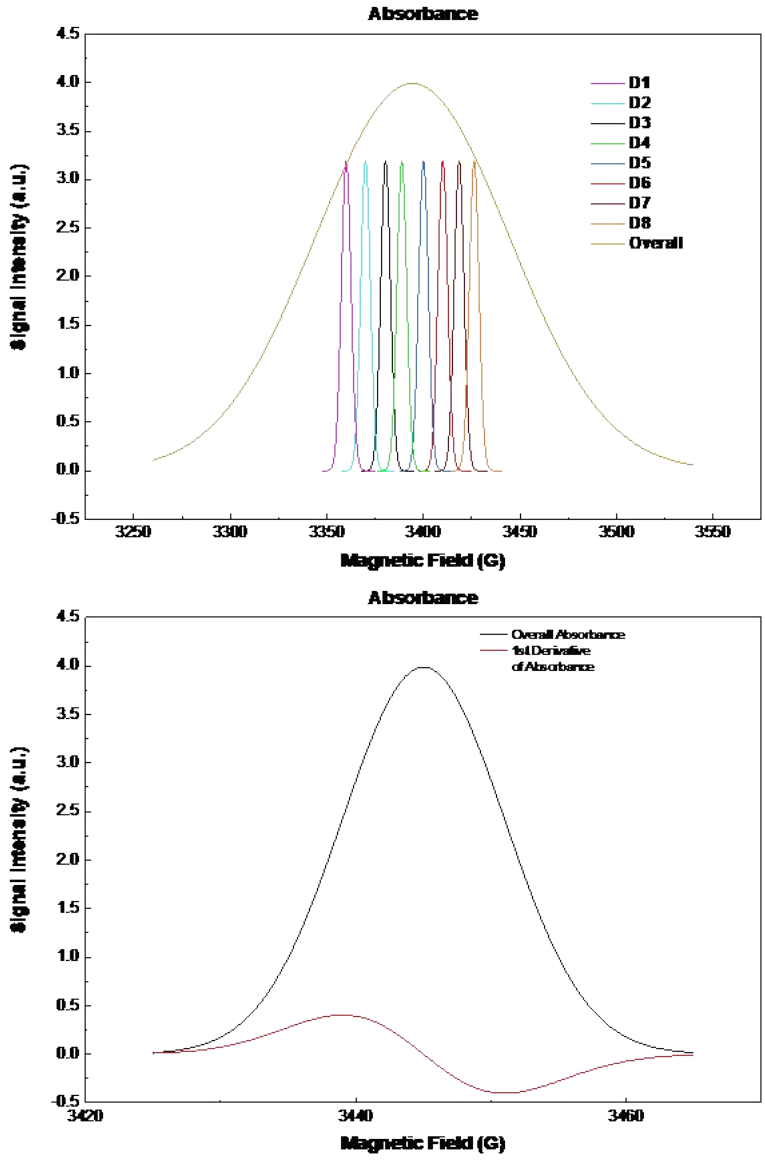

Figure 30: Here we present a simulated signal in which we represent each domain as having Lorentz shape line (just for the case, normally it would be a mix of Gauss and Lorentz) as we showed earlier in Figure 26.

With increase of temperature the spin domains merge as shown in Figure 31 and the lineshape turns from Gauss to Lorentz lineshape because of the spin hopping and the intensity increase because the

difference of population increases too until a point. At Figure 31 we also show the absorbance and the first derivative of an EPR spectrum at room temperature and at a higher temperature.

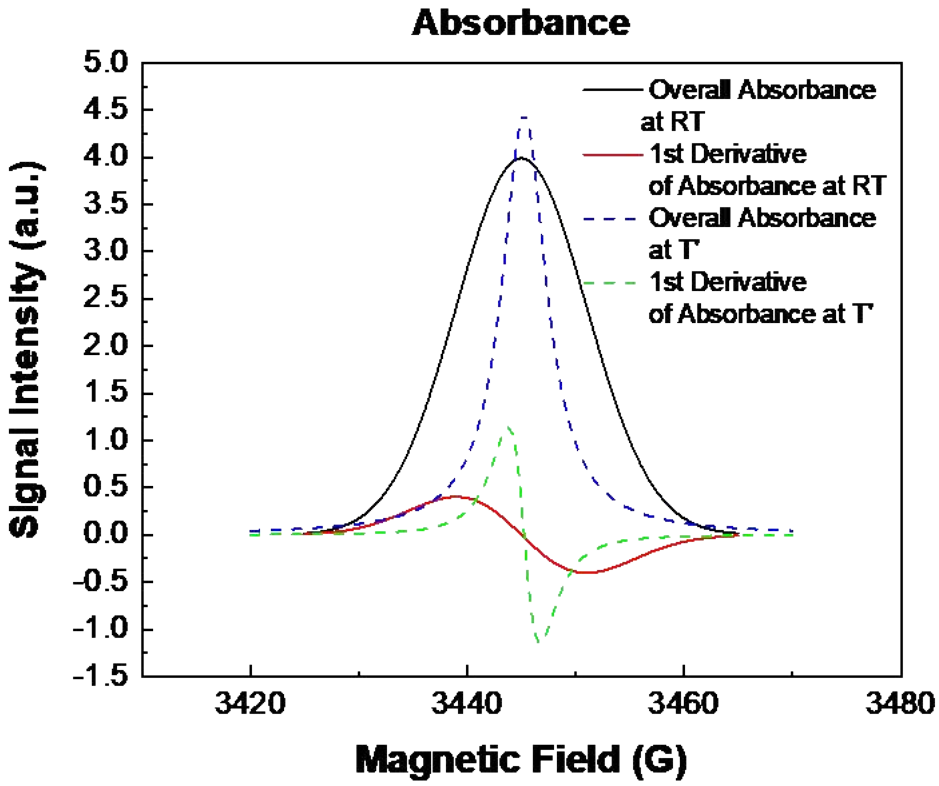

Figure 31: In this figure we present a simulated H.T. EPR spectrum. More specifically it's a spectrum for a ferromagnetic material, with spin domains as explained earlier. We start from a signal at RT and we increase the temperature in that case the domains are reorientated and the intensity of the signal is getting higher. We also present the absorbance lines for both RT and T'.

Therefore, we analyzed every parameter that can be recorded from an EPR spectrum with simulated signals for simplicity.

CHAPTER 3

3 EPR Spectrometer Set-Up

The "normal" Zeeman effect was well-known in optical spectroscopy for many years but the components to build an EPR were more advanced. Each spectrometer has three essential components: a source of electromagnetic radiation, a sample and a detector. To acquire a spectrum, we change the frequency of the electromagnetic radiation and measure the amount of radiation which passes through the sample with a detector to observe the spectroscopic absorptions. Despite the apparent complexities of any spectrometer that is the basic idea. In general, EPR layout spectrometer contains a microwave bridge, the microwave cavity, an electromagnet the sample and a main console. The electromagnetic radiation source and the detector are in a box called the "microwave bridge" as shown in Figure 32. The sample is in a microwave cavity, which is a metal box that helps to amplify weak signals from the sample. There is the electromagnet to tune the electronic energy levels. In addition, we have a console, which contains signal processing and control electronics and a computer. The computer is used for analyzing data as well as coordinating all the units for acquiring a spectrum.

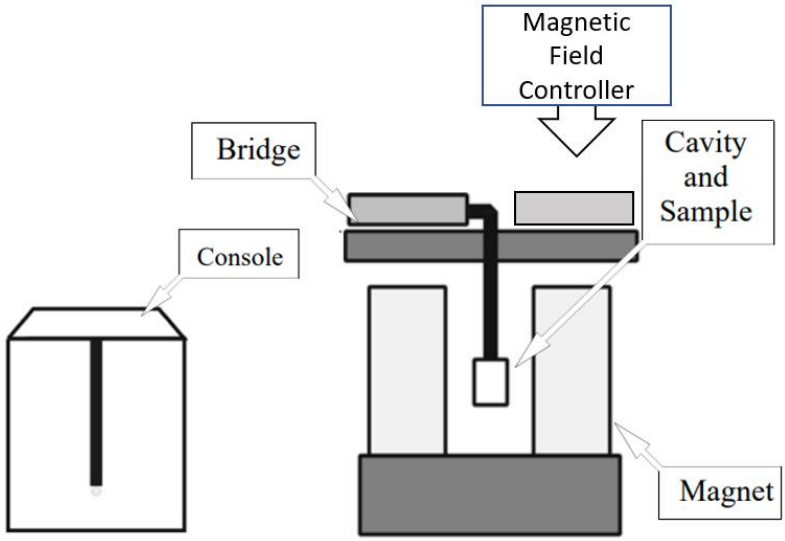

Figure 32: Diagram of a typical EPR spectrometer with the most important parts.

3.1 The Microwave Bridge

In the case of the EPR both detector and source are in the microwave bridge. In a bridge there are more parts than shown in Figure 33, but most of them are for control, power supply, and security electronics of the bridge.

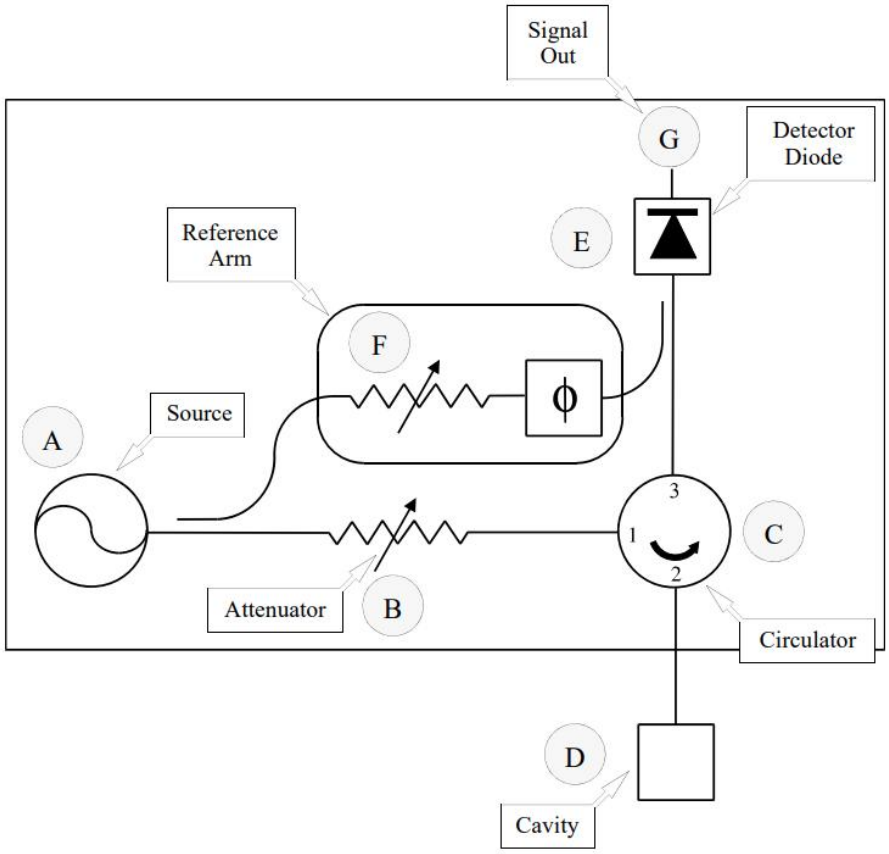

Figure 33: Block diagram of a typical microwave bridge, where the most important parts of the set up are installed.

From the block diagram at point A is the microwave source, that can't be varied easily, that's why we need the second point, B where is the variable attenuator, a device which blocks the flow of microwave radiation. With the attenuator, we can precisely and accurately control the microwave power which the sample sees. Most EPR spectrometers are reflection spectrometers (which means that it measures the amount of radiation that is reflected from the sample) that happens by measuring the changes (due to spectroscopic transitions) in the amount of radiation reflected from the microwave cavity containing the sample (point D in the figure). We therefore want our detector

to see only the microwave radiation coming back from the cavity. The circulator at point C is a microwave device which allows us to do this. Microwaves coming in port 1 of the circulator only go to the cavity through port 2 and not directly to the detector through port 3. Reflected microwaves are directed only to the detector and not back to the microwave source. In point E we use a Schottky barrier diode to detect those reflected microwaves and convers the microwave power to an electrical current. At low power levels, (less than 1 microwatt) the diode current is proportional to the microwave power and the detector is called a square law detector. That's because electrical power is proportional to the square of the voltage or current.) At higher power levels, (greater than 1 milliwatt) the diode current is proportional to the square root of the microwave power and the detector is called a linear detector. The transition between the two regions is very gradual. As in most electronics the diode should operate in the linear region in order to have the optimal sensitivity, for that detector the best results are taken when the detector's current is approximately to 200 μA. To ensure that the detector operates there or very close to that current there is a reference arm, which is at point F of the block diagram which supplies the detector with some extra microwave power or "bias". Some of the source power is tapped off into the reference arm, where a second attenuator controls the power level (and consequently the diode current) for optimal performance. There is also a phase shifter to ensure that the reference arm microwaves are in phase with the reflected signal microwaves when the two signals combine at the detector diode. The detector diodes are very sensitive to damage from excessive microwave power and will slowly lose their sensitivity. To prevent this from happening, there is protection circuitry in the bridge which monitors the current from the

diode. When the current exceeds 400 μA, the bridge automatically protects the diode by lowering the microwave power level this protection circuit reduces the risk of damage due to accidents or improper operating procedures.

For technical reasons, every microwave source (Klystron, Gunn) has a maximum peak at its performance at a very narrow frequency range e.g. 9.00± 0.05 GHz. So every spectrometer EPR is characterized from its working frequency of its microwave source. Nowadays there are categories of EPR spectrometers and some high field EPR spectrometers that go above 100 GHz as shown in Table 2:

Working Frequency (GHz)	***Name***
1-2	*L-band*
2-3	*S-band*
9-10	*X-band*
15-18	*P-band*
24-30	*K-band*
32-35	*Q-band*
90-95	*W-band*
140-150	*D-band*
285 -290	*J-band*

Table 2: The main categories of EPR spectrometers categorized based on their working frequency.

Most of the EPR spectrometers are working at the X-band and for that thesis we will work on that band. In our case we use a microwave of 9-10GHz frequency or 3cm-[1] wavelength and it's a Klystron type.

3.2 The EPR Cavity

In this section, we shall discuss the properties of microwave (EPR) cavities and how changes in these properties due to absorption result in an EPR signal. The microwave cavities are used to amplify weak signals from the sample. A microwave cavity is a metal box with a rectangular or cylindrical shape which resonates with microwaves much as an organ pipe resonates with sound waves. Resonance means that the cavity stores the microwave energy; therefore, at the resonance frequency of the cavity, no microwaves will be reflected, but will remain inside the cavity. (See Figure 34)

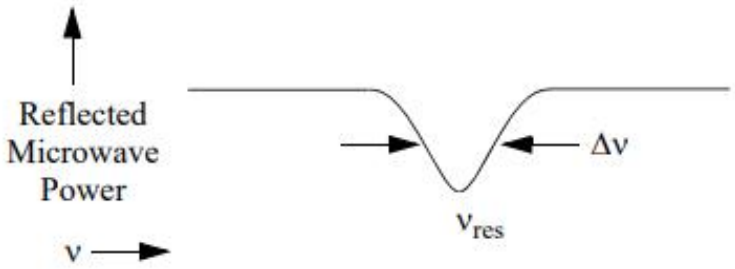

Figure 34: Reflected microwave power from a resonant cavity.

Cavities are characterized by their Q or quality factor, which indicates how efficiently the cavity stores microwave energy. As Q increases, the sensitivity of the spectrometer increases. The Q factor is defined as shown in Equation 85:

Eq.85

where the energy dissipated per cycle is the amount of energy lost during one microwave period. Energy can be lost to the side walls of the cavity because the microwaves generate electrical currents in the side walls of the cavity which in turn generates heat. We can measure Q factors easily because there is another way of expressing Q:

Eq.86

where ν_{res} is the resonant frequency of the cavity and $\Delta\nu$ is the width at half height of the resonance. A consequence of resonance is that there will be a standing wave inside the cavity. Standing electromagnetic waves have their electric and magnetic field components exactly out of phase, i.e. where the magnetic field is maximum, the electric field is minimum and vice versa. The spatial distribution of the amplitudes of the electric and magnetic fields in the most used EPR cavity is shown in Figure 35.

It is the microwave magnetic field (B_1) that induces the EPR transitions that are detected in EPR spectroscopy. Also associated with B_1 is the microwave electric field (E_1). The E_1 can induce rotational transitions in the sample, thereby generating heat. This phenomenon is the same from the effects of a microwave oven on food. This microwave absorption contributes to additional energy

dissipation and thereby reduces the resonator Q. To avoid excessive interaction of the sample with the E_1 field (and resultant Q lowering), it is important to position [60] the sample in a region of the cavity with high B_1 and low E_1. For cavities, there is a natural separation between B_1 and E_1 because upon resonance, a standing wave is excited within the cavity. Standing electromagnetic waves have their electric and magnetic field components exactly out of phase, i.e. where the magnetic field is maximum, the electric field is minimum and vice versa.

We can use the spatial separation of the electric and magnetic fields in a cavity to great advantage. Most samples have non-resonant absorption of the microwaves via the electric field (this is how a microwave oven works) and the Q will be degraded by an increase in the dissipated energy. It is the magnetic field that drives the absorption in EPR. Therefore, if we place our sample in the electric field minimum and the magnetic field maximum, we obtain the biggest signals and the highest sensitivity. The cavities are designed for optimal placement of the sample. We couple the microwaves into the cavity via a hole called an iris. The size of the iris controls the number of microwaves which will be reflected back from the cavity and how much will enter the cavity. The iris accomplishes this by carefully matching or transforming the impedances (the resistance to the waves) of the cavity and the waveguide (a rectangular pipe used to carry microwaves). There is an iris screw in front of the iris which allows us to adjust the "matching". This adjustment can be visualized by noting that as the screw moves up and down, it effectively changes the size of the iris. (See Figure 36)

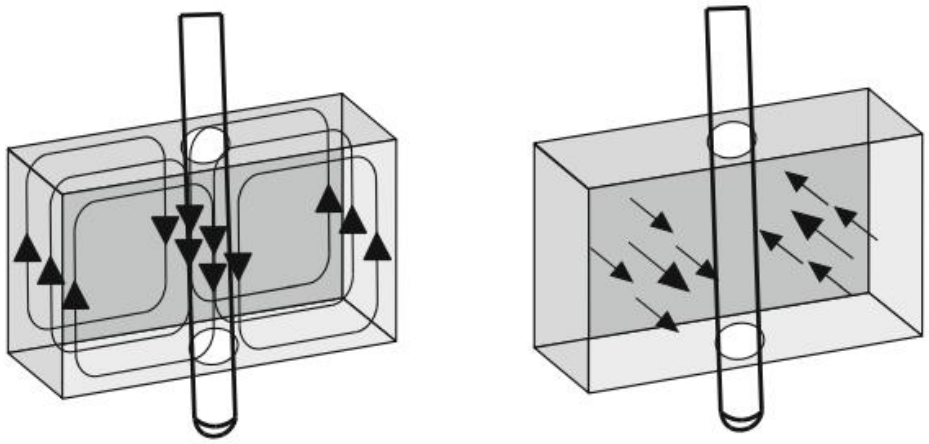

Figure 35: Magnetic and electric field patterns in a standard EPR cavity.

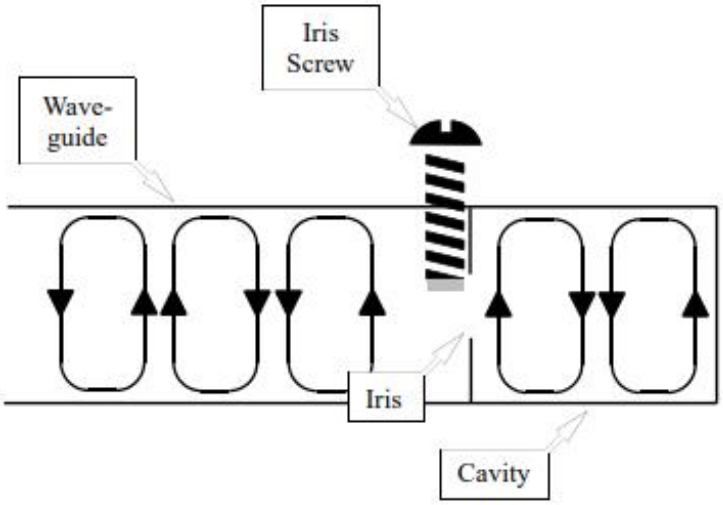

Figure 36: The matching of a microwave cavity to waveguide.

All these properties of a cavity give rise to an EPR signal, because when the sample absorbs the microwave energy, the Q is lowered because of the increased losses and the coupling changes because the absorbing sample changes the impedance of the cavity. The cavity is therefore no longer critically coupled and microwave will be reflected back to the bridge, resulting in an EPR signal.

3.3 The Magnetic Field Controller & Magnet

The magnetic field controller permits the operator to establish the DC magnetic field magnitude and range of magnetic field sweep in which an EPR signal is expected. The field controller provides the operator interface to the magnetic field current regulator and power supply. The desired field value, specified by the operator in units of Gauss, is translated into the appropriate signals for current regulation.

Field controllers use the Hall effect in order to establish and monitor the magnetic field intensity that is generated by the current flowing through the magnet pole windings. An external magnetic field $\boldsymbol{H}$ will generate a potential $\boldsymbol{V}$, across a Hall device by displacing current $\boldsymbol{I}$, flowing in the plane orthogonal to the Hall plate. The potential generated can be represented by Equation 87:

Eq.87

where ***R*** is a proportionality constant which depends on the geometry and material of the Hall element. A control voltage, generated by comparing the measured Hall voltage to a reference voltage established for the desired field value, is used by the magnet power supply to determine the current level flowing through the magnet. The Hall potential has a temperature coefficient, but this effect is compensated by calibration and use of a thermostat to control the temperature.

The magnetic field controller allows us to sweep the magnetic field in a controlled and precise manner for our EPR experiment. It consists of two parts; a part which sets the field values and the timing of the field sweep and a part which regulates the current in the windings of the magnet to attain the requested magnetic field value.

The magnetic field values and the timing of the magnetic field sweep are controlled by a microprocessor in the controller. A field sweep is divided into a minimum of 512 and a maximum of 4096 discrete steps called sweep addresses. At each step, a reference voltage corresponding to the magnetic field value is sent to the part of the controller that regulates the magnetic field. The sweep rate is controlled by varying the waiting time between the individual steps. The magnetic field regulation occurs via a Hall probe placed in the gap of the magnet. It produces a voltage which is dependent on the magnetic field perpendicular to the probe. The relationship is not linear and the voltage changes with temperature; however, this is easily compensated for by keeping the probe at a constant temperature slightly above room temperature and characterizing the nonlinearities so that the microprocessor in the controller can make the appropriate corrections. Regulation is accomplished by comparing the voltage from the Hall probe with the reference voltage given by the other part of the controller. When there is a difference between the two voltages, a correction voltage is sent to the magnet power supply which changes the amount of current flowing through the magnet windings and hence the magnetic field. Eventually the error voltage drops to zero and the field is “stable” or “locked”, this step occurs at each discrete step of a magnetic field scan.

In that specific EPR setup the magnetic field has a range of 0.001-0.6 Tesla (100-6000 Gauss). In most cases we set it around 3000 Gauss, Figures 38a, 39. The H.T. EPR which can cover a wide range of temperature from room temperature up to 1300K in Figure 38b.

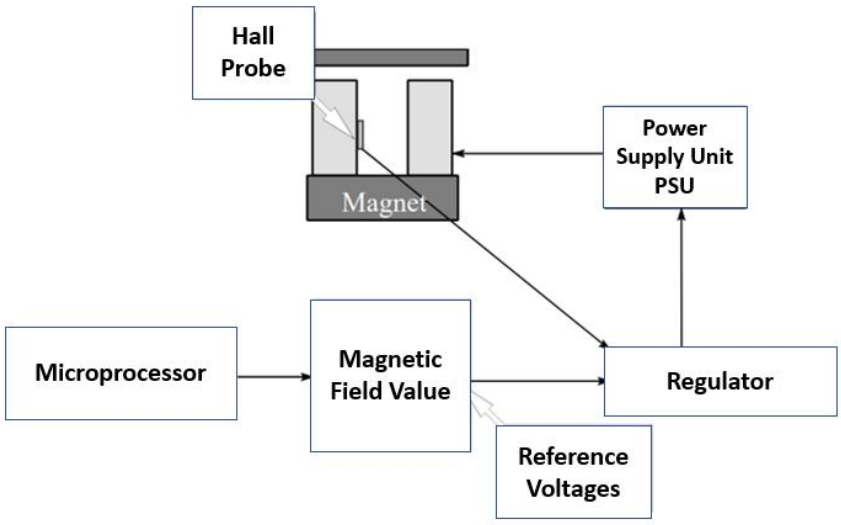

Figure 37: A block diagram of the field controller and associated components.

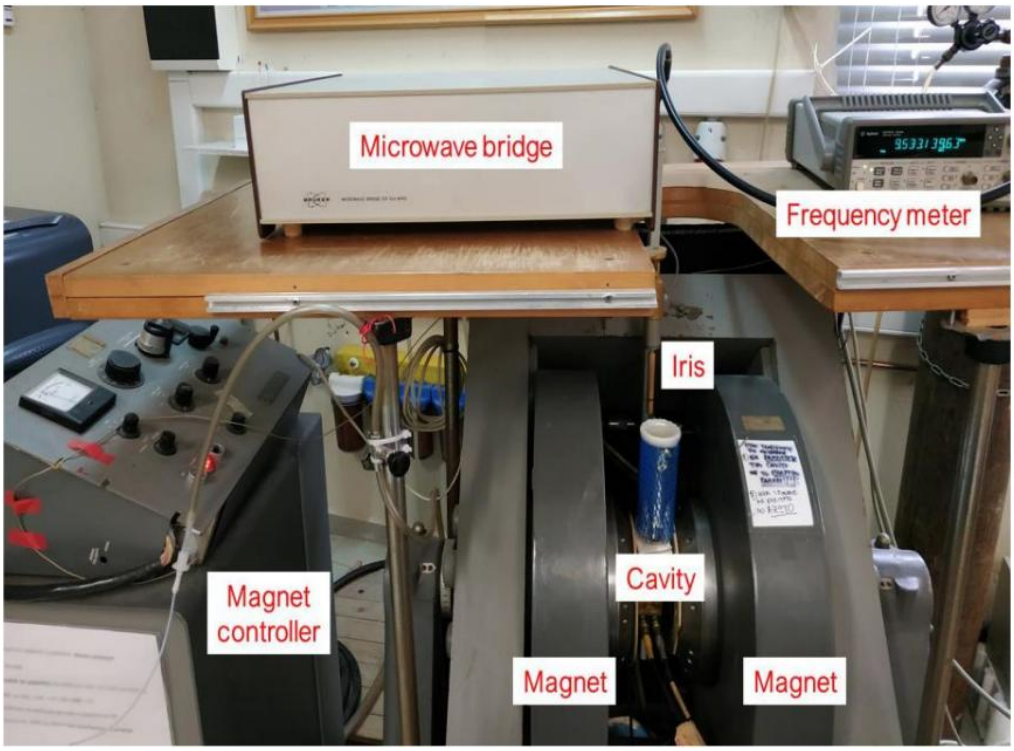

Figure 38a: The X-band EPR set-up. That magnet can apply a magnetic field of 8000 Gauss and uses a Hall probe to control the field. The Magnet controller controls the current that it passes to the electromagnet in order to achieve the magnetic field that we set. The Microwave bridge and the frequency controller-meter to produce and detect the microwaves as we explained. In that picture a Perpendicular Cavity is demonstrated with its iris motor to find the peak of the amplitude of the microwaves.

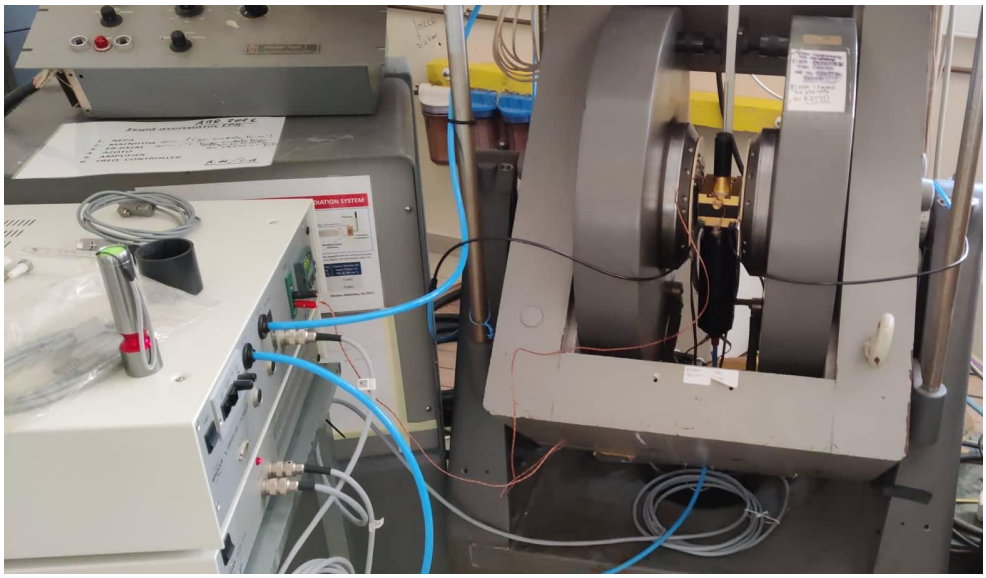

Figure 38b: The X-band EPR set-up. That magnet can apply a magnetic field of 8000 Gauss and uses a Hall probe to control the field. In that picture the H.T. Cavity is demonstrated.

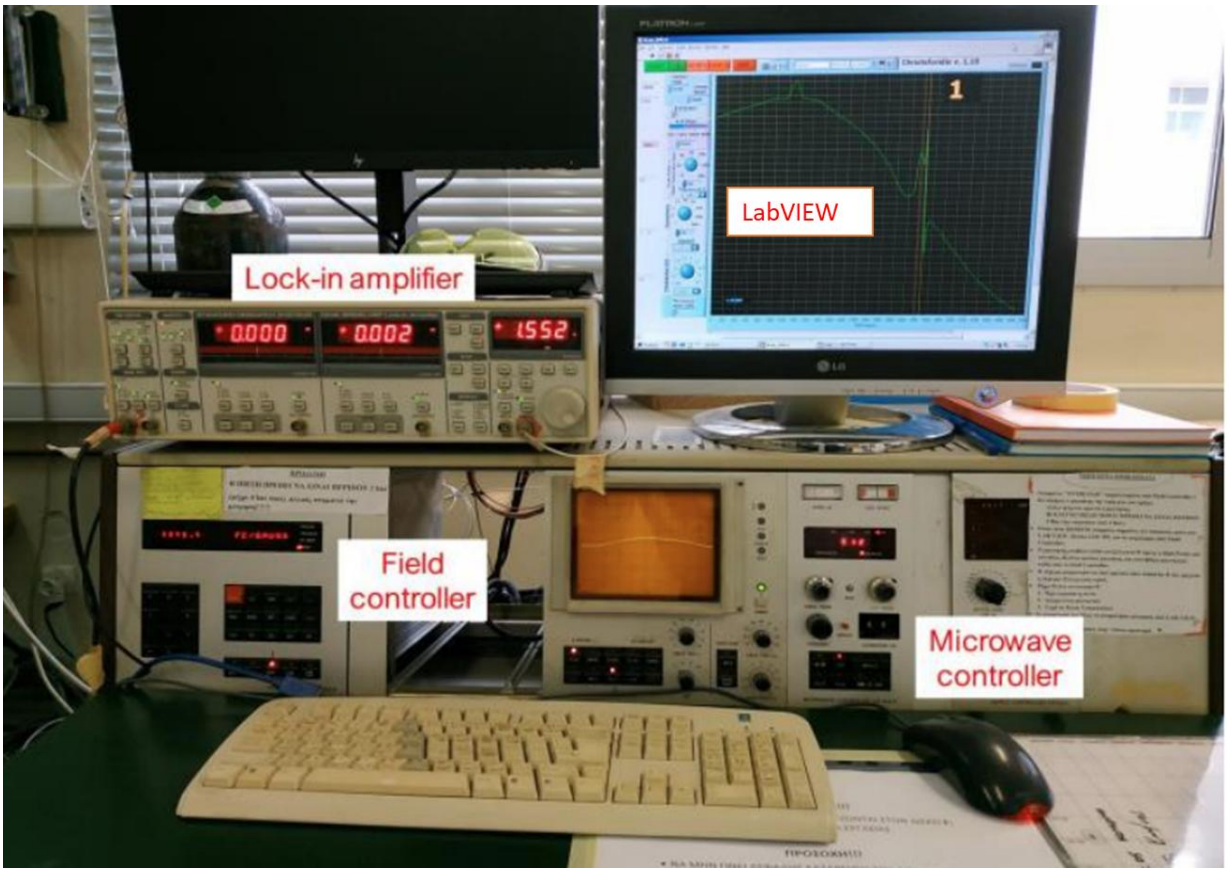

Figure 39: Here we present the lock-in amplifier, the field controller and the microwave controller to control the iris and the power of the microwaves.

3.4 The Signal Channel

EPR spectroscopy is a technique known as phase sensitive detection to enhance the sensitivity of the spectrometer. The advantages include less noise from the detection diode and the elimination of baseline instabilities due to the drift in DC electronics. A further advantage is that it encodes the EPR signals to make it distinguishable from sources of noise or interferences. The signal channel, a unit which fits in the spectrometer console, contains the required electronics for the phase sensitive detection.

The detection scheme works as follows. The magnetic field strength which the sample sees is modulated (varied) sinusoidally at the modulation frequency. If there is an EPR signal, the field modulation quickly sweeps through part of the signal and the microwaves reflected from the cavity are amplitude modulated at the same frequency. For an EPR signal which is approximately linear over an interval as wide as the modulation amplitude, the EPR signal is transformed into a sine wave with an amplitude proportional to the slope of the signal.
The signal channel (more commonly known as a lock-in amplifier or phase sensitive detector) produces a DC signal proportional to the amplitude of the modulated EPR signal. It compares the modulated signal with a reference signal having the same frequency as the field modulation and it is only sensitive to signals which have the same frequency and phase as the field modulation. Any signals which do not fulfill these requirements (i.e., noise and electrical interference) are suppressed. To further improve the sensitivity, a time constant is used to filter out more of the noise.
Phase sensitive detection with magnetic field modulation can increase our sensitivity by several orders of magnitude; however, we must be careful in choosing the appropriate modulation amplitude, frequency, and time constant, Figure 40. All three variables can distort our EPR signals and make interpretation of our results difficult.

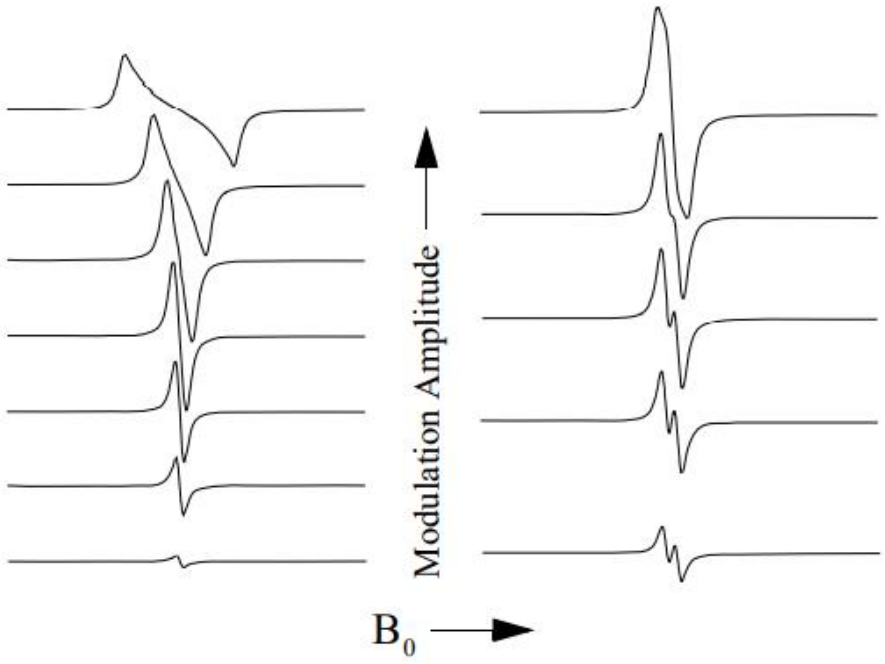

Figure 40: Signal distortions due to excessive field modulation.

For samples with very narrow or closely spaced EPR signals, (~ 50 milligauss. This usually only happens for organic radicals in dilute solutions.) we can get a broadening of the signals if our modulation frequency is too high as shown in Figure 41. The broadening is a consequence of the Heisenberg uncertainty principle.

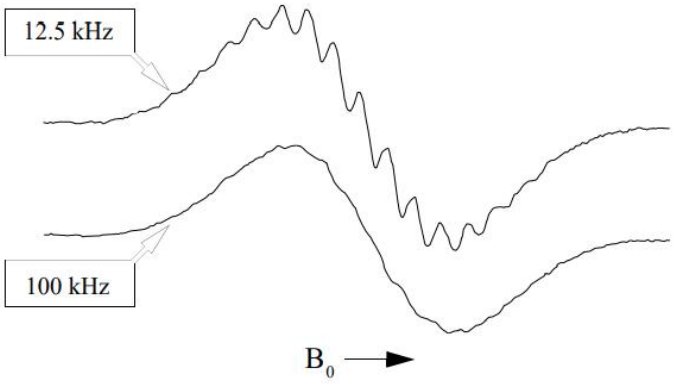

Figure 41: Loss of resolution due to high modulation frequency.

All those individual components of the spectrometer if they work together, they will produce a spectrum as shown in Figure 42.

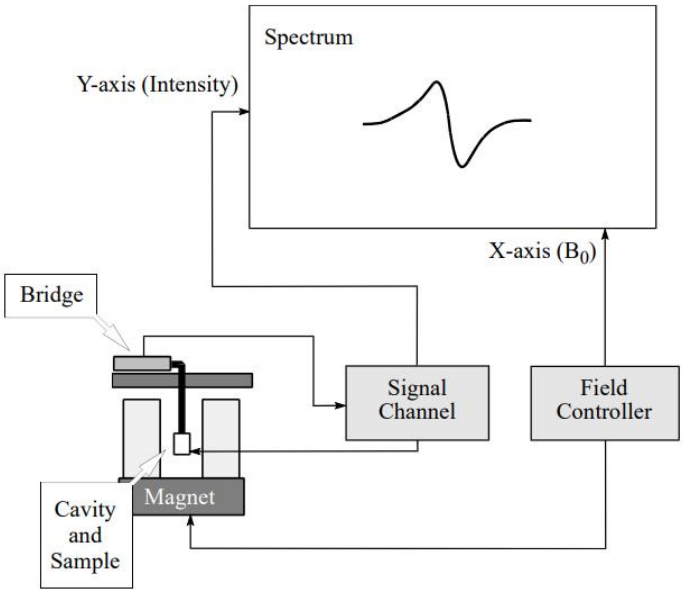

Figure 42: Block diagram of an EPR spectrometer.

3.5 Data Acquisition (DAQ)

Data acquisition (DAQ) is the process of sampling signals that measure real-world physical phenomena (temperature, voltage, current, strain and pressure, shock and vibration, distance and displacement, rpm, angle, discrete events, weight) and converting them into a digital form that can be manipulated by a computer and software. The signals are converted from the analog domain to the digital domain and then recorded to a digital medium such as ROM, flash media, or hard disk drives. Hence the primary purpose of a data acquisition system is to acquire and store the data. But they are also intended to provide real-time and post-recording visualization and analysis of the data. More data acquisition systems can merge and provide a tightly connected and synchronized with a real-time control system.

The modern digital data acquisition systems consist of four essential components that form the entire measurement chain of physics phenomena:

- Sensors
- Signal Conditioning
- Analog to Digital Converter (ADC)

- Computer with DAQ software for signal logging and analysis

Typical data acquisition system has multiple channels of signal conditioning circuitry which provide the interface between external sensors and the ADC subsystem. Because physical phenomena exist in the analog domain, i.e., the physical world that we live in, they must be first measured there and then converted to the digital domain.

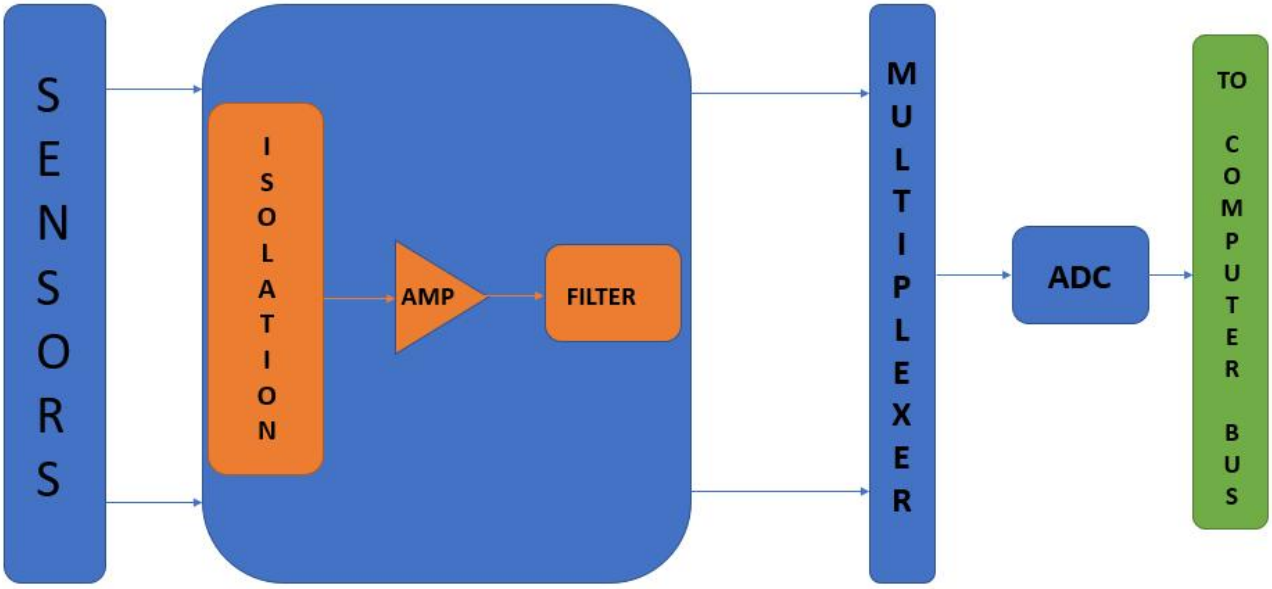

Figure 43: A complete scheme of an analog data acquisition system.

Some types of sensors for measuring different phenomena as mentioned earlier are for example:

- thermocouples, thermistors, Resistance Temperature Detectors (RTDs) and even infra-red temperature detectors for measuring Temperature.
- Load cells: for measuring weight and load,
- Accelerometers: measuring vibration and shock,
- Microphones: for measuring sound,
- Strain gauges: to measure strain on an object, e.g. measure force, pressure, tension, weight, etc.,
- Current transducers: for measuring AC or DC current,
- and countless more.

Depending on the type of sensor, its electrical output can be a voltage, current, resistance, or another electrical attribute that varies over time. The output of these analog sensors is typically connected to the input of a signal conditioner, which are taking the output from analog sensors and preparing them to be sampled digitally. The signal conditioning circuitry needs to linearize the output from the sensor as well as provide isolation (galvanic isolation), and amplification to bring the very small voltage up to a nominal level for digitizing.

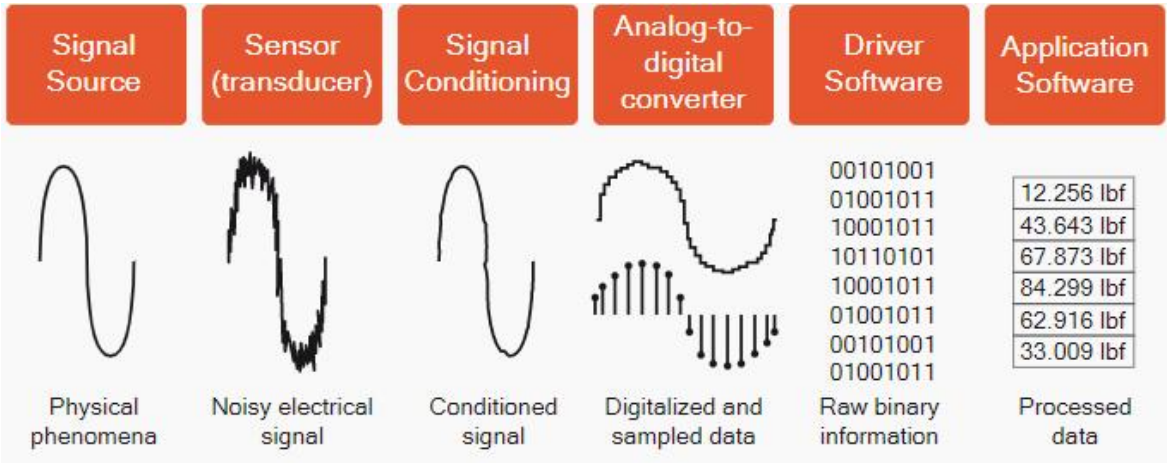

Figure 44: From analog signal source to digitalized data ready for processing by computer and software.

Isolation is especially important with respect to the analog input signals that we want to measure. So many of these signals exist at relatively low levels, and external electrical potentials can influence the signal greatly, resulting in wrong readings. Imagine the output of a thermocouple, which is just a few thousands of a volt, and how easily it could be overwhelmed with electrical interference. Electrical interference or noise can also take the form of AC signals created by other electrical components in the signal path or in the environment around the test. This is especially important with measuring systems because most signals exist at relatively low levels, and external electrical potentials can influence the signal quality greatly, resulting in wrong readings. Interfering potentials can be both AC and DC in nature. Some problems and "noise" are so called as common mode voltages (CMV) which are unwanted signals that get into the measurement chain, usually from the cable connecting a sensor to the measuring system. Depending on their amplitude, they can range from being a "minor annoyance" to completely obscuring the real signal and destroying the measurement. The most basic approach to eliminate those noises is to use a

differential amplifier, which has two inputs: a positive one and a negative one. The amplifier measures only the difference between the two inputs.

Electrical noise riding along on our sensor cable should be present on both lines - the signal positive line and the ground (or signal negative) line. The differential amplifier will reject the signals common to both lines, and only the signal will be passed through, as shown in the figure 45 below:

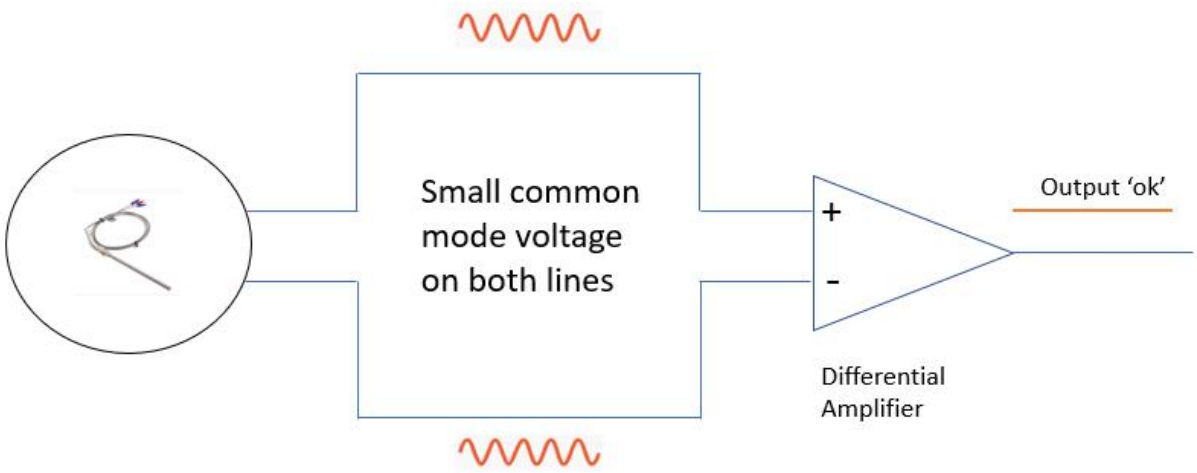

Figure 45: A differential amplifier successfully eliminates common-mode voltages within its CMV input range.

When the CMV present on the signal lines exceeds the differential amplifier's maximum CMV input range, it will "clip." The result is a distorted, unusable output signal, in these cases, we need an additional layer of protection against CMV and electrical noise in general which is the isolation. An isolated amplifier's inputs "float" above the common-mode voltage. They are designed with an isolation barrier with a breakdown voltage greater than 1000 V. This allows it to reject very high CMV noise and eliminate ground loops as show in Figure 45. Isolated amplifiers create this isolation barrier by using tiny transformers to decouple ("float") the input from the output, or by small optocouplers, or by capacitive coupling. The last two methods typically provide the best bandwidth performance. Sometimes called "noise," a ground loop is caused by inadvertently

referencing electrical equipment to more than one path to the ground - any difference of potential at these grounding points can induce a current loop, which can lead to distortions on the signal. If the amplitude of these distortions is high enough, it can ruin the measurement.

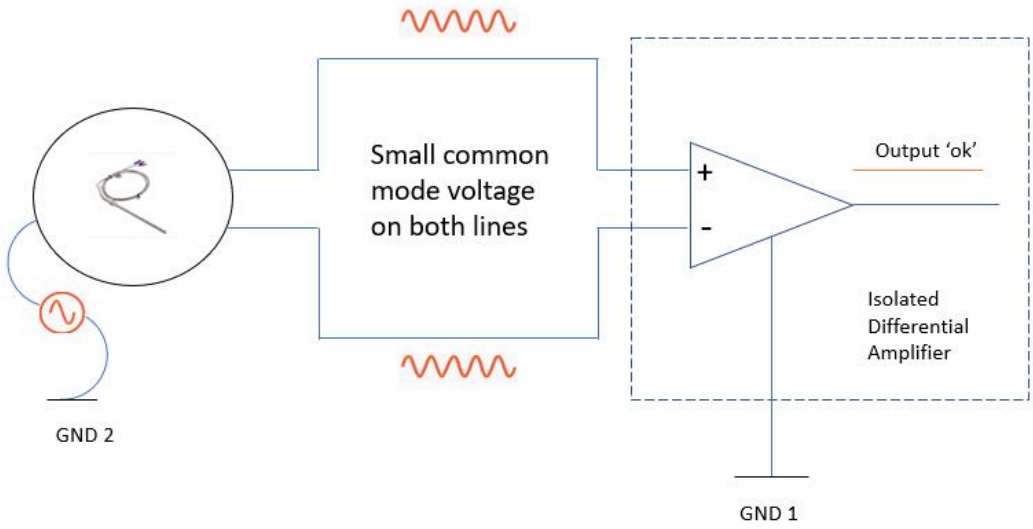

Figure 46: An isolated differential amplifier rejects even very high common-voltage mode.

Ground loops can also come from the instrument itself, via its own power supply. Keeping in mind that our measuring system is plugged into power, which has a ground reference. It is critical, therefore, to decouple this reference from the signal handling components of the instrument to ensure that ground loops cannot be created within the instrument.

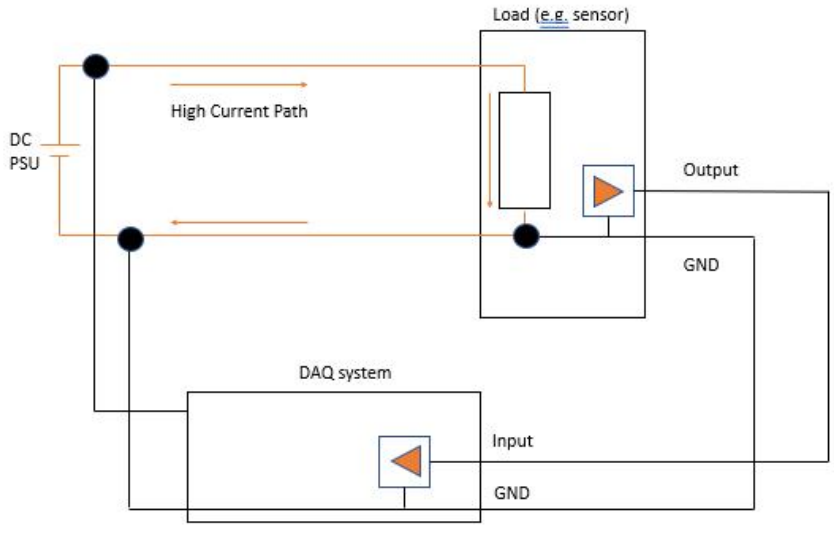

Figure 47: Power supply induced ground looping.

There are several approaches for creating an isolation barrier between a signal source and the rest of the system:

1. Optical isolation is one of the most popular and effective methods of isolating a signal from the rest of the system and the outside world. An electrical signal is input to an LED, which transmits it across a dielectric isolation barrier to a photodiode, which converts it back to an electrical signal. By converting an electrical signal to light and then back to electricity, it is completely decoupled from the outside world. Light is not susceptible to electromagnetic (EMI) or radio frequency (RFI) interference, inherent benefits of this approach. However, optocouplers are not as fast as light itself - they are limited by the LED's switching speed. They are generally slower than inductive or capacitive isolators. In addition, the intensity of the LED light will degrade over time, requiring recalibration or replacement.
2. In inductive coupling isolation, an electrical insulation barrier is placed between the windings, so that the only signals that pass from the first winding to the second are those that have been magnetically induced - and there is no direct contact across the barrier. Inductive couplers have very high bandwidth and are extremely reliable, but they can be affected by nearby magnetic fields.
3. Capacitive isolators couple a signal across an isolation barrier, usually made from silicon dioxide. They cannot pass DC signals, which makes them very adept at blocking common-mode signals. The signal is converted to digital and then replicated on the other side of the barrier using capacitive coupling. Unlike inductive isolation, capacitive isolation is not susceptible to magnetic interference. High data rates and long-life operation are hallmarks of these isolators. Capacitive isolators are available with different ratings to provide the right level of safety against failure and possible short circuits.

By isolating the system, we avoid electrical interference from the equipment itself but more generally every signal that we want to measure can be affected by electrical interference or noise. This has a variety of causes, including ambient electromagnetic fields which can be induced into high gain signal lines, or simple voltage potentials that exist between the sensor or measuring system and the object under test. Therefore, the best signal conditioning systems provide selectable filtering to remove these interferences and making better measurements. Filters can be

defined by how many poles they have. The more poles, the steeper the roll-off they can perform on the signal. This roll-off or slope simply means how many decibels of the signal can be rolled off per octave. The specification of the filter in question will typically give the maximum roll-off in dB/Q. Here filters will be expressed in terms of the band that they operate, to the following types:

- **Low-pass filter**: this filter reduces or "rolls off" starting at a given frequency and those above it.
- **High-pass filter**: does the opposite and allows frequencies to pass which are above a given frequency.
- **Band-pass and band-reject filters**: either pass or stop (reject) frequencies between two given values.

All those filters can be achieved by different types of filters like those which are presented in Table 3 depending on their purpose.

Filter Type	Roll-off Steepness	Ripple or Distortion	Other factors
Butterworth	Good	No ripple, but square waves cause distortion (hysteresis)	Moderate phase distortion
Chebyshev	Steeper	Ripples in the pass band	Poor transient response
Bessel	Good	No ringing or overshoot from non-sinus waveforms	Increased phase delay
Elliptic	Steepest	Ripples in the pass band	Non-linear phase response

Table 3: Filter types with trade-offs among them.

As described earlier another very important part is the conversion from analog to digital using an ADC, which will convert this signal to a series of high-speed digital values so that it can be displayed and stored by the data acquisition system. There are a variety of ADC types, including both multiplexed and single converter per channel. In a multiplexed ADC system, a single analog-to-digital converter is used to convert multiple signals from analog to digital domain. This is done by multiplexing the analog signals one at a time into the ADC. There are plenty ADC types from 8-bit to 32-bit ADCs with 16-bit ADCs to be the most common considered the bare minimum resolution for signals in general. The rate at which the signals are converted is called the sample rate. Certain applications, such as most temperature measurements, do not require a high rate since the measurands do not change very rapidly. However, AC voltages and currents, shock, vibration, and many other measurands require sample rates in the tens or hundreds of thousands of samples per second or more. Once converted to digital, our signals (aka measurands) are processed by the computer subsystem in several ways. First and foremost, they can be displayed to the test operator on the system's screen for visual inspection and review.

In this set up we need to read different data such as temperature, the changes in magnetic field, AC voltages which need to be measured all the time in real time and the amplitude. Because it's a very fast process, it needs very powerful hardware and, in that case, we used a DAQ from National Instruments PCIe-6351 (Figure 48) which can deliver up to 8 analog and digital inputs and outputs through the DMA channels. It also has external digital triggers which are workable through any protocol and have software-selectable polarity for many signals. The external digital triggers have analog inputs and outputs. These inputs and outputs enable the device to direct and break the triggers. It can also be used as a sample clock time-based and a sample clock. That DAQ device has four 32-bit counters/timers for event counting and PWM. These are also included for frequency, encoder, and is applicable in test automation and control applications. It is connected to the instrument's computer through a PCI express x16 slot. The most important part about this DAQ device is that it can have as input 1.25MS/s and as output the value of 2.86MS/s.

Figure 48: Multifunctioning DAQ Device from National Instruments that was used in EPR.

3.6 THE LOCK-IN AMPLIFIER

Lock-in amplifiers are used to detect and measure very small AC signals – all the way down to nanovolts and accurate measurements can be made even when the small signal is obscured by noise sources many thousands of times larger. The Lock-in amplifiers use a technique known as phase-sensitive detection to single out the component of the signal at a specific reference frequency and phase. Noise signals even if they are larger which are other than the reference frequency are rejected and don't affect the measurement.

In general, the lock-in measurements require a frequency reference, typically an experiment is excited at a fixed frequency (from an oscillator or a function generator) and the lock-in detects the response from the experiment at the reference frequency that is the phase-sensitive detection

technique (PSD). If for example, we send from a function generator a square wave as a reference signal at a frequency equal to ω_{ref} as shown in Figure 49, if the sine output from the function generator is used to excite the experiment, the response might be the signal waveform shown below. The signal is $V_{sig}\sin(\omega_{ref}t + \theta_{sig})$ where V_{sig} is the signal amplitude. The lock-in amplifier generates its own sine wave with a lock-in reference $V_L\sin(\omega_L+\theta_{ref})$.

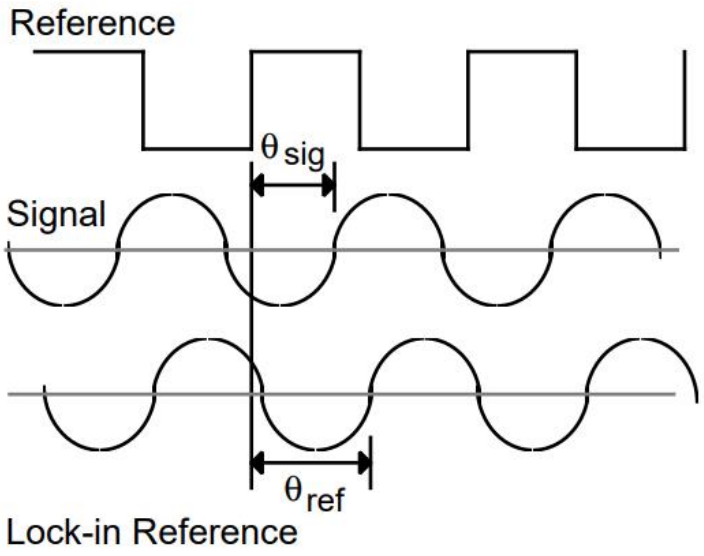

Figure 49: An example on how phase-sensitive detection technique that is used in lock-in amplifiers for signal detection based on a reference frequency and phase.

Then the lock-in amplifier amplifies the signal and then multiplies it by the lock-in reference using a phase-sensitive detector or multiplier. The output of the PSD is simply the product of two sine waves as shown in Equation 88.

Eq.88

as expected, the PSD output is two AC signals, one of the difference of the frequencies and one of the sum of the frequencies. If the PSD output is passed through a low pass filter, the AC signals are removed, in the general case that will give no signal, in the case though that ω_{ref} is equal to ω_L the

difference frequency component will be a DC signal and the output will be as shown in Equation 89.

Eq.89

In the case that the input is made up of signal plus noise. The PSD and low pass filter only detect signals whose frequencies are very close to the lock-in reference frequency. Noise signals at frequencies far from the reference are attenuated at the PSD output by the low pass filter (neither $\omega_{noise}-\omega_{ref}$ nor $\omega_{noise}+\omega_{ref}$ are close to DC). Noise at frequencies very close to the reference frequency will result in very low frequency AC outputs from the PSD ($|\omega_{noise}-\omega_{ref}|$ is small). Their attenuation depends upon the low pass filter bandwidth and roll-off. A narrower bandwidth will remove noise sources very close to the reference frequency, a wider bandwidth allows these signals to pass. The low pass filter bandwidth determines the bandwidth of detection. Only the signal at the reference frequency will result in a true DC output and be unaffected by the low pass filter. It's important that the lock-in reference needs to be phase-locked to the signal reference.

Lock-in amplifiers use a phase-locked-loop (PLL) to generate the reference signal. An external reference signal (in this case, the reference square wave) is provided to the lock-in. The PLL in the lock-in locks the internal reference oscillator to this external reference, resulting in a reference sine wave at ω_{ref} with a fixed phase shift of θ_{ref}. Since the PLL actively tracks the external reference, changes in the external reference frequency do not affect the measurement.

The internal oscillator of the lock-in amplifier can be used just like a function generator (with variable sine output and a TTL sync) which is always phase-locked to the reference oscillator.

In order to take a graph from those we need to determine the X-axis and the Y-axis as shown in Equations 90a and 90b below:

$$X=V_{sig}\cos\theta \quad \text{Eq.90a}$$

$$Y=V_{sig}\sin\theta \quad \text{Eq. 90b}$$

these two quantities represent the signal as a vector relative to the lock-in reference oscillator. X is called the 'in-phase' component and Y the 'quadrature' component. This is because when $\theta=0$, X

measures the signal while Y is zero. By computing the magnitude (R) of the signal vector as shown in Equation 91, the phase dependency is removed.

$$R=(X^2+Y^2)^{1/2}=V_{sig} \quad \text{Eq.91}$$

R measures the signal amplitude and does not depend upon the phase between the signal and lock-in reference. In addition, the phase θ between the signal and lock-in reference, can be measured according to the equation 92 as shown below.

$$\theta=\tan^{-1}(Y/X) \quad \text{Eq.92}$$

Fourier's theorem basically states that any input signal can be represented as the sum of many, many sine waves of differing amplitudes, frequencies and phases. This is generally considered as representing the signal in the "frequency domain". Normal oscilloscopes display the signal in the "time domain". Except in the case of clean sine waves, the time domain representation does not convey very much information about the various frequencies which make up the signal.

In that EPR set-up we used an SR-830 lock-in amplifier which multiplies the signal by a pure sine wave at the reference frequency. All components of the input signal are multiplied by the reference simultaneously. Mathematically speaking, sine waves of differing frequencies are orthogonal, i.e. the average of the product of two sine waves is zero unless the frequencies are exactly the same. In the SR830, the product of this multiplication yields a DC output signal proportional to the component of the signal whose frequency is exactly locked to the reference frequency. The low pass filter which follows the multiplier provides the averaging which removes the products of the reference with components at all other frequencies. Because it multiplies the signal with a pure sine wave, measures the single Fourier (sine) component of the signal at the reference frequency.
In the general case, the input consists of signal plus noise. Noise is represented as varying signals at all frequencies. The ideal lock-in only responds to noise at the reference frequency. Noise at other frequencies is removed by the low pass filter following the multiplier. This "bandwidth narrowing" is the primary advantage that a lock-in amplifier provides. Only inputs at frequencies at the

reference frequency result in an output. Lock-in amplifiers as a general rule display the input signal in Volts RMS. When the SR830 displays a magnitude of 1V (rms), the component of the input signal at the reference frequency is a sine wave with an amplitude of 1 Vrms or 2.8 V pk-pk.

The SR830 multiplies the signal with the reference sine waves digitally. The amplified signal is converted to digital form using a 16 bit A/D converter sampling at 256 kHz. The A/D converter is preceded by a 102 kHz anti-aliasing filter to prevent higher frequency inputs from aliasing below 102 kHz. The signal amplifier and filters will be discussed later. This input data stream is multiplied, a point at a time, with the computed reference sine waves described previously. Every 4 μs, the input signal is sampled and the result is multiplied by the two reference sine waves (90° apart). As we examined earlier Lock-in amplifiers have traditionally set the low pass filter bandwidth by setting the time constant. The time constant is simply $1/2\pi f$ where f is the -3 dB frequency of the filter. The low pass filters are simple 6 dB/oct roll off, RC type filters. A 1 second time constant referred to a filter whose -3 dB point occurred at 0.16 Hz and rolled off at 6 dB/oct beyond 0.16 Hz. Typically, there are two successive filters so that the overall filter can roll off at either 6 dB or 12 dB per octave. The time constant referred to the -3 dB point of each filter alone (not the combined filter). The notion of time constant arises from the fact that the actual output is supposed to be a DC signal. In fact, when there is noise at the input, there is noise on the output. By increasing the time constant, the output becomes more steady and easier to measure reliably. The tradeoff comes when real changes in the input signal take many time constants to be reflected at the output. This is because a single RC filter requires about 5-time constants to settle to its final value. The time constant reflects how slowly the output responds, and thus the degree of output smoothing.

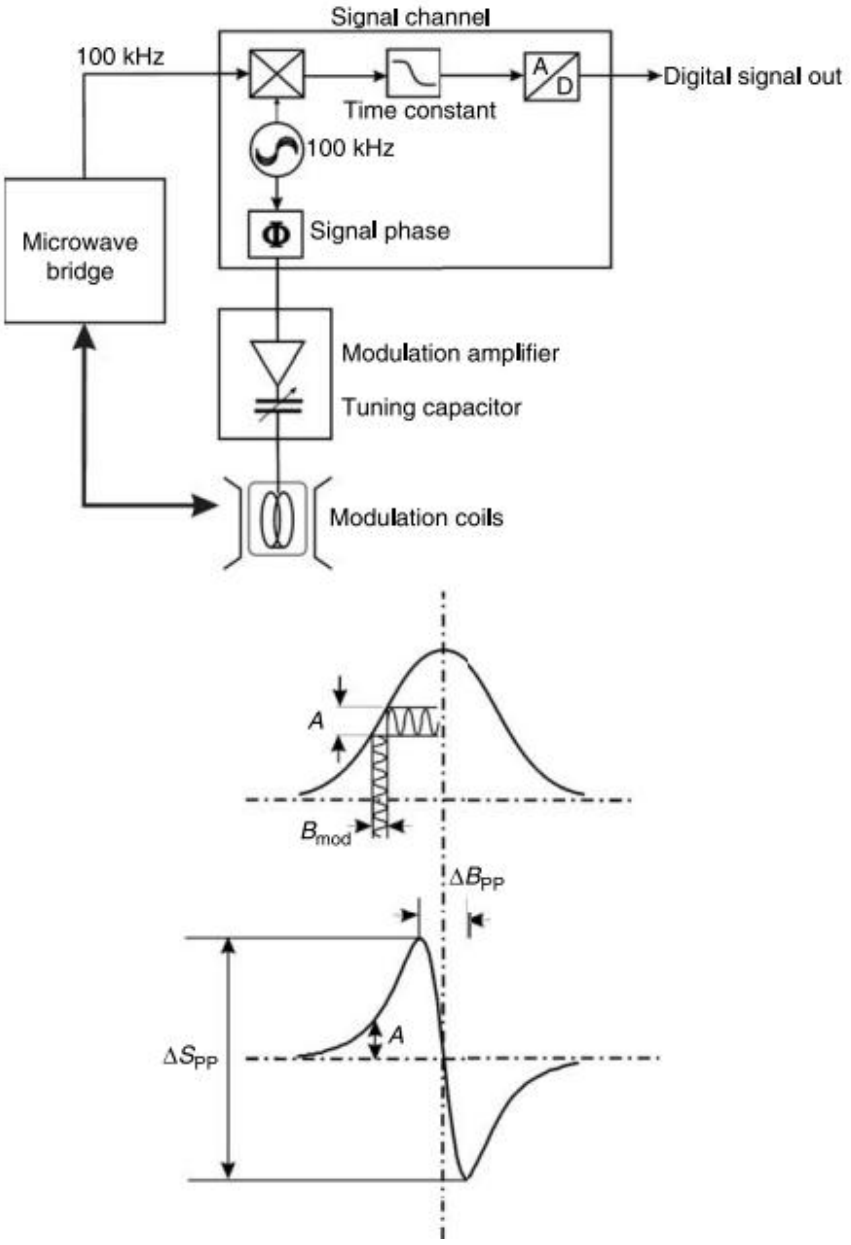

Figure 50: The magnetic field modulation scheme and derivative line shape. The derivative line is characterized by the peak–peak amplitude (ΔS_{pp}) and the peak–peak linewidth (ΔB_{pp}).

As noted, if the lock-in detection frequency is equal to the modulation frequency the first derivative of the absorption line is registered.

3.6.1 Random Noise in measurements

In every measurement there is random noise, but with good experimental design can reduce these noise sources and improve the measurement stability and accuracy. There are a variety of intrinsic noise sources which are present in all electronic signals. These sources are physical in origin.

- **Johnson noise**: Every resistor generates a noise voltage across its terminals due to thermal fluctuations in the electron density within the resistor itself. These fluctuations give rise to an open-circuit noise voltage as shown below (Equation 93)

$$V_{noise}(rms)=(4k\ TR\Delta f)^{1/2} \qquad \text{Eq.93}$$

  where k is Boltzmann's constant (1.38x10-^{23} J/°K), T is the temperature in °Kelvin (typically 300°K), R is the resistance in Ohms, and Δf is the bandwidth in Hz. Δf is the bandwidth of the measurement.
- **Shot noise**: Electric current has noise due to the finite nature of the charge carriers. There is always some nonuniformity in the electron flow which generates noise in the current. This noise is called shot noise. This can appear as voltage noise when current is passed through a resistor, or as noise in a current measurement. The shot noise or current noise is given by Equation 94 as below:

$$I_{noise}(rms) = (2qI\Delta f)^{1/2} \qquad \text{Eq.94}$$

  where q is the electron charge (1.6x10-19 Coulomb), I is the RMS AC current or DC current depending upon the circuit, and Δf is the bandwidth.
- **1/f noise:** Every 10Ω resistor, no matter what it is made of, has the same Johnson noise. However, there is excess noise in addition to Johnson noise which arises from fluctuations in resistance due to the current flowing through the resistor. For carbon composition resistors, this is typically 0.1 μV-3 μV of rms noise per Volt of applied across the resistor. Metal film and wire-wound resistors have about 10 times less noise. This noise has a 1/f spectrum and makes measurements at low frequencies more difficult. Other sources of 1/f noise include noise found in semiconductors.

All of these noise sources are incoherent. The total random noise is the square root of the sum of the squares of all the incoherent noise sources.

In addition to the intrinsic (random) noise sources discussed previously, there are a variety of external noise sources. Most of these noise sources are asynchronous, i.e. they are not related to the reference and do not occur at the reference frequency or its harmonics. These noise sources affect the measurement by increasing the required dynamic reserve or lengthening the time constant. Some noise sources, however, are related to the reference and, if picked up in the signal, will add or subtract from the actual signal and cause errors in the measurement. Typical sources of synchronous noise are ground loops between the experiment, detector and lock-in, and electronic pick up from the reference oscillator or experimental apparatus. There are several ways in which noise sources are coupled into the signal path.

The most common noise sources are:

- **Capacitive Coupling:** An AC voltage from a nearby piece of apparatus can couple to a detector via a stray capacitance. Although C_{stray} may be very small, the coupled noise may still be larger than a weak experimental signal. This is especially damaging if the coupled noise is synchronous (at the reference frequency). We can estimate the noise current caused by a stray capacitance by

$$i=C_{stray}\, dV/dt= \omega\, C_{stray}\, V_{noise} \qquad \text{Eq.95}$$

  where ω is 2π times the noise frequency, V_{noise} is the noise amplitude, and C_{stray} is the stray capacitance.

- **Inductive Coupling:** An AC current in a nearby piece of apparatus can couple to the experiment via a magnetic field. A changing current in a nearby circuit gives rise to a changing magnetic field which induces an emf (dØB/dt) in the loop connecting the detector to the experiment. This is like a transformer with the experiment-detector loop as the secondary winding.

- **Resistive coupling or ground loops:** Currents flowing through the ground connections can give rise to noise voltages. This is especially a problem with reference frequency ground currents. The experiment senses the detector signal plus the voltage due to the noise source's ground return current passing through the finite resistance of the ground between the experiment and the detector. The detector and the experiment are grounded at different places which, in this case, are at different potentials.

- **Microphonics:** Not all sources of noise are electrical in origin. Mechanical noise can be translated into electrical noise by microphonic effects. Physical changes in the experiment or cables (due to vibrations for example) can result in electrical noise over the entire frequency range of the lock-in. Mechanical vibrations in the cable translate into a capacitance that varies in time, typically at the vibration frequency. Since the cable is governed by Q=CV, taking the derivative, we have:

  Eq.96

  Mechanical vibrations in the cable which cause a dC/dt will give rise to a current in the cable. This current affects the detector and the measured signal.

- **Thermocouple effects:** The emf created by junctions between dissimilar metals can give rise to many microvolts of slowly varying potentials. This source of noise is typically at very low frequency since the temperature of the detector and experiment generally changes slowly. This effect is large on the scale of many detector outputs and can be a problem for low frequency measurements, especially in the mHz range.
-

3.7 DIGITAL CONTROL OF THE EPR SPECTROMETER

In this subchapter we will explain with the help of a flow diagram (Figure 51) the way that all those components are cooperating and connecting so the High Temperature EPR spectrum can be taken. Each one of the parameters are controlled digitally with the cooperation of some physical components.

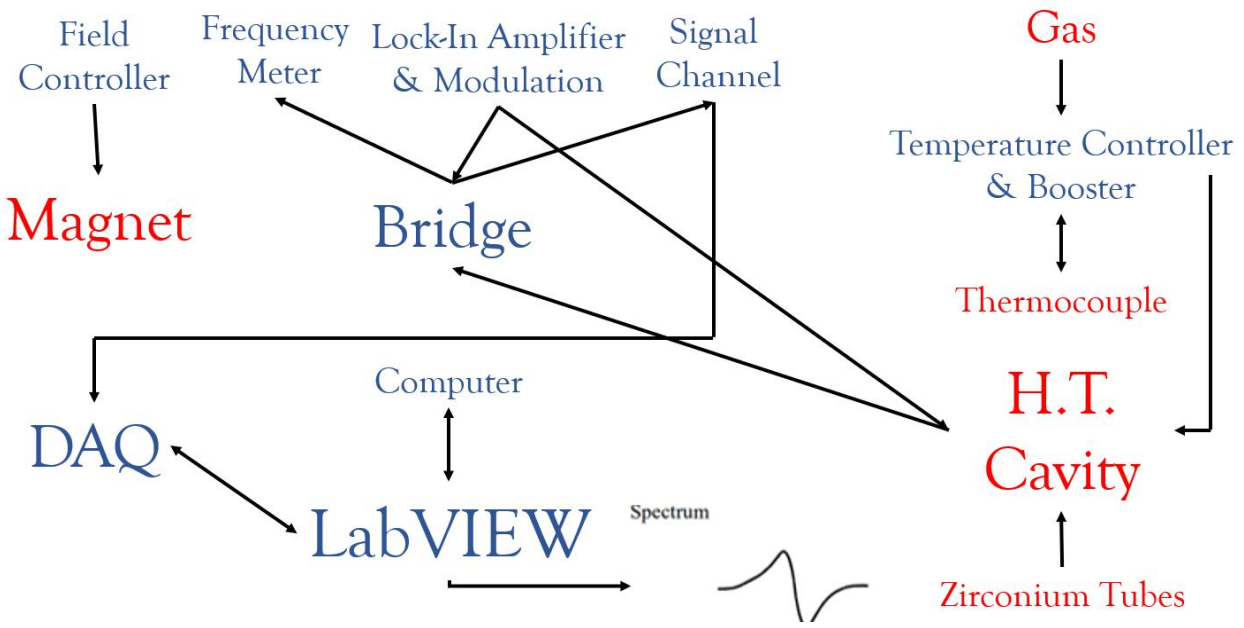

Figure 51: In this Figure we present a flow diagram on how each component physical or digital controlled is connected with each other to receive the spectrum. In that diagram the physical controlled parts are with red color coded and the digitally controlled are with blue.

Modern spectrometers are software controlled and contain multiple microprocessors to store calibration data and operate modules of the spectrometer under command from the main software program. The operator interacts with the spectrometer via the keyboard of a PC, with software that is vendor specific.

For all the reasons we mentioned the dependence of temperature in any material may be different. Its important that almost all components are digital-controlled and more especially all of them are controlled via LabView.

LabVIEW is a programmable environment made by National Instruments since 1991. It uses a logic model of programming which is able to allocate the problem into subprograms, the sub-Vis. In that way it splits the problem into smaller pieces and let the programmer to solve each one of

them more efficiently. The most important is that LabVIEW is an inherently concurrent language, so it is very easy to program multiple tasks that are performed in parallel via multithreading. Below we show in Figure 52a the LabView main VI, with all the parameters that we change to take a spectrum in H.T. EPR.

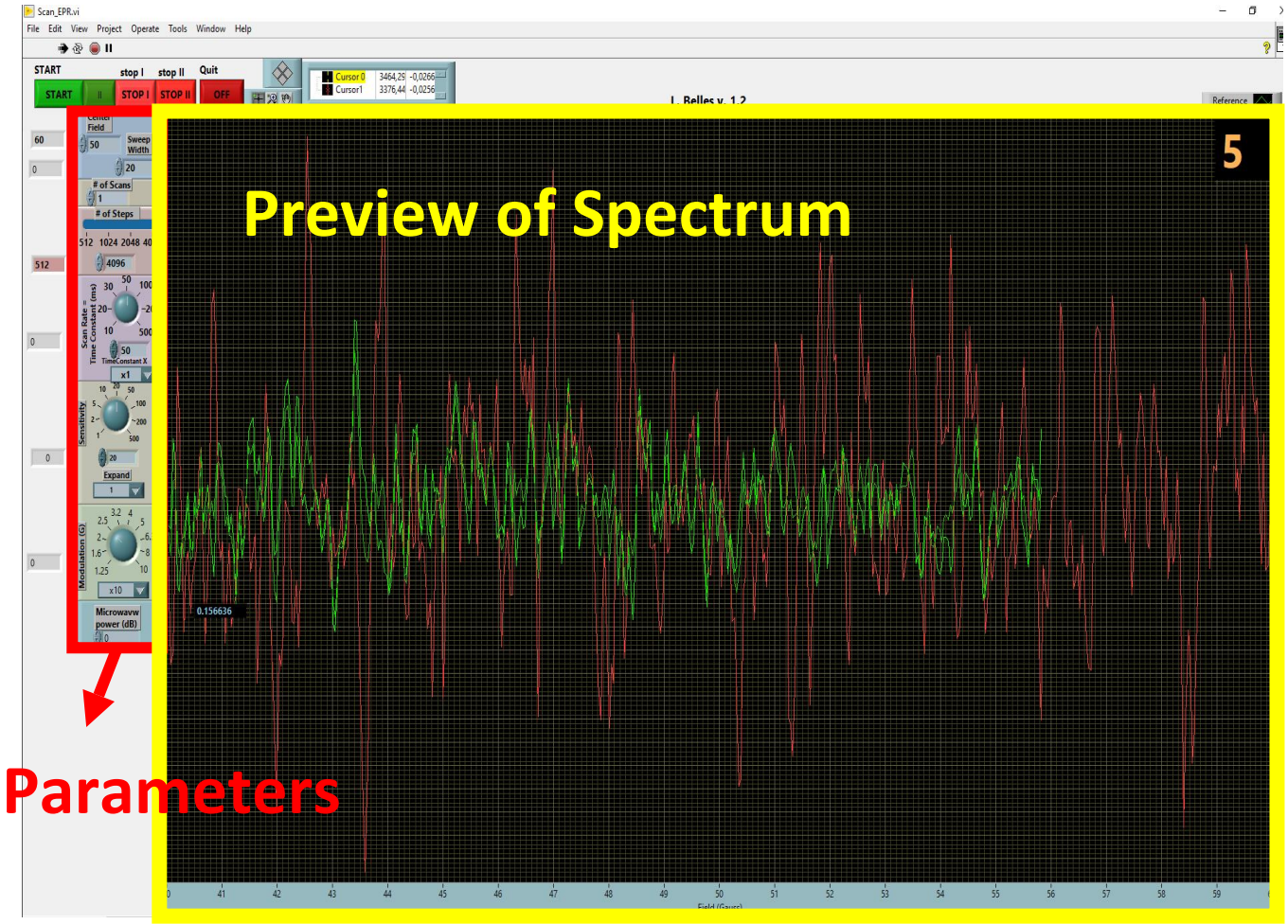

Figure 52a: In this Figure we show the main VI of LabView for the control of HT EPR spectrometer.

After the development of the Vi, it has been converted in an executable form (.exe) in order to run it with no loop-problems. In figure 52a we show the two basic windows, on the left in the red box we show where the parameter settings are imported by the user which is more detailed in Figure 52b and on the right side in the yellow box is the measured spectrum of the material.

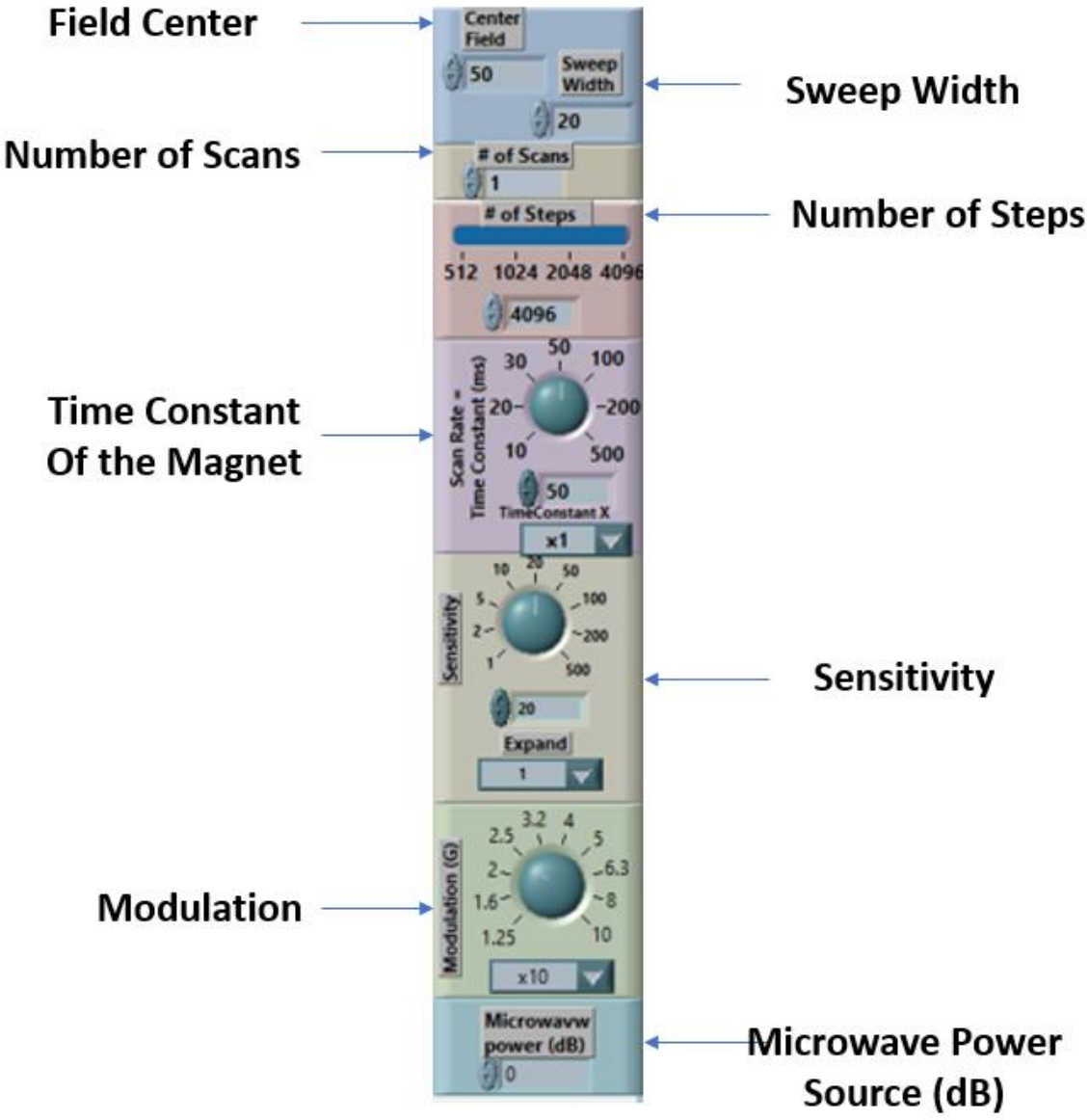

Figure 52b: here we show the panel of LabView or of the HT EPR.exe in which we add all the settings parameters that we control through it. In this figure also each value-field is explained.

Next we will analyze the block diagram of the EPR VI, in a detailed way in order to understand how the software works.

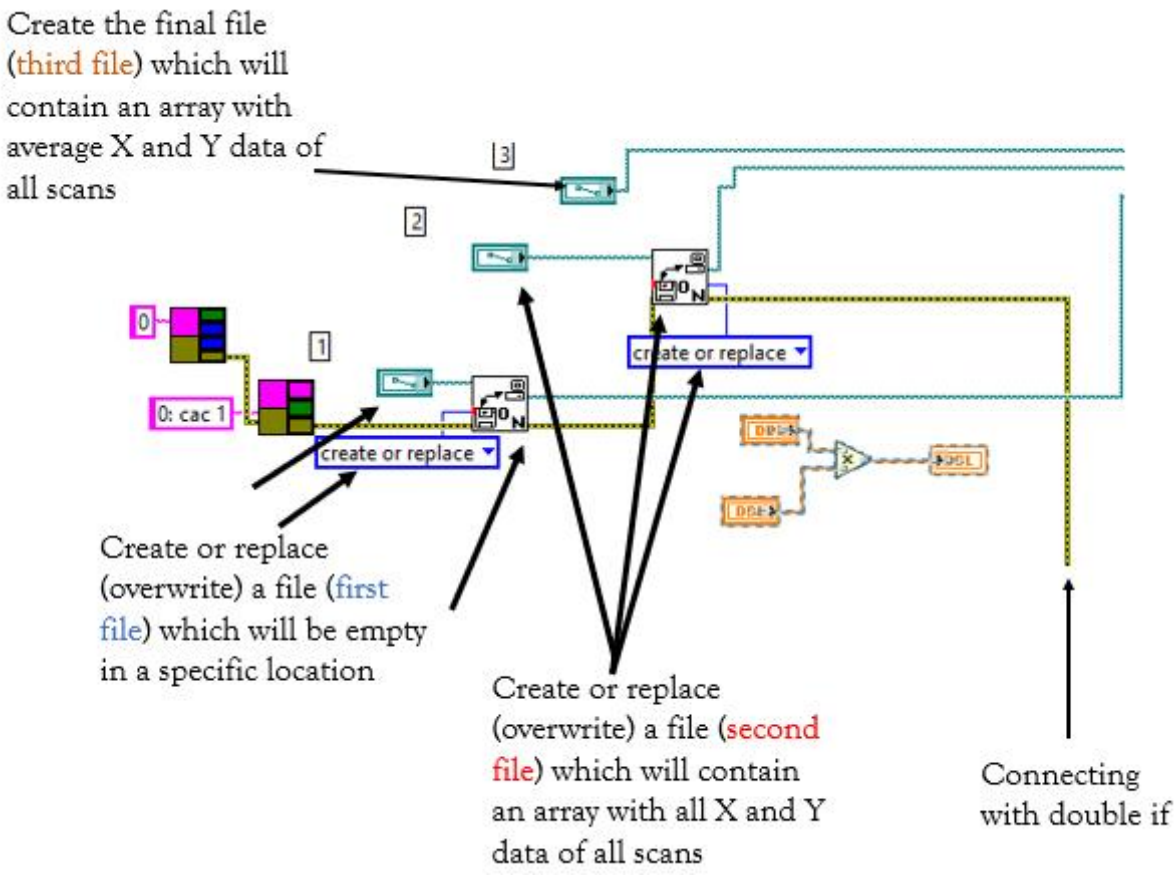

Figure 52c: We show in the LabView the creation of three different files. The first file will be an empty array which will be created or overwrite an existing one. The second file which will be created or overwrite an existing one, it will create an array of an equal size with the first array. So the second array will include the data of every scan, i.e. the X-values and the Y-values. The third and last file will have the average values of all Y values versus X values

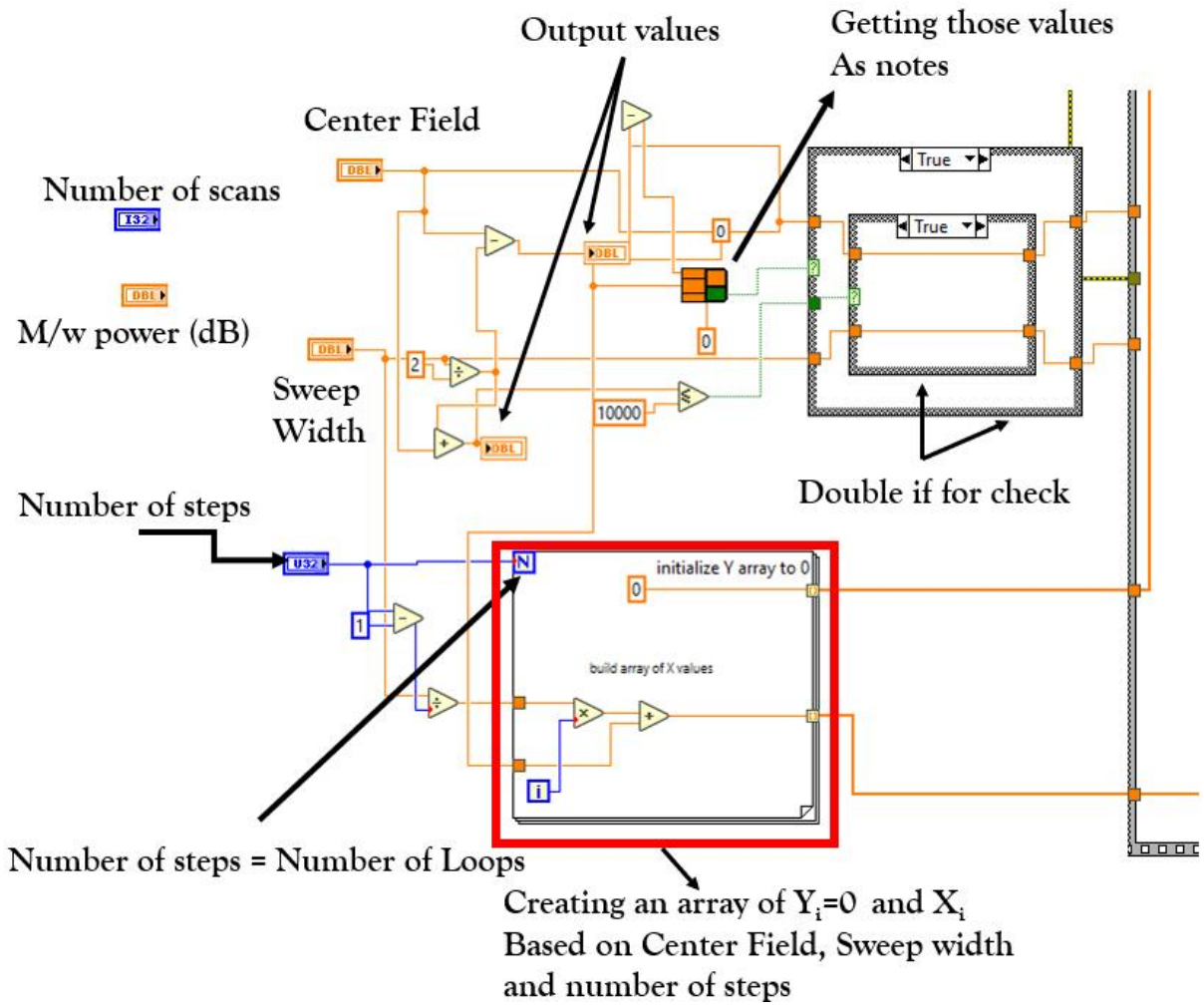

Figure 52d: We show LabView's Block diagram, the creation and the connections for each parameter. Here we present the center field, the sweep width (which is divided with two in order to go around the field center), also the results of each mathematical operation will appear in front panel, also the number of steps will divide the range of the field in to equal fields and create an array with the proper X-values but zero Y-values.

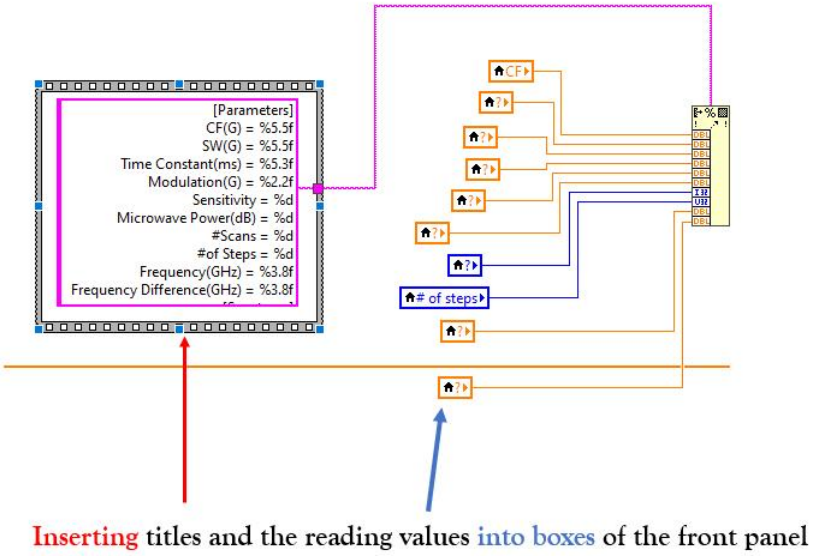

Figure 52e: In this figure the values of the parameters are taken from the GPIB and placed as values on the top of the data in the same file (output file).

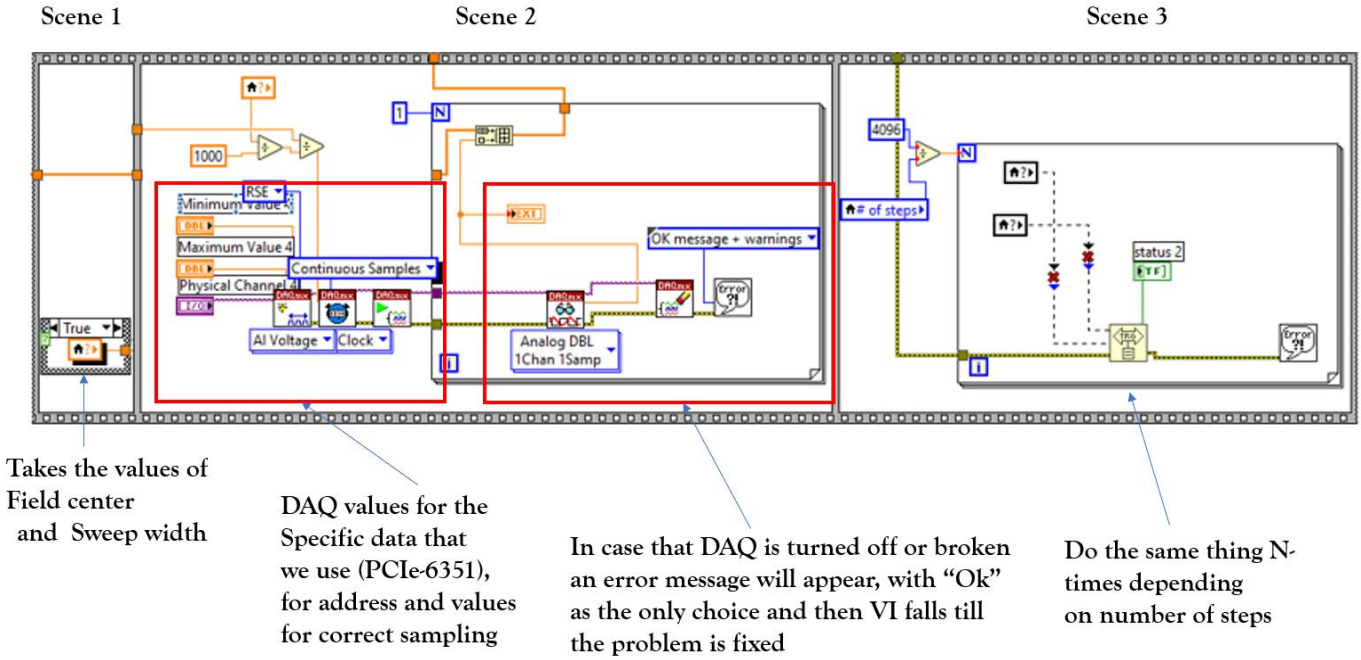

Figure 52f: Here in the block diagram we connect the values of the array of the previous figure, then the DAQ values (address and number of bytes to read), the case of an error at GPIB and at the third scene we send data to the GPIB, here we add a number which is connected to the GPIB bus address and then if something is wrong an error message will appear to the user.

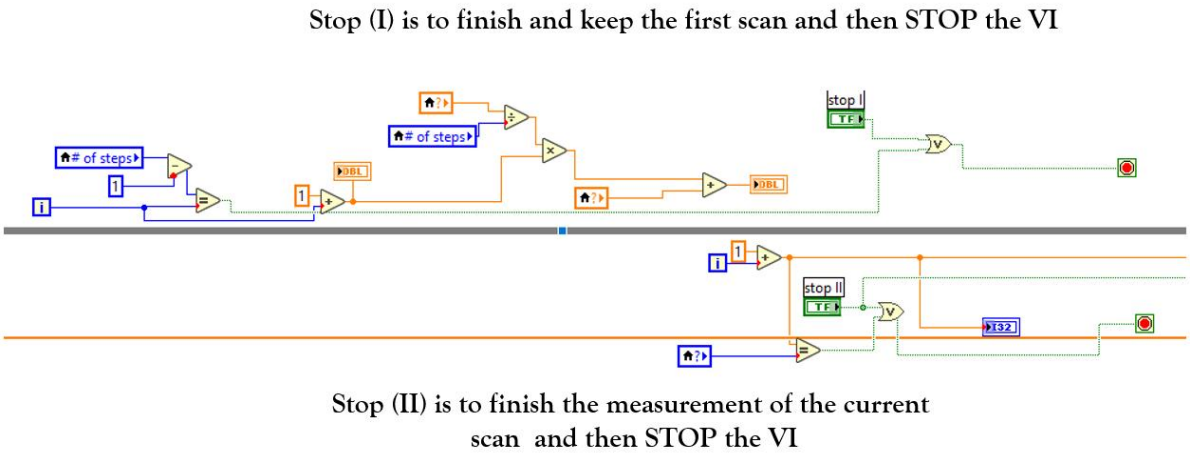

Figure 52g: In that part of the program of the block diagram we insert two buttons in the Front panel (STOP I) which will finish and keep the first scan and then stop the VI and (STOP II) is used to finish measurement after the current scan.

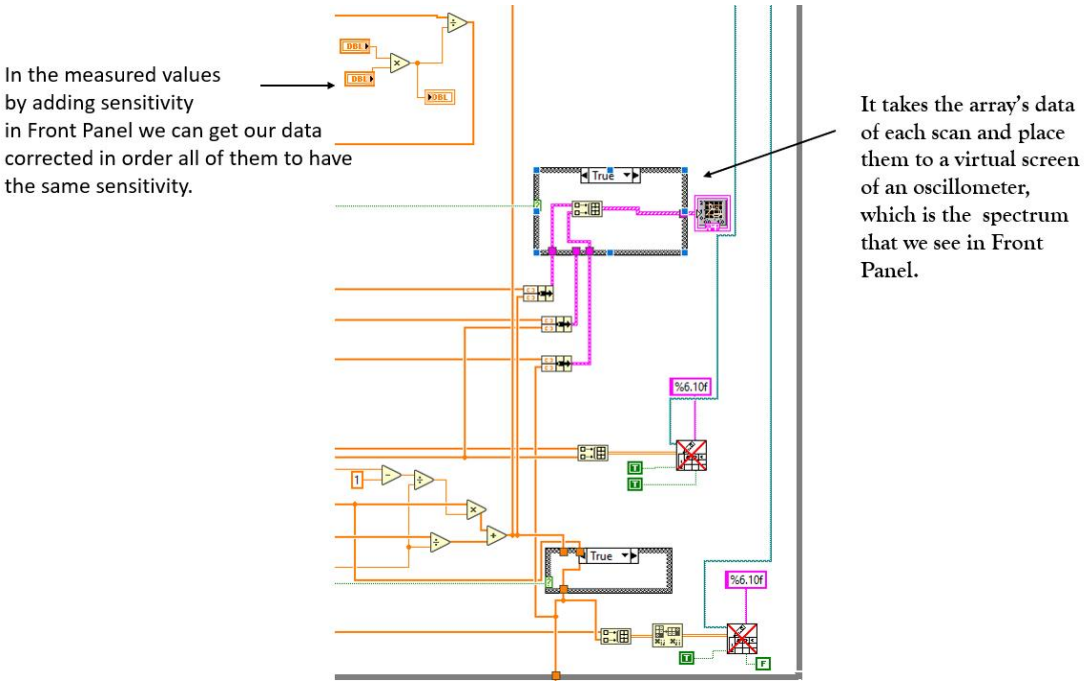

Figure 52h: In that part of the program of the block diagram we insert a knob in Front panel "Sensitivity" in which we choose the same sensitivity setting with the Lock-in Amplifier in order to get our data corrected, otherwise if we leave it at 1 we will get raw data. The measurement will eb correct but in the information file the sensitivity will be wrong. Also we add a virtual oscillator in order to see the spectrum after each scan finishes.

3.8 High Temperature EPR

The High Temperature EPR differs from the casual CW EPR to the cavity and the temperature at which we measure and take the EPR spectra. In this thesis we used an ER4114HT cavity. That cavity was chosen because it can be connected with any X-Band EPR as the one we have in the laboratory. This cavity is provided by Bruker with an upper temperature limit of 1273K (1000 ºC) that limit is defined by the quartz re-crystallization in long experimental runs. A tailor-made three wall high purity quartz glass dewar houses both the sample tube and the heater wire.
The forming gas is heated by the tungsten filament to achieve a maximum temperature of 1200 K. The temperature is measured with a thermocouple (type K: Cr-Al) close to the sample.
Also, the inner surfaces of the resonator have been coated with a material which is highly reflective for both infra-red and visible radiation. Due to the low thermal expansion coefficient of the cavity material, the frequency shift upon temperature change is kept at minimum. In addition, the cavity's end-plates and the sample chokes are water cooled. As in regular cavities the waveguide and the cavity space are purged with nitrogen gas and the matching proceeds via an iris screw.

3.9 High Temperature Equipment

The High Temperature EPR equipment is different than a common CW EPR Set-up. Of course, it is similar i.e. the high temperature EPR spectrometer set up needs a magnet with a magnetic field controller and a PSU to apply an external magnetic field, a microwave bridge and a frequency controller for produce and detect of the microwaves, a DAQ card for data acquisition, a GPIB card and shield which is a bus where every part is connected with each other and connected to the computer and of course the LabView VI which is the software to take measurements remotely and do all the mathematically work also with it we make the proper files to save all kind of data with all the parameters.
Therefore, at a High Temperature EPR spectrometer set-up the equipment that is needed is a High temperature Cavity (ER4114HT) which will be endurable to high temperatures and the specific one is associated with some zirconium tubes in which the sample will be placed. Also there is a

need of some thermocouples that will measure the temperature every moment and a high stability temperature controller (Eurotherm 2416) with self and adaptive tuning in order to control the temperature inside the cavity in cooperation with the thermocouple. Also, because of the cavity we will need some N_2 source for the inside resistor in order not to get damaged.

3.9.1 High Temperature Cavity – ER4114HT

This high temperature cavity which is shown in Figure 53a is a tailor-made three wall high purity quartz glass dewar houses both the sample tube and the heater wire. The inner surfaces of the resonator have been coated with a material which is highly reflective for both infra-red and visible radiation also, the cavity space and the waveguide are purged with nitrogen gas. A forming gas is inserted and heated by the tungsten filament, which is shown in Figure 53b, to achieve a maximum temperature of 1200 K. The forming gas is advised to be a mixture of 92% N_2 and 8% H_2, that gas is protecting the heater and the dewar, in order to keep the Q-value of the cavity high and to transfer the heat very fast. The upper temperature limit of 1273 K (1000 °C) is the limit which is defined by quartz re-crystallization in long experimental runs. Due to the low thermal expansion coefficient of the cavity material, the frequency shift upon temperature change is kept at minimum. In addition, the cavity end plates and the sample chokes are water cooled (with pressur e 1.0 up to $2.5*10^5$Pa).

(a)

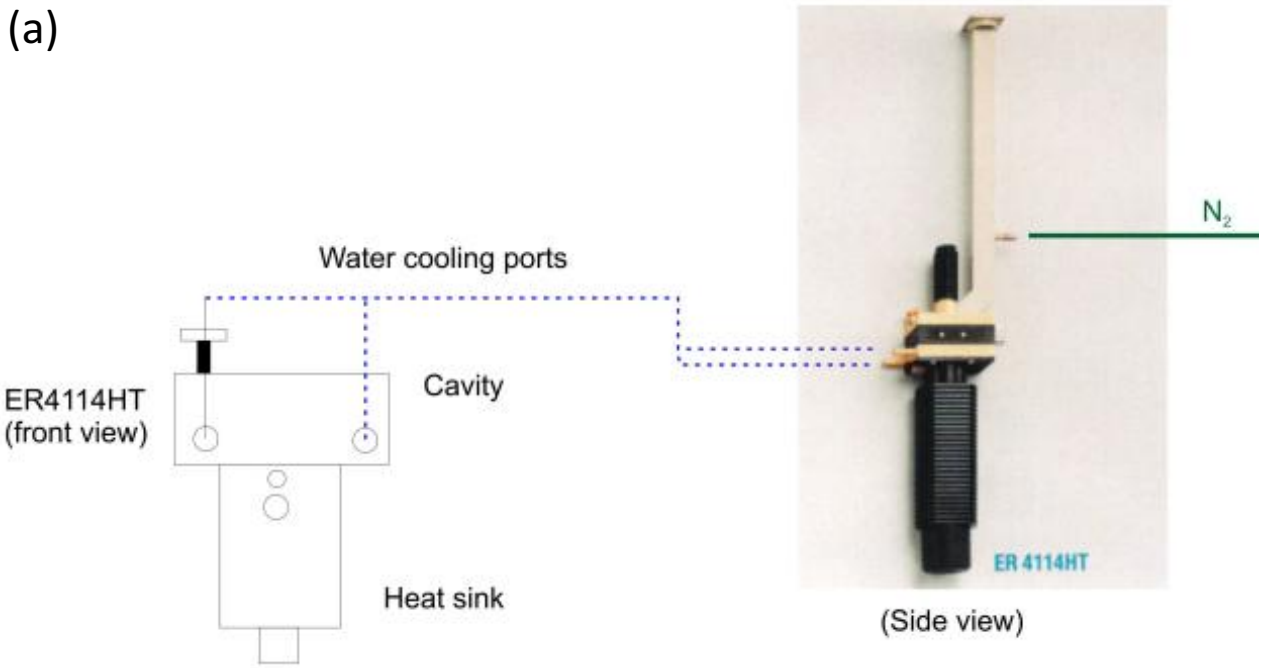
Water cooling ports
ER4114HT
(front view)
Cavity
Heat sink
N_2
ER 4114HT
(Side view)

(b)

(c)

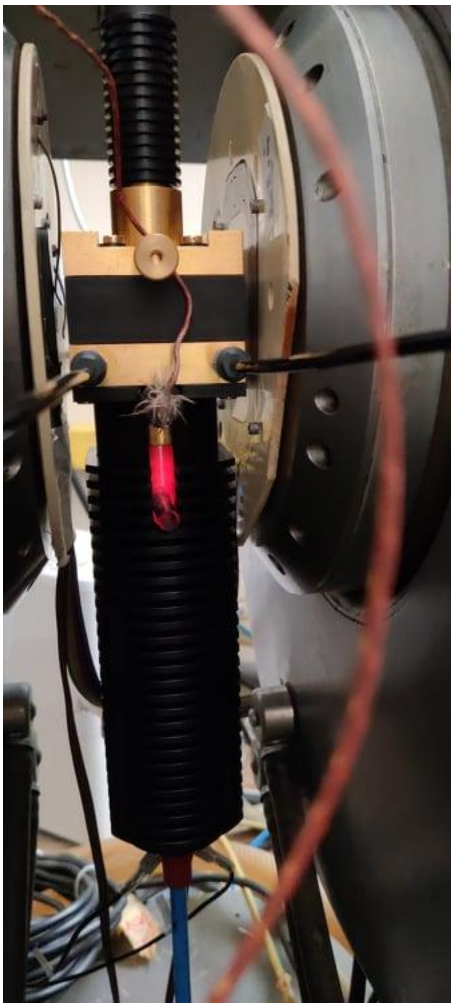

Figure 53: (a) High Temperature EPR cavity (ER4114HT made by Bruker on the top) and (b) the tungsten filament (bottom) which is used as a resistor to heat the sample with the help of a forming gas from the bottom side under the cavity. (c) The H.T. cavity while warming with low N_2 flow.

3.9.2 High Temperature Controller – BVT3000

Except for the High Temperature Cavity an important part of the High Temperature EPR equipment is the temperature controller which is referred as BVT 3000, which is shown in Figure 54, and can be also computer controlled via an RS-232 cable and LabView. The gas flow and the heater power are controlled; a digital display reads the actual as well as the desired temperature, which can also be set via front panel operation. In order to transfer so much current through the

tungsten filament a power booster, also known as BVTB3500 will be needed to heat up the heating wire in the dewar to such a temperature that the sample can reach the max. specified temperature of 1200 K. The booster is controlled via the temperature controller.

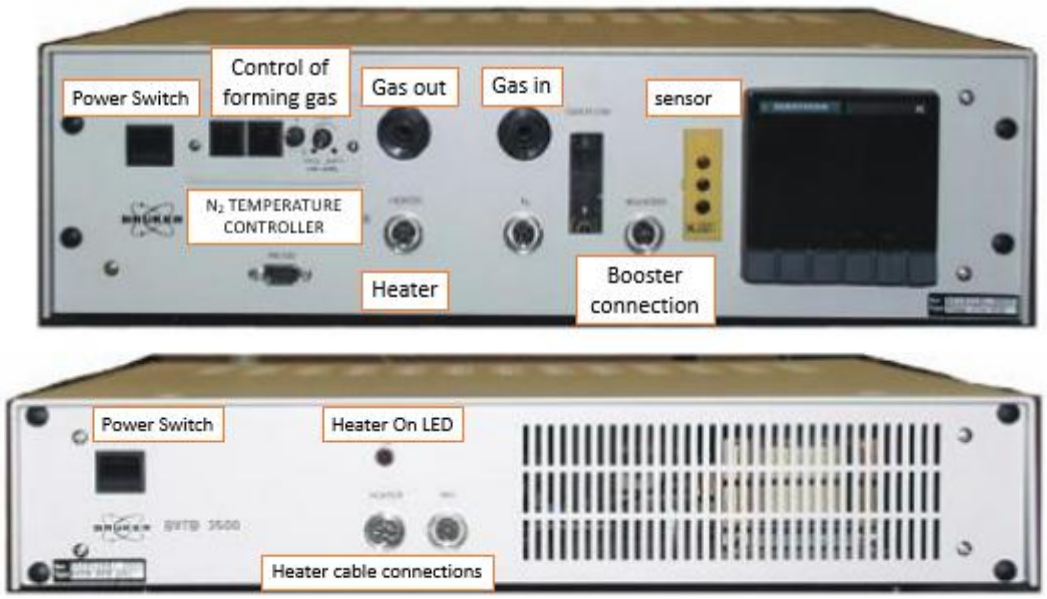

Figure 54: On top the BVT 3000 temperature controller is presented and on the bottom the power booster BVTB3500 to provide the necessary electrical power to heat the tungsten filament. The booster is controlled via the temperature controller.

Heater cable of the BVTB3500 needs to connect the heater output of the power booster to the electrical contacts of the heater wiring of the ER41114HT cavity. In more detailed way a schematic is following in Figure 55 to show the connections between the temperature controller, the power booster, the computer, the cavity.

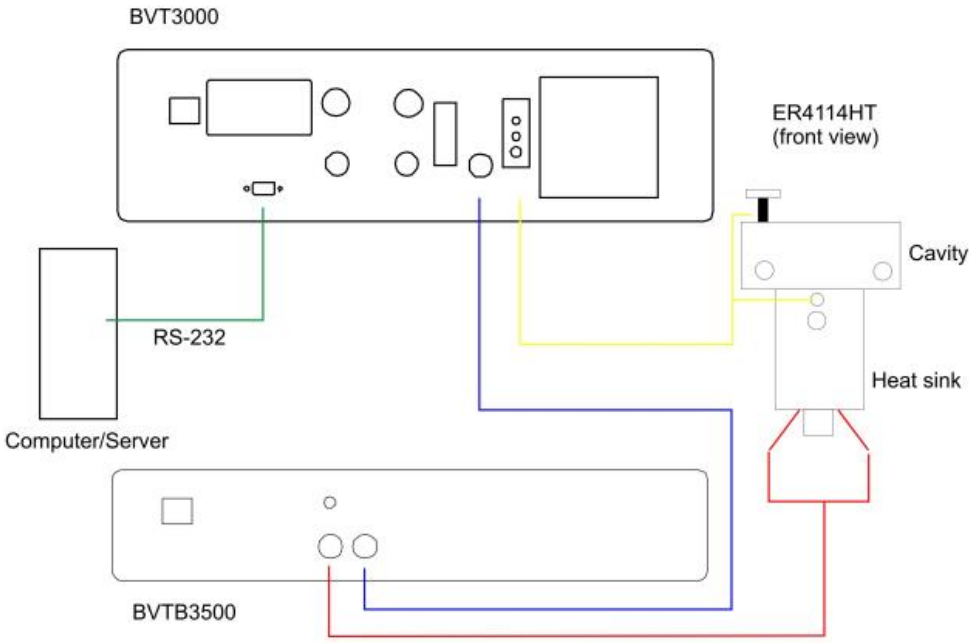

Figure 55: Connections between the BVT3000, the BVTB3500 and the High Temperature Cavity for the HT EPR spectrometer set-up. The green cable is the RS-232 which connects to the same plug to the computer in order to control the unit remotely. The blue cable is connecting the power booster to the temperature controller. The red cable is connecting the power booster with the resistor in order to send the proper amount of electrical energy to the module and finally to the tungsten filament. At the end the yellow cable is the sensor cable with the thermocouple that we made in order to read the temperature to the controller. Its important that the negative bias of the thermocouple to be attached to the cavity's metal in order to be colder than the positive bias and so the thermocouple to work properly, otherwise false information will be provided as reading temperature.

Also, for the forming gas the followed schematic in Figure 56 is showing the connections for the forming gas.

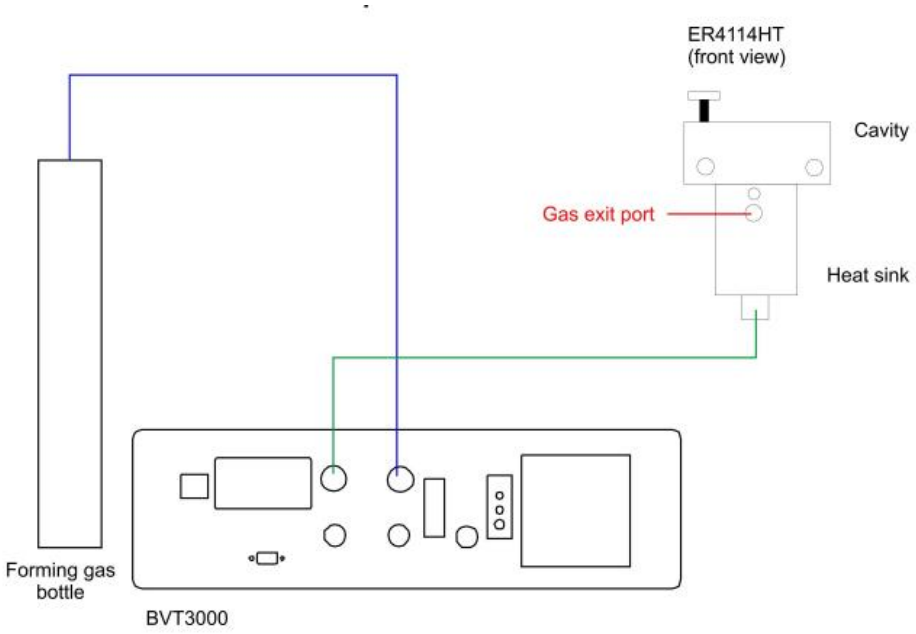

Figure 56: The connections between the forming gas that in our case will be 99.999% N_2 with the temperature controller. The blue cable is the Gas in that is going from the N_2 bottle to the Gas in socket through a tube and then with the green cable through a tube it will go to the bottom of the structure under the cavity. Afterwards the forming gas will flow and get the hotter gas out through the gas exit port.

The gas flow rate can be controlled though the temperature controller BVT 3000 and the Gas Flow Rate of the forming gas may be set to the two smallest possible rates: 135 l/h and/or 270 l/h.

3.9.3 Thermocouple Type K

Many sensors use materials that have variable electrical resistivity depending on the temperature or by mechanical pressure or even by humidity. The electrical resistivity of a metal-material depends on the temperature as shown in Equation 97:

Eq.97

Where ρ is the electrical resistivity of the conductor at the temperature T, ρ_o is the electrical resistivity of the conductor at a specific-reference temperature T_o and a is the thermal factor of the material of the electrical resistance. On the Table 4 we present some metals with their thermal factor and electrical resistivity.

Metal	**ρ (μΩ/cm) at 20 ^oC**	**a ($^oC^{-1}$)**
Gold (Au)	*2.44*	*0.0040*
Silver (Ag)	*1.59*	*0.0041*
Copper (Cu)	*1.72*	*0.0043*
Platinum (Pt)	*0.0966*	*0.00393*
Tungsten (W)	*5.60*	*0.0048*
Nickel (Ni)	*7.80*	*0.0068*
Chromel (90% Ni & 10% Cr)	*0.00706*	*0.00032*
Alumel (95% Ni & 2% Al & 2% Mn & 1% Si)	*0.00294*	*0.00239*

Table 4: Values of electrical resistivity ρ and thermal factor α for common metals used in thermocouples and sensors.

The metal's sensitivity at temperature's changes is given by the change of electrical resistivity versus the temperature and its different for every material. A thermocouple is an electrical devise consisting of two dissimilar electrical conductors forming an electrical junction. Due to Seebeck effect which is the electromotive force (emf) that is developed across two points of an electrically conducting material when there is a temperature difference between them (thermoelectric emf). The ratio between the emf and temperature difference is the Seebeck coefficient. One thermocouple as the one we used in our system measures the potential difference between a hot and cold end for two dissimilar materials. This potential difference is proportional to the temperature between cold and hot ends. This happens because electron energy levels shifted differently in the different metals, creating a potential difference between the junctions which in turn created an electrical current through the wires, and therefore a magnetic field around the wires.

The local current density is given by:

Eq.98

where V is the local voltage, σ is the local conductivity,

and

Eq.99

In that thesis we constructed some type K thermocouples with the use of Alumel and Chromel as shown in Figure 57.

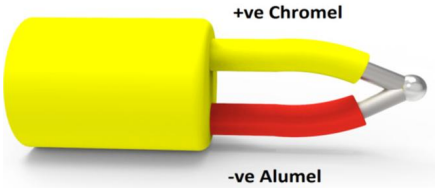

Figure 57: A schematic of a type-K thermocouple as the one we constructed for that EPR set-up.

Type K (Chromel-Alumel) is the most common general-purpose thermocouple with a sensitivity of approximately 41μV/^{o}C [61]. That thermocouple is inexpensive and a wide variety of probes are available to cover all the temperature range, in which the High Temperature EPR experiments will be conducted, more specifically the thermocouple can detect from -200^{o}C to +1350^{o}C. They operate very well in oxidizing atmospheres. If, however, a mostly reducing atmosphere (such as hydrogen with a small amount of oxygen) encounters the wires, the chromium in the Chromel alloy oxidizes. This reduces the emf output, and the thermocouple reads low. This phenomenon is known as *green rot*, due to the color of the affected alloy. Although not always distinctively green, the Chromel wire will develop a mottled silvery skin and become magnetic. An easy way to check for this problem is to see whether the two wires are magnetic (normally, Chromel is non-magnetic). In this set up we will not examinate the green rot phenomenon because all the heating system is at the same atmosphere so the error at the temperatures is constant.

CHPATER 4 RESULTS

4.1 Thermocouple Calibration

All thermocouples and also those, that we constructed from alumel and chromel need calibration temperature versus voltage so, after we constructed a second thermocouple, with the same materials and properties and we placed it inside the zirconium tube where the sample will be, to have two temperature reads. The first read is about measuring the temperature below the cavity and the sample and to heat the system when the T_{set} (the set temperature) is higher than the T_{read} temperature, to set the resistance off when the set temperature is almost equal to the read Temperature and then to keep it in equilibrium. The second thermocouple in the sample tube reads the temperature there, as shown in Figure 58 its almost equal with the other temperature read. Therefore, two calibrations achieved one to measure the difference between the set temperature and one measurement of potential with a potentiometer versus temperature as shown in Figure 59.

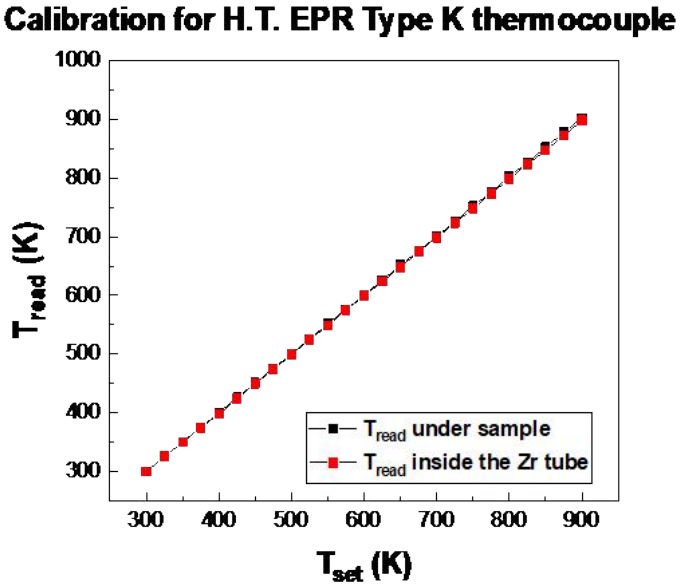

Figure 58: In this Figure we present the reading temperature of two type K thermocouples that we made. The first one is placed under the sample and the second inside the Zirconium tube. We notice a very small difference in reading temperature with an error peak of 8K.

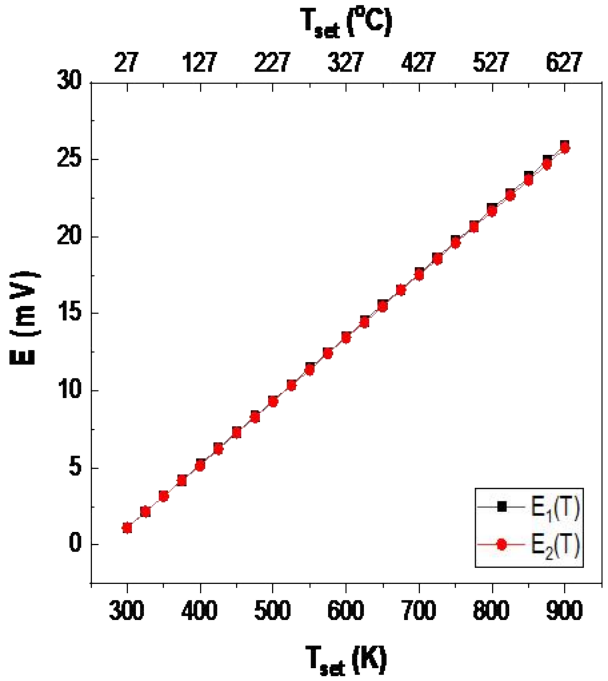

Figure 59: In this Figure we present the calibration of two type K thermocouples that we made. The first one is placed under the sample and the second inside the Zirconium tube. We measured the voltage difference with an oscilloscope notice a very small difference in reading voltage, which explains also the small difference in temperature reading.

4.2 N_2 Flow Calibration

As mentioned earlier the forming gas must go through the quartz glass and the tungsten filament. However, to have the control of the N_2 flow gas before it enters the chamber, it has to pass through the temperature control unit BVT 3000. The control of the N_2 flow can be done by a knob on the temperature controller who changes the flow and has 10 options with the first to be the limit of 135 lt/h. So in order to calibrate the flow of the forming gas we had to connect it with a flow controller before the Gas In port to the temperature controller and ensure to give enough pressure in order to achieve higher flows and in order to know how much forming gas to send to the chamber to transfer heat. In that calibration, as shown in Figure 60 we will set the knob at a lower highest limit because we don't want to go to extreme temperatures for the materials that we interest and also for safety reasons.

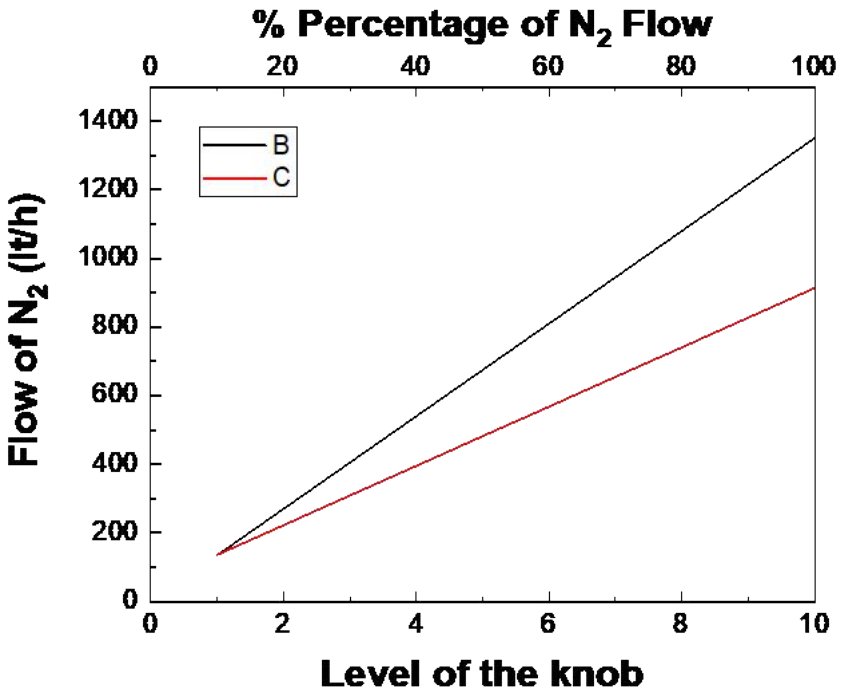

Figure 60: N_2 flow calibration that enters the temperature controller BVT 3000, then flows to the chamber where the tungsten filament (resistor) is heating and then transfers the heat to the zirconium tube where the sample is in, at the preferred temperature. In that calibration we set the knob at a lower highest limit because we don't want to go to extreme temperatures for the materials that we interest and also for safety reasons.

The exact values of the forming gas flows are presented on the Table 5 below.

KNOB LEVEL	CALIBRATED FLOWS OF N_2
1	136
2	222.4
3	308.8
4	395.2
5	481.6
6	568
7	654.4
8	740.8
9	827.2

10	913.6

Table 5: The values that match to the level of the knob after the calibration of the forming gas with the use of a flow meter.

4.2.1 Purging N_2 Flow Calibration

The setup was calibrated with a purge N_2 flow of 100 ml/min. While we increased the temperature the microwave resonance seemed to be minimized and after a specific temperature the resonance was destroyed as shown in the next set of screenshots at different temperatures.

Starting from the Room Temperature (300K) as shown in Figure 61:

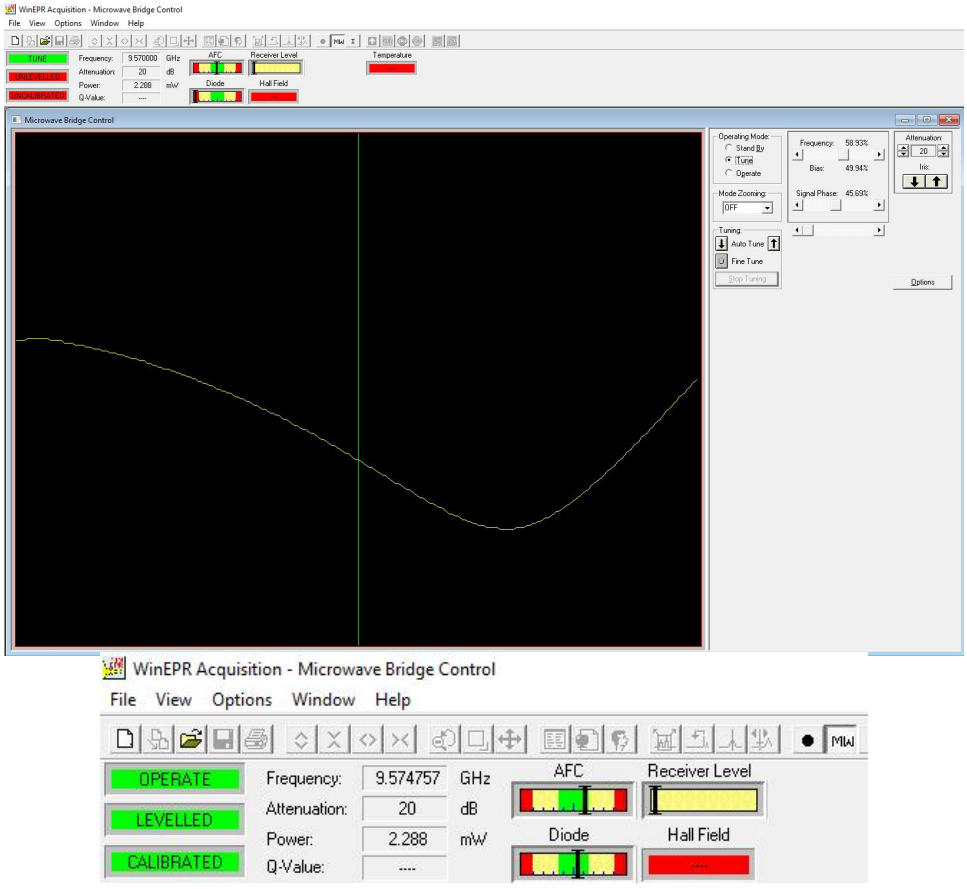

Figure 61: (a) Tuning the resonance of the microwaves and (b) levelling and calibrating the Diode of the detector of the microwave bridge at 300K.

We increased the temperature by an amount of 20K to check the stability of tuning and operating functions as shown in Figures 62:

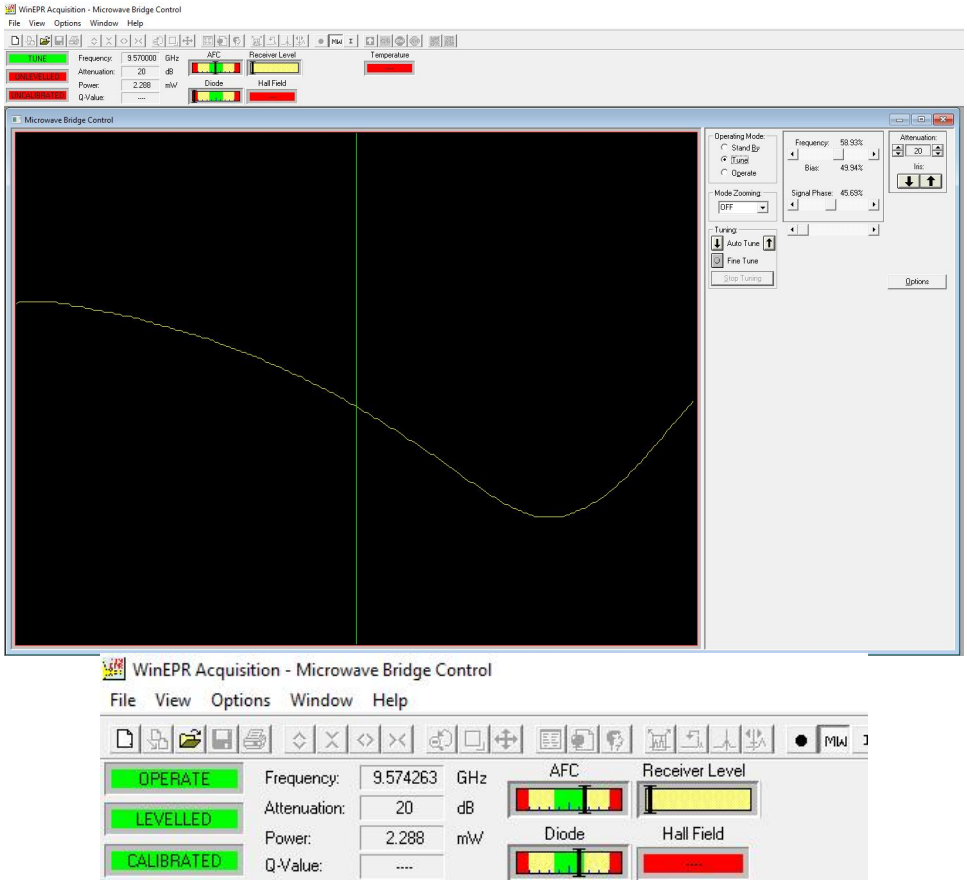

Figure 62: (a) Tuning the resonance of the microwaves and (b) levelling and calibrating the Diode of the detector of the microwave bridge at 320K.

While increasing the temperature more than 325 the microwave resonance started to change so we stopped at 350K in order to see resonance ‘s response as shown in Figure 63.

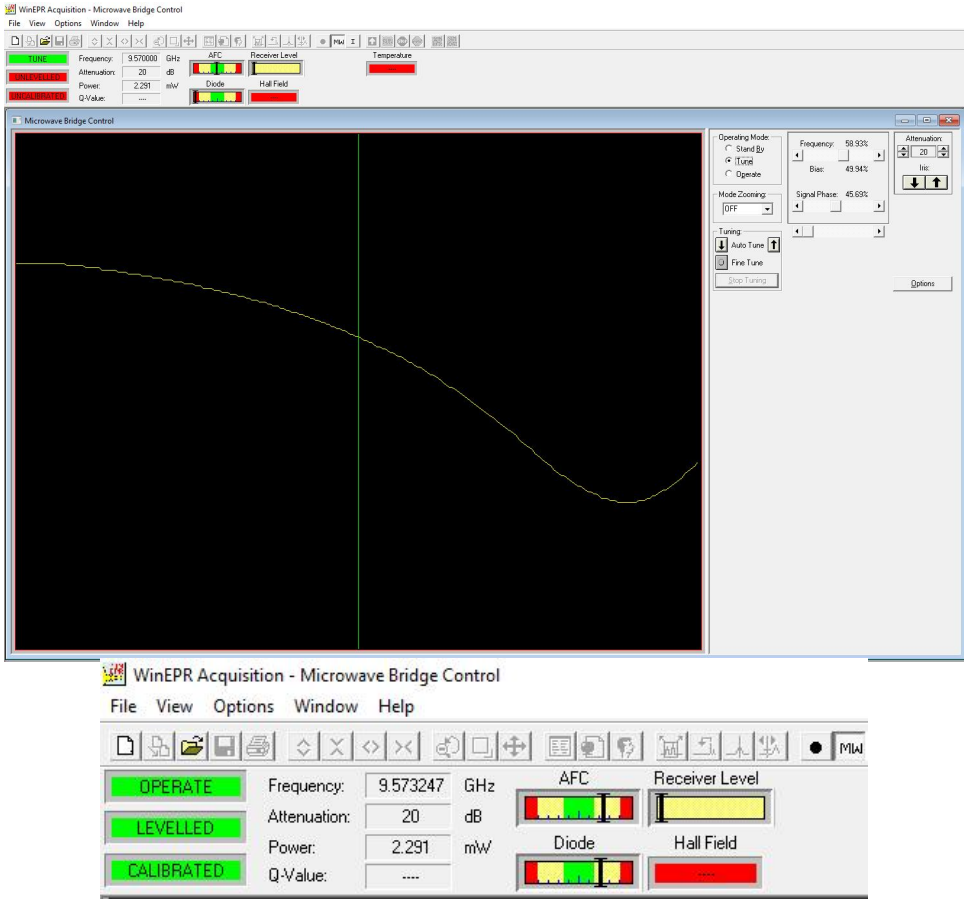

Figure 63: (a) Tuning the resonance of the microwaves and (b) levelling and calibrating the Diode of the detector of the microwave bridge at 350K.

As shown in Figure 63 the AFC was getting out of the "green zone" something that one can see also from the change of the value of the frequency so we had to tune it again and in next Figure 64 we present it after the second tuning.

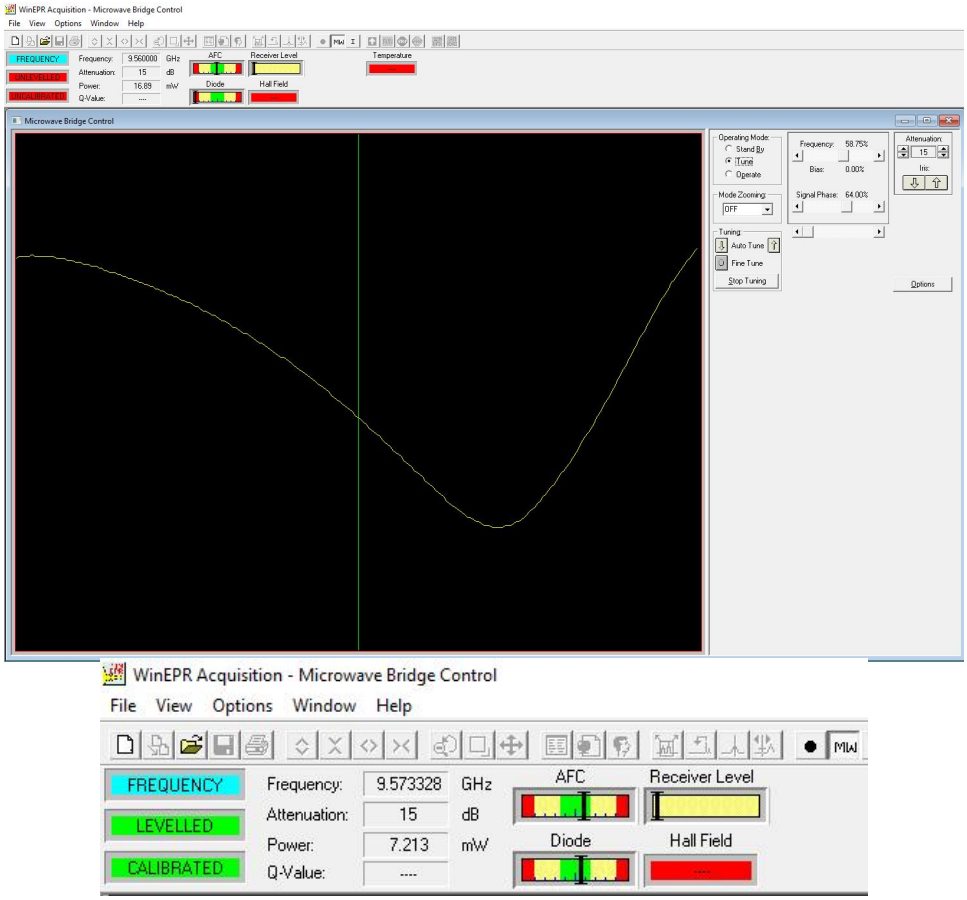

Figure 64: (a) Tuning the resonance of the microwaves and (b) levelling and calibrating the Diode of the detector of the microwave bridge at 350K.

From temperature of 350K and above all the tunings needed to be done two times in order to get the best tuning and get a good microwave resonance signal. In Figures 65 - 67 we present the shape of microwave resonance with the best tuning options by changing the signal phase of the microwave bridge and the iris of the cavity.

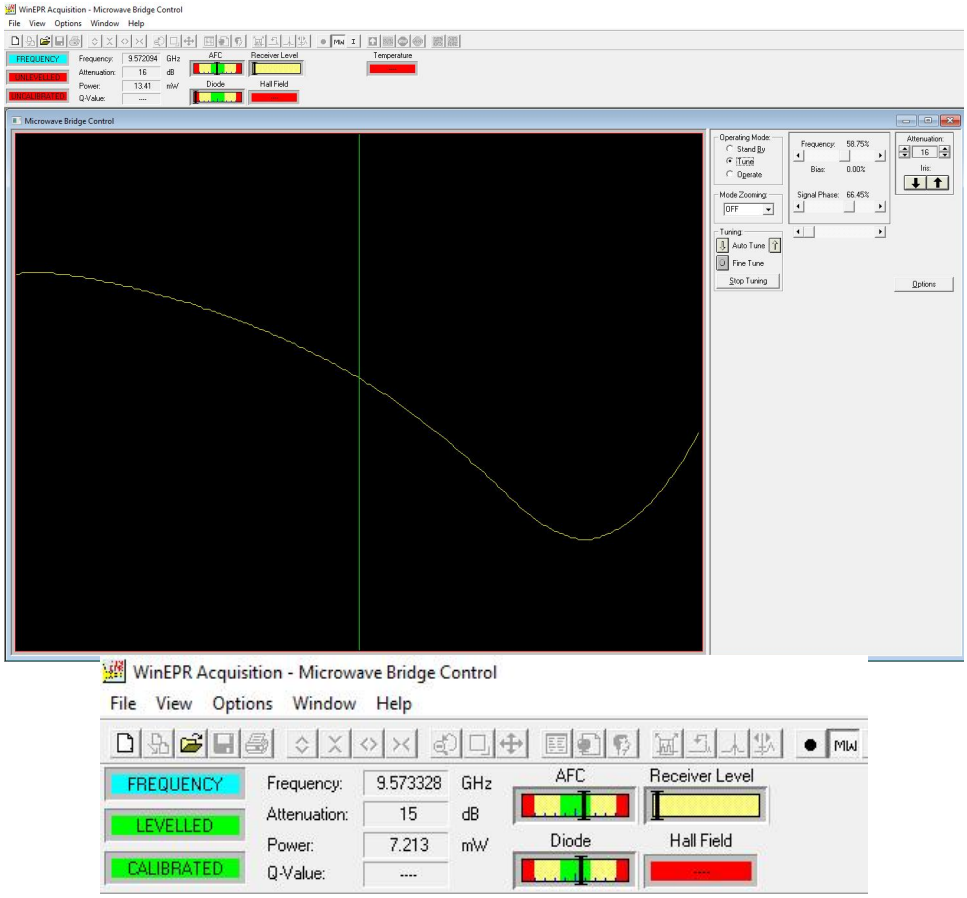

Figure 65: (a) Tuning the resonance of the microwaves and (b) levelling and calibrating the Diode of the detector of the microwave bridge at 400K.

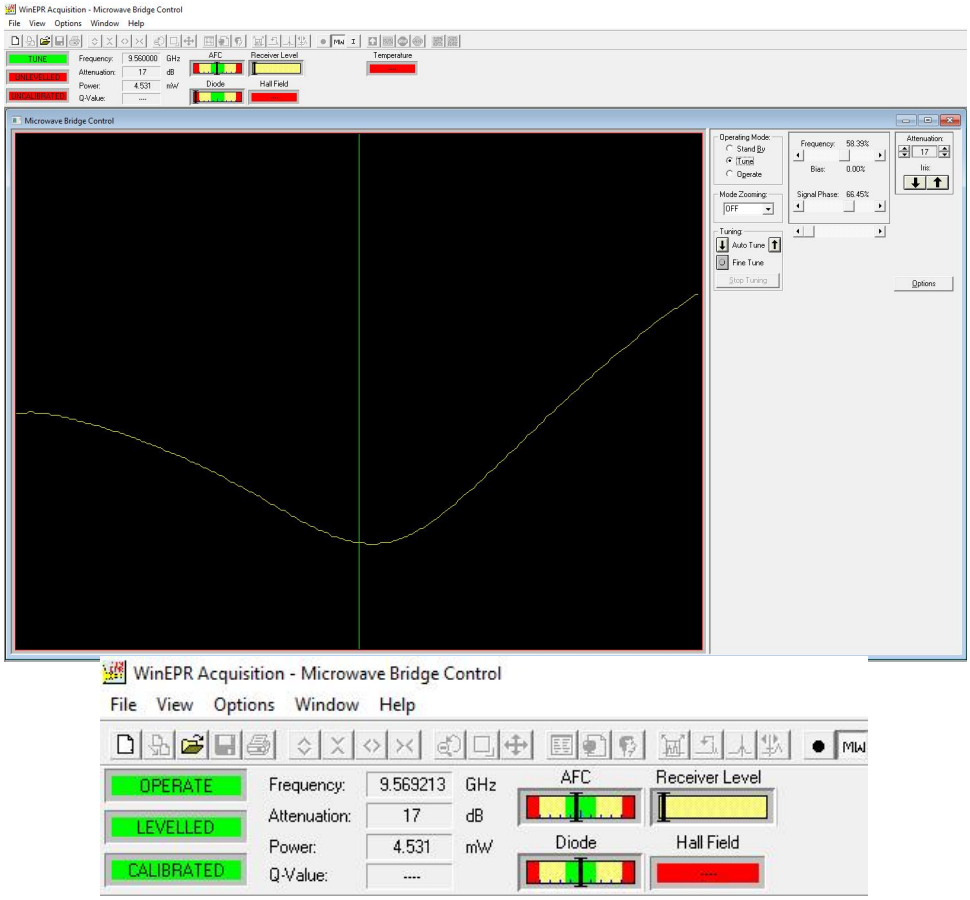

Figure 66: (a) Tuning the resonance of the microwaves and (b) levelling and calibrating the Diode of the detector of the microwave bridge at 500K.

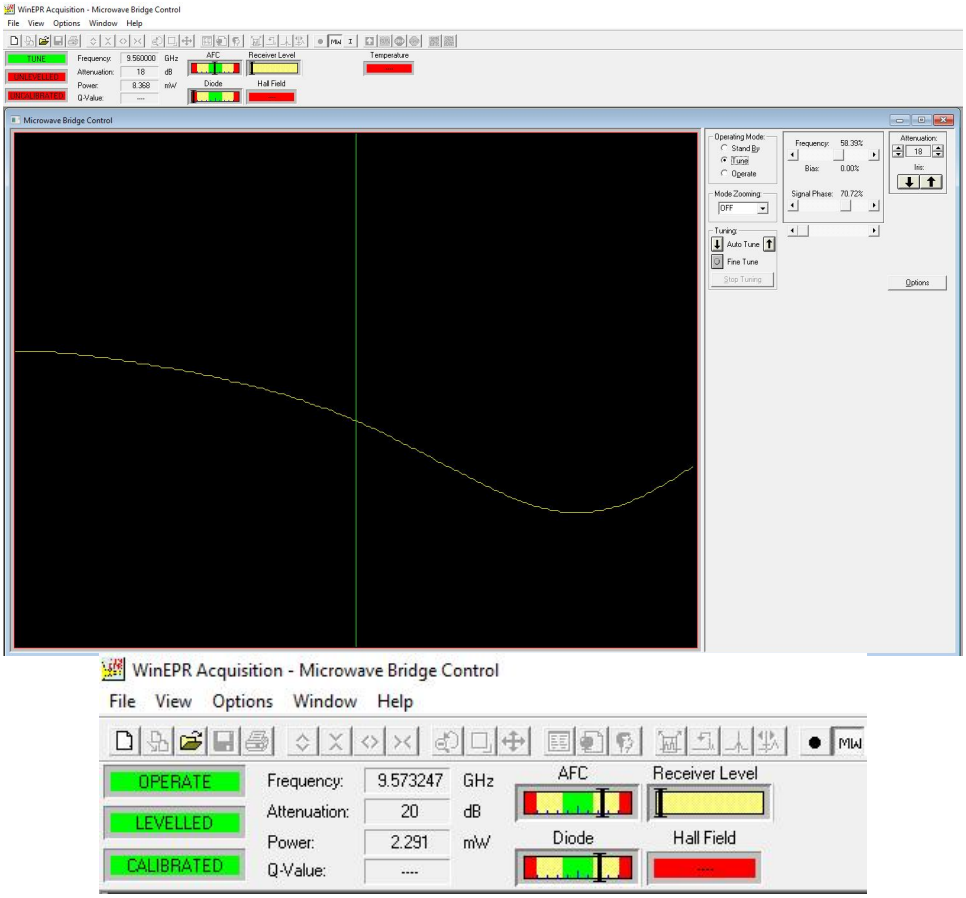

Figure 67: (a) Tuning the resonance of the microwaves and (b) levelling and calibrating the Diode of the detector of the microwave bridge at 550K.

As can be easily noticed by all the Figures in that section the resonance was minimized after a range of ΔT=200K which was a problem. In order to fix that we changed the purging value inside the cavity in order to minimize the humidity factor which easily can minimize the microwave resonance.

4.3 Calibration of Lock-In Amplifier& Modulation

S=1/2 System for Calibration of the Set up.

For calibrating the EPR system we used an organic chemical compound 2,2-diphenyl-1-picrylhydrazyl which more commonly is called DPPH It is a dark-colored crystalline powder composed of stable free radical (S=1/2) molecules. DPPH has two major applications, both in laboratory research: one is a monitor of chemical reactions involving radicals, most notably it is a common antioxidant assay [62] and another is a standard of the position and intensity of electron paramagnetic resonance signals. The commercial powder is a mixture of phases which melts at ~130 °C. In order to find the most optimal values of measurements we had to take some measurements with different values on different settings of the modulation amplifier. At first we tried to measure it by adding to the sample holder 1.2mg of DPPH powder but as shown on Figure 68 the amplitude of the DPPH sample is very high and that's why it's cut-off at 3400G and at 3410G.

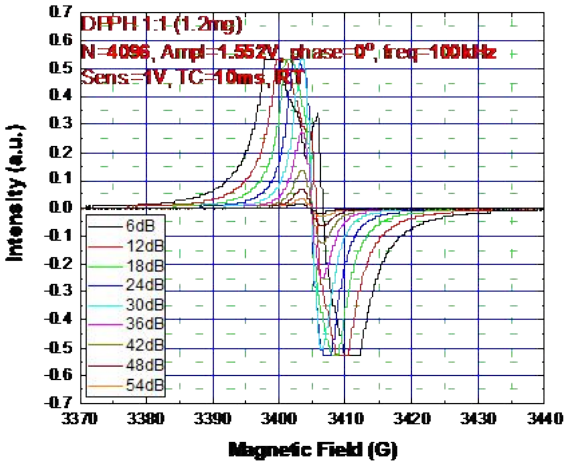

Figure 68: We measured DPPH in a zirconium tube and measured it in RT, in order to find the most appropriate settings to take measurements. 1.2mg DPPH versus microwave source power (dB) though have a very strong signal and that's why in low dB its cut off in EPR spectrum.

In order to measure that sample we had to make a new sample which had 1% wt. DPPH in KBr (KBr is EPR silent, i.e. it doesn't give a signal in EPR measurement). We start the measurements by choosing the number of steps and for each value (512, 1024, 2048, 4096) to choose different time constant (10ms – 100μs) as shown in Figure 69.

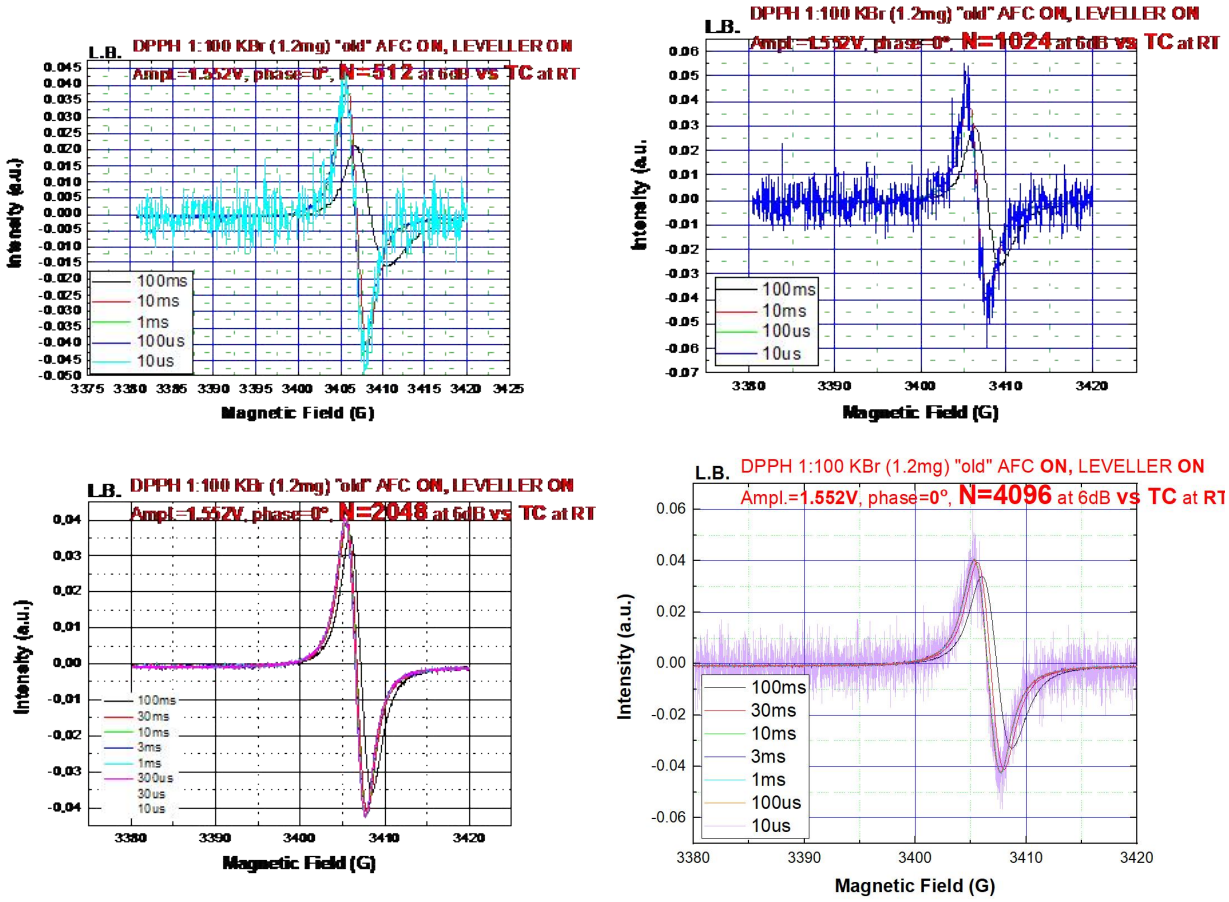

Figure 69: Here we measured the DPPH sample which is diluted in KBr (1:100) at constant 6dB versus time constant and versus number of steps (in how many pieces the sweep width is divided to).

We observe that for N=512 we can measure with a Time Constant in a range of 100μs up to 10ms, after increasing the steps value to 1024 we observed that in the same range of values for time constant the measurements could be made. Then by increasing the steps number to 2048 we observed that the time constant should be in the range from 30μs up to 10ms and finally for 4096 we could measure properly in the range of 100μs up to 30ms. It must be noted that the magnetic field center in all measurements was 3400G with a sweep width of 40G.

After finding the proper settings for time constant we did the same thing to find the most appropriate value of phase of the sinusoidal wave that the modulation amplifier sends to amplify

the signal. We present the results below in Figure 70a for positive phase and Figure 70 for negative phase.

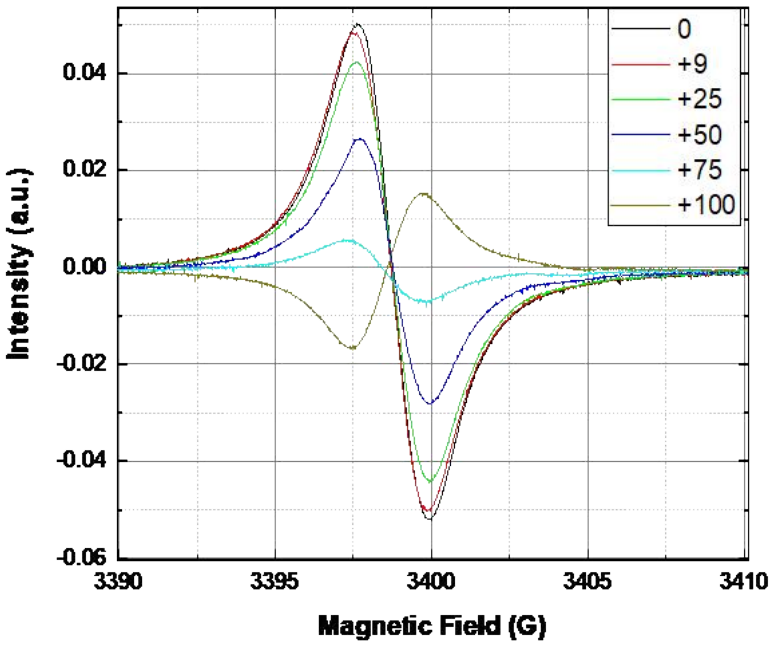

Figure 70a: Here we measured the DPPH sample which is diluted in KBr (1:100) at constant 6dB versus the positive modulation phase of the lock-in amplifier.

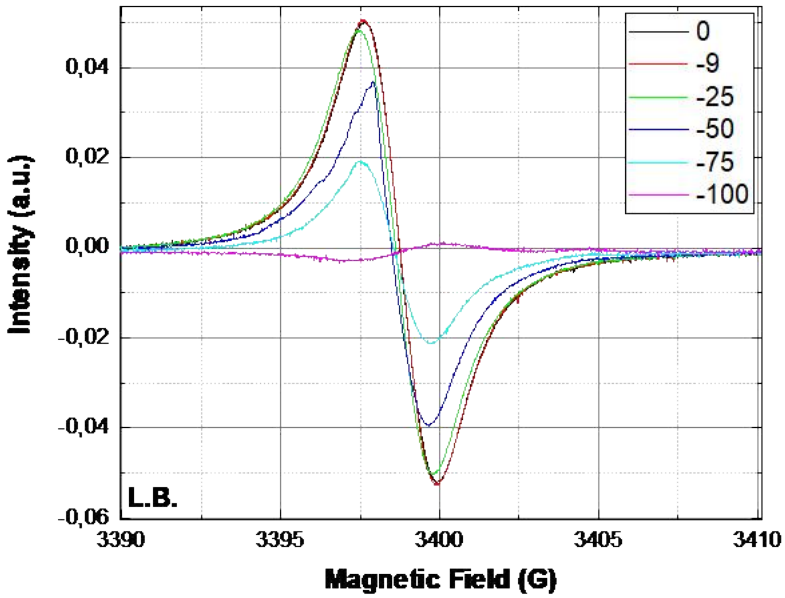

Figure 70b: Here we measured the DPPH sample which is diluted in KBr (1:100) at constant 6dB versus the negative modulation phase of the lock-in amplifier.

After finding the best values for time constant and phase for the amplifier and by keeping the amplitude steady at 1.552V we started our search for the appropriate value of frequency of the amplifier. As the Figure 71 shows we searched at the order of kHz because in lower orders of frequency the relaxation time would be much smaller, i.e. much faster than the frequency of the amplifier and the signal would be zero.

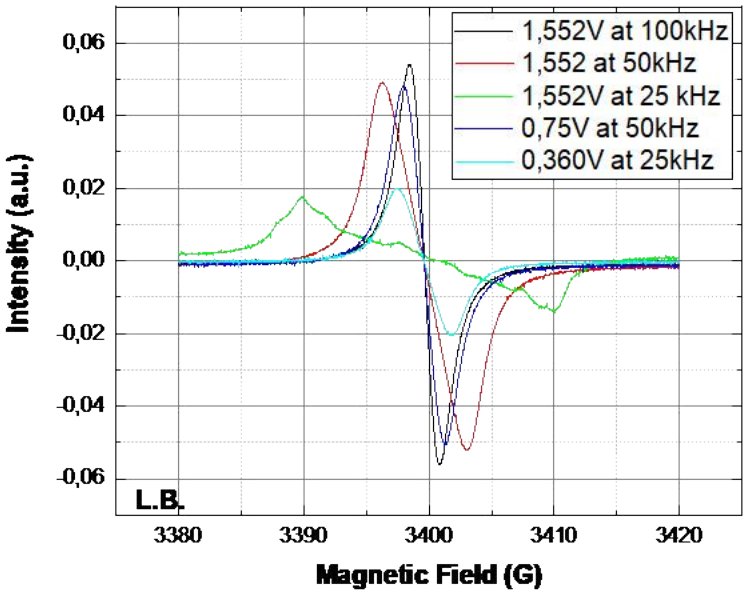

Figure 71: Here we measured the DPPH sample which is diluted in KBr (1:100) at constant 6dB versus the modulation amplitude of the lock-in amplifier and the modulation frequency.

After finishing with the amplifier, we had to search for the settings of the bridge in order to measure the samples. In figure 72 we take measurements of a 1% wt. DPPH in KBr, and we were changing only the dB of the microwave source. With that way we checked that the microwaves are tuning with the cavity.

(a)

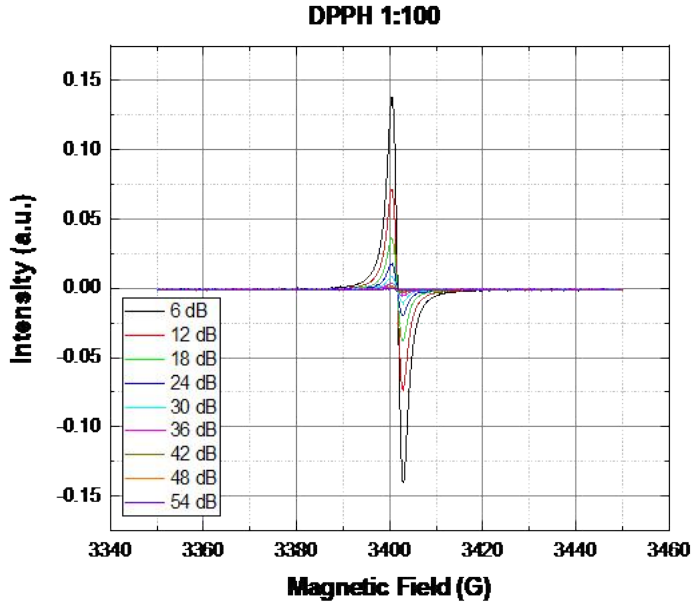

(b)

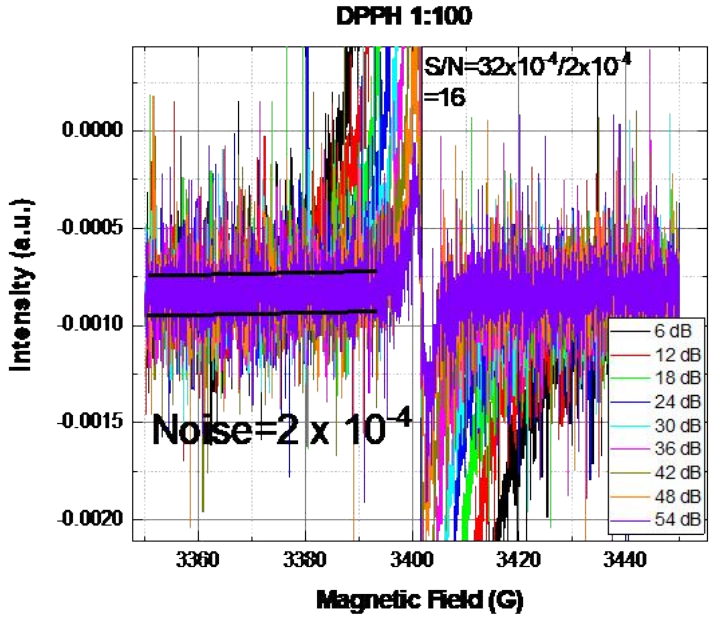

Figure 72: Here we measured the DPPH sample which is diluted in KBr (1:100) versus microwave source power with the optimal settings that we found earlier (the modulation amplitude, the modulation frequency of the lock-in amplifier, the time constant, sensitivity and number of steps)

4.4 APPLICATIONS

- **Isolated spins Mn^{2+} (S=5/2, I=5/2) in a solid matrix at natural marble**

In this application we chose a high spin system (S=5/2) with high nuclear spin (I=5/2), natural marble is such a system. Because of both high spin (5/2, 5/2) it gives rich EPR spectrum. The spins in marble are isolated in a solid matrix of $CaCO_3$, which eliminates any Mn-Mn interactions, thus we have no spin domains. The intensity signals are high from the room temperature, though the temperature dependence on a system like that is important because from the changes of lineshape or linewidth much information about its environment can be received. Because Mn^{2+} ions are isolated in the matrix we have no Mn-Mn interactions, thus no spin domain system. The case of ferromagnetic materials with spin domains was examined in the second application of this thesis.

- **Spin domains in superparamagnetic nanoparticles of Fe_2O_3 (S=5/2)**

In this application again a high spin system was studied, with the difference that ions aren't any more isolated in a matrix, but they interact with each other and with that way the particle is divided to spin domains as shown in Figure 29. In this application all the factors that we explained before are important like the intensity, line-width and line-shape, but also other factors that haven't taken place in that thesis like surface effects.

4.4.1 APPLICATION #1

Isolated spins Mn^{2+} (S=5/2, I=5/2) in a solid matrix at natural marble

The method of measuring digitally on High Temperature EPR works. We succeed on measuring Mn^{2+} ions transitions. We covered all the range from 300K up to 750K with a step of 25K. All the factors that we needed were well-recorded and the parameters of measurements. There are two types of disordered materials: glasses and polycrystalline powders. The Mn^{2+} ion in these materials can be characterized by either well-defined values of spin-Hamiltonian parameters (in constituting crystallites), or a distribution of these around mean values (in glasses), or a combination of both. It's a very good application because in the EPR spectrum we expect to see six first-order (sextet) transitions but also some forbidden hyperfine transitions. Those forbidden hyperfine transitions will be seen as doublet separations (m=-3/2, -1/2, 1/2, 3/2, 5/2). By having a spin larger than ½ its spectrum reflects interaction with the environment and temperature dependence of the EPR line-shape, line-width offers rich information. Line narrowing phenomena were observed at T>400K and all the transitions where visible. No phase transition occurs for $CaCO_3$ matrix in the temperature range at 300K up to 750K. In Figure 73 we present the theoretical transitions for this system with spin S=5/2 and nuclear spin I=5/2. In Figure 74 we show all the temperatures from 300K up to 700K, we assigned the peaks based on the transition type, the normal letters (α, β, γ, δ, ε, ζ) show the first order transitions and they are six, thus we have the basic sextet of peaks and the accented letters (α′, β′, γ′, δ′, ε′) are the doublets of forbidden hyperfine transitions. In Figures 75-81 we show the changes of the spectrums with the changes of the temperature with a step of 25K for each measurement to show the importance of a digitally controlled High Temperature EPR. In each Figure of those we start by showing the full spectrum and then the subfigures which are presented by adding them a letter. The subfigures with letter (a) are targeted to the first order transition as shown in Figure 74 with letter α and to the first doublet of forbidden transitions with the letter α', the subfigures with letter (b) are targeted firstly to the last doublet of forbidden transitions with letter ε' of Figure 74 and then the last first-order transition which is coded with letter ζ.

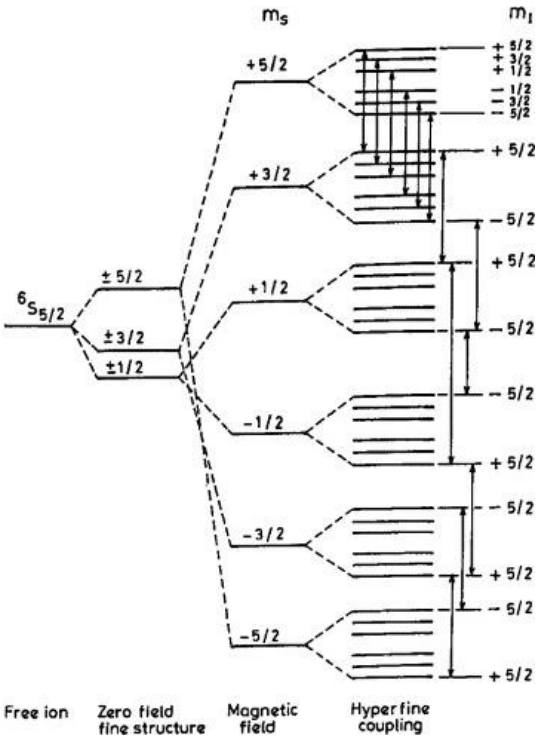

Figure 73: Theoretical Model first order transitions and hyperfine transitions.

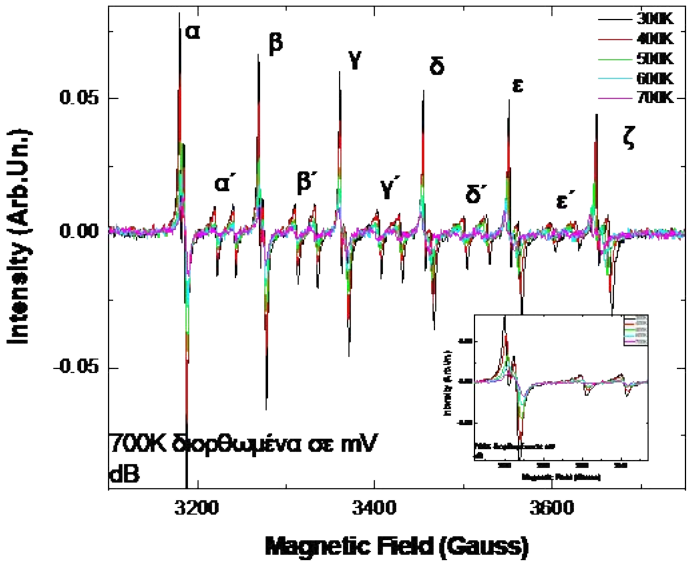

Figure 74: In this figure the first H.T. EPR spectrum, of natural marble, is presented in a wide range of 300K up to 700K. In this spectrum both types of interactions can be observed the first order with normal letters and the forbidden hyperfine interactions with accented letters.

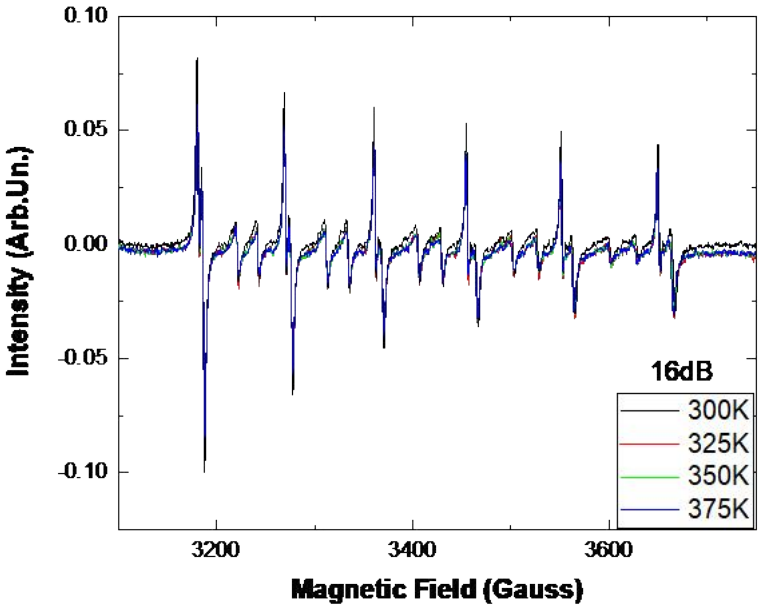

Figure 75: In this figure we show a H.T. full EPR spectrum of natural marble, a full spectrum of the sample in a range from 300K up to 375K.

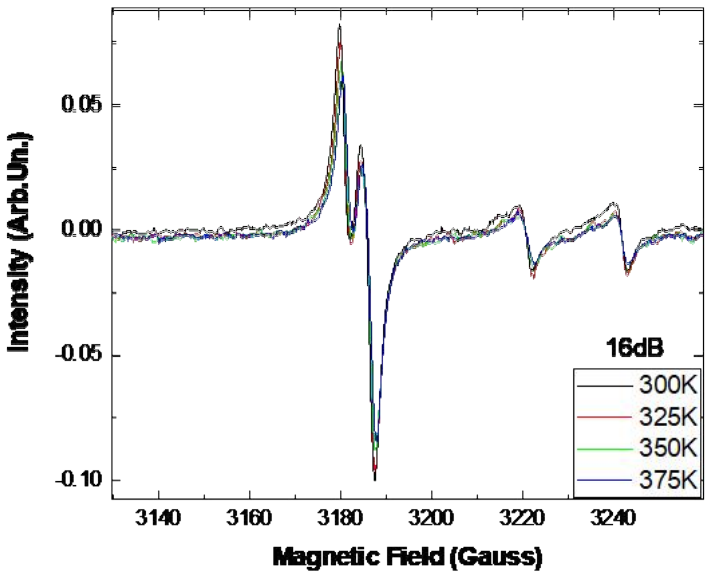

Figure 75a: In this figure we show a H.T. EPR spectrum, of natural marble, in which it's in a temperature range from 300K up to 375K. The spectrum is targeted to the first order transition and to the first doublet of forbidden transitions.

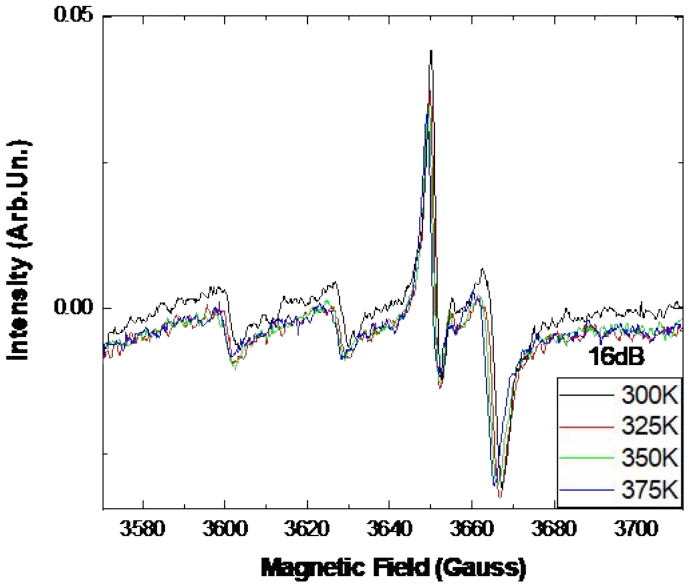

Figure 75b: In this figure we show a H.T. EPR spectrum, of natural marble, in which it's in a temperature range from 300K up to 375K. The spectrum is targeted to the last doublet of forbidden transitions and to the last first-order transition.

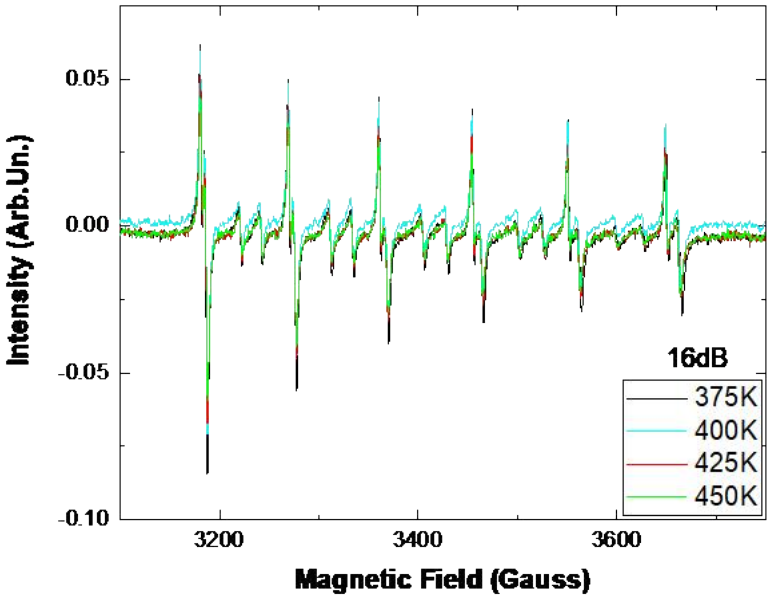

Figure 76: In this figure we show a H.T. full EPR spectrum of natural marble, a full spectrum of the sample in a range from 375K up to 450K.

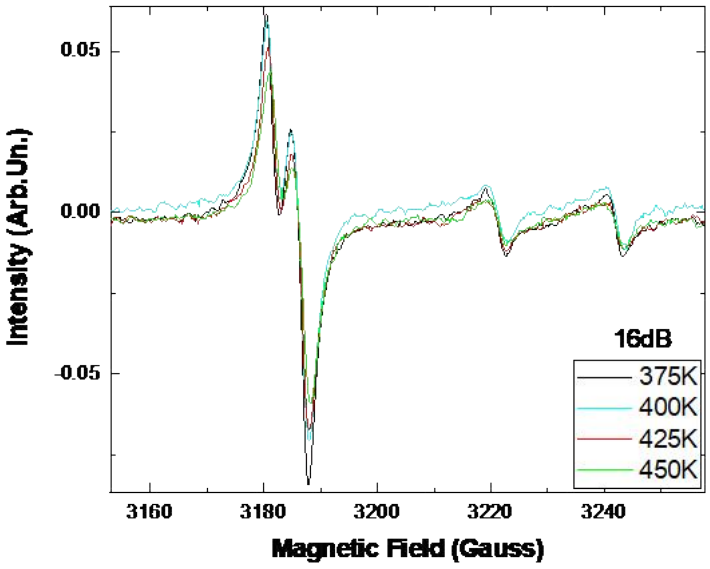

Figure 76a: In this figure we show a H.T. EPR spectrum, of natural marble, in which it's in a temperature range from 375K up to 450K. The spectrum is targeted to the first order transition and to the first doublet of forbidden transitions.

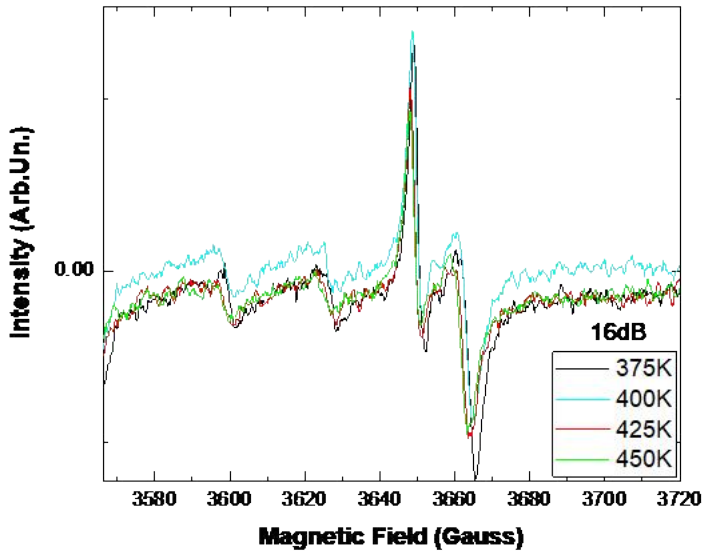

Figure 76b: In this figure we show a H.T. EPR spectrum, of natural marble, in which it's in a temperature range from 300K up to 375K. The spectrum is targeted to the last doublet of forbidden transitions and to the last first-order transition.

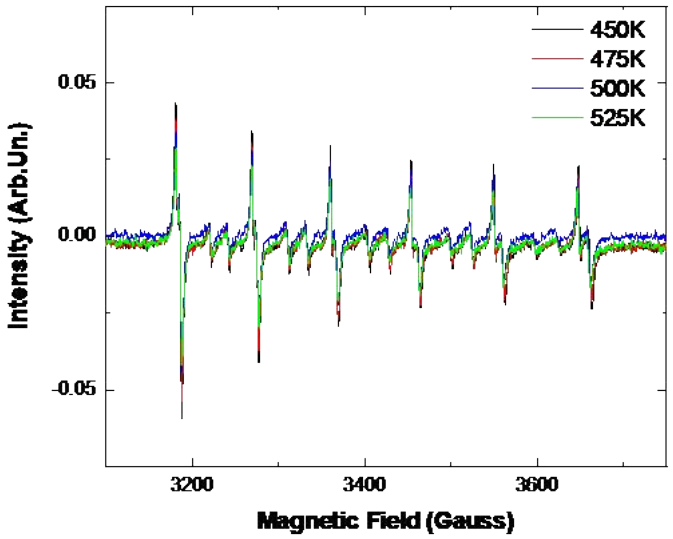

Figure 77: In this figure we show a H.T. full EPR spectrum of natural marble, a full spectrum of the sample in a range from 450K up to 525K.

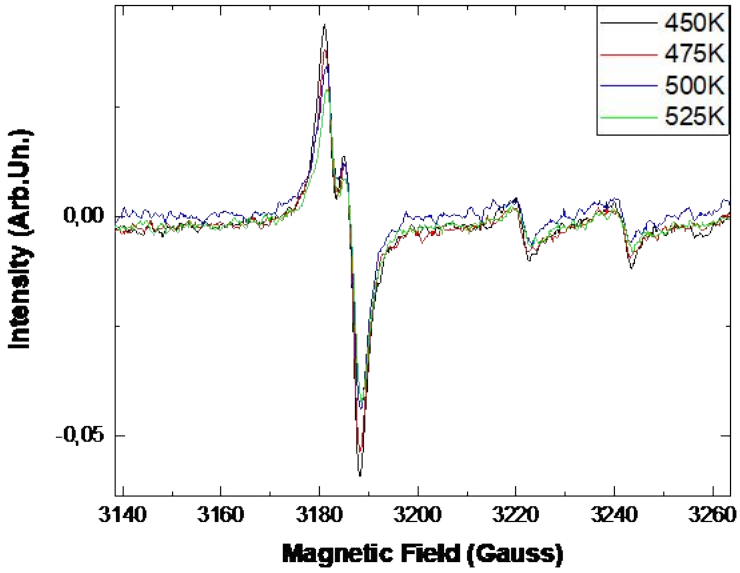

Figure 77a: In this figure we show a H.T. EPR spectrum, of natural marble, in which it's in a temperature range from 450K up to 525K. The spectrum is targeted to the first order transition and to the first doublet of forbidden transitions.

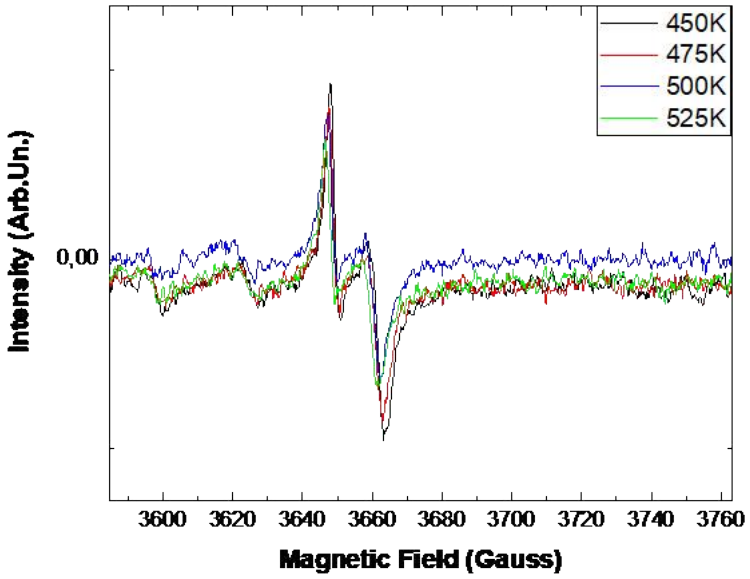

Figure 77b: In this figure we show a H.T. EPR spectrum, of natural marble, in which it's in a temperature range from 300K up to 375K. The spectrum is targeted to the last doublet of forbidden transitions and to the last first-order transition.

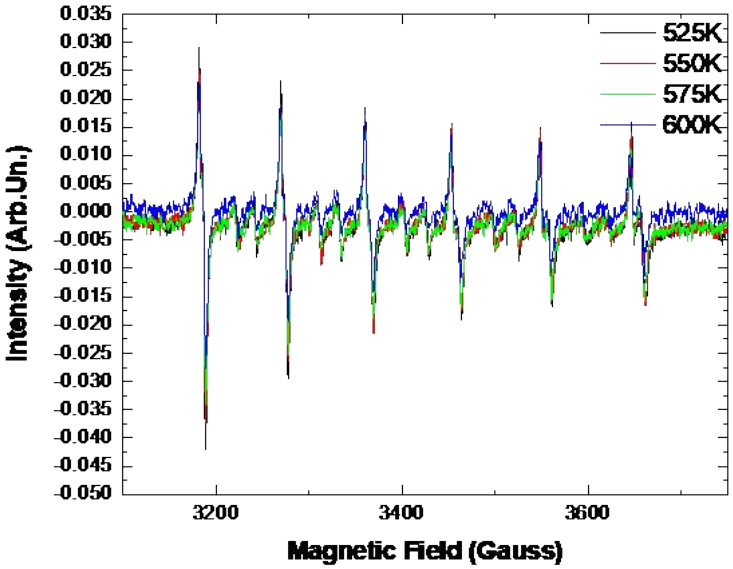

Figure 78: In this figure we show a H.T. full EPR spectrum of natural marble, a full spectrum of the sample in a range from 525K up to 600K.

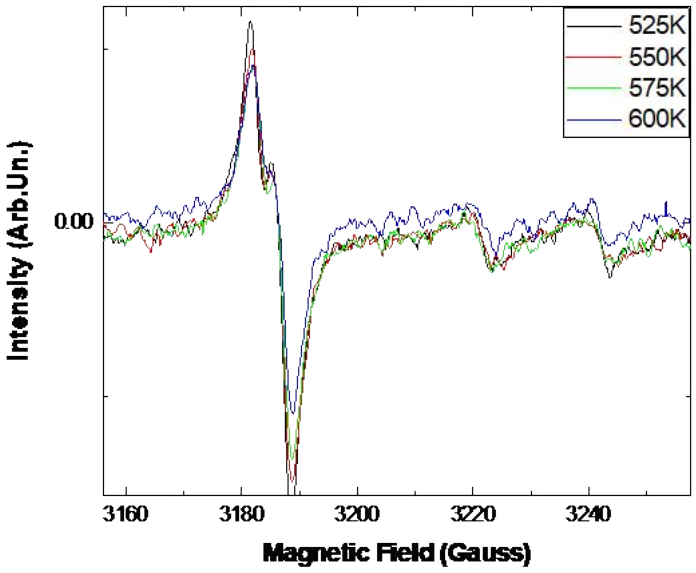

Figure 78a: In this figure we show a H.T. EPR spectrum, of natural marble, in which it's in a temperature range from 525K up to 600K. The spectrum is targeted to the first order transition and to the first doublet of forbidden transitions.

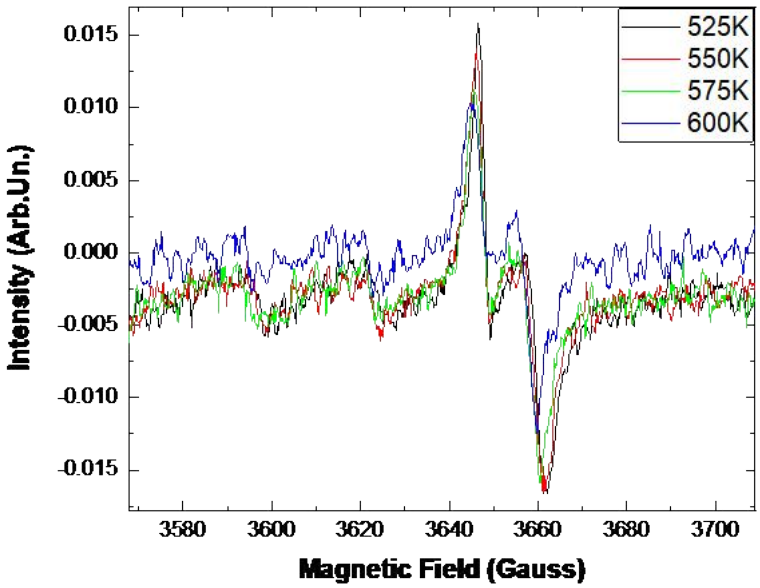

Figure 78b: In this figure we show a H.T. full EPR spectrum of natural marble, a full spectrum of the sample in a range from 525K up to 600K.

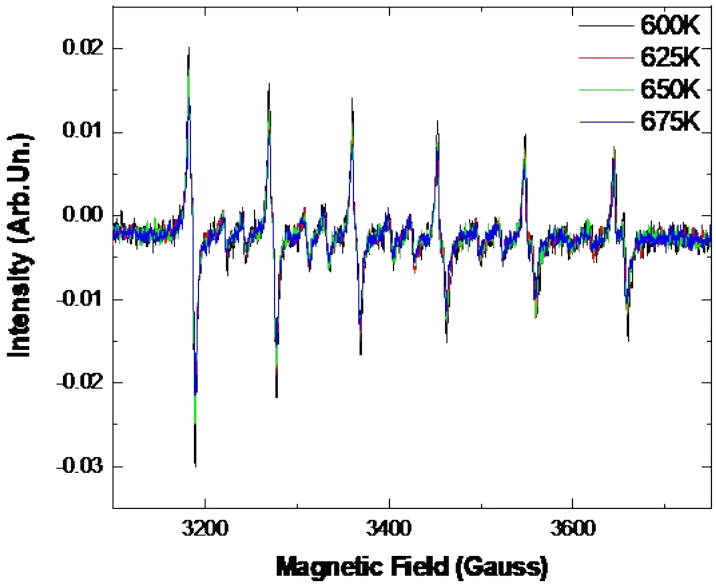

Figure 79: In this figure we show a H.T. full EPR spectrum of natural marble, a full spectrum of the sample in a range from 600K up to 675K.

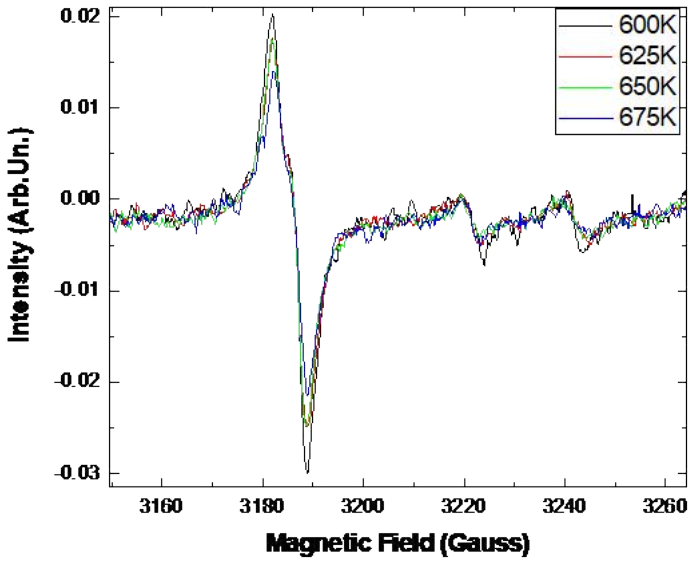

Figure 79a: In this figure we show a H.T. EPR spectrum, of natural marble, in which it's in a temperature range from 600K up to 675K. The spectrum is targeted to the first order transition and to the first doublet of forbidden transitions.

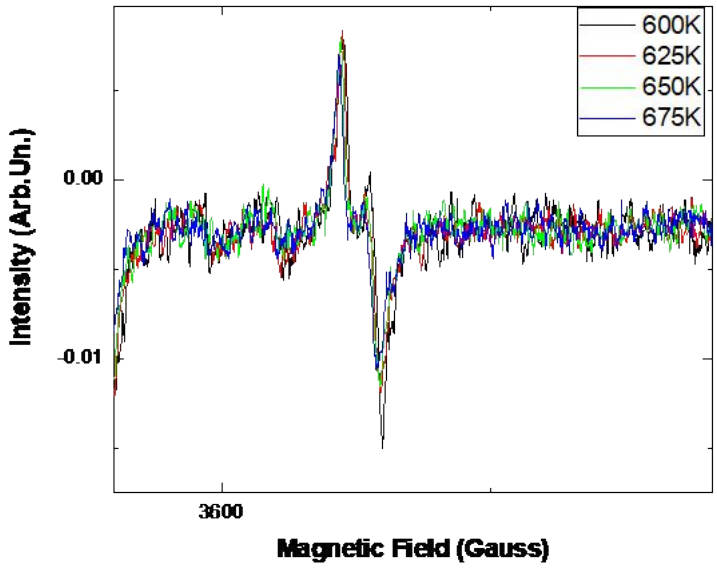

Figure 79b: In this figure we show a H.T. full EPR spectrum of natural marble, a full spectrum of the sample in a range from 600K up to 675K.

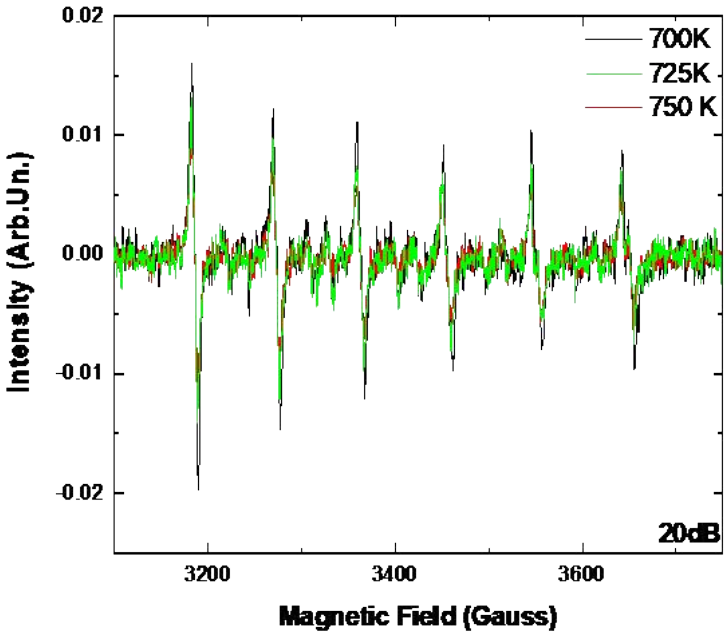

Figure 80: In this figure we show a H.T. full EPR spectrum of natural marble, a full spectrum of the sample in a range from 700K up to 750K.

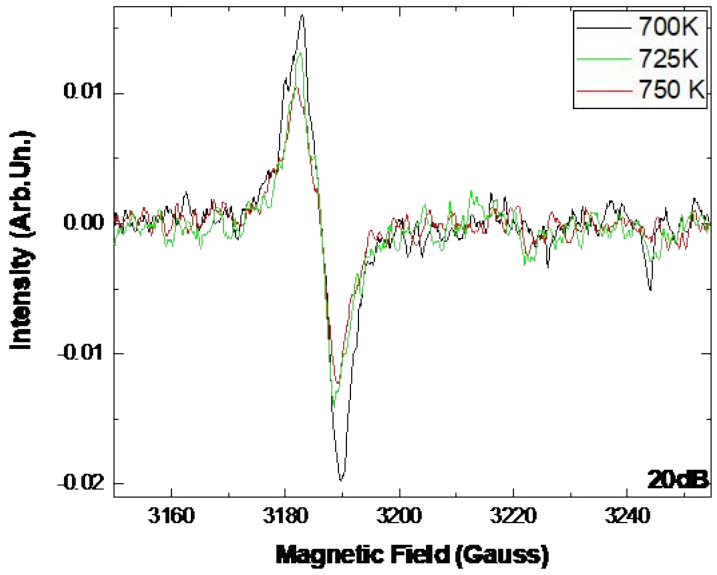

Figure 80a: In this figure we show a H.T. EPR spectrum, of natural marble, in which it's in a temperature range from 700K up to 750K. The spectrum is targeted to the first order transition and to the first doublet of forbidden transitions.

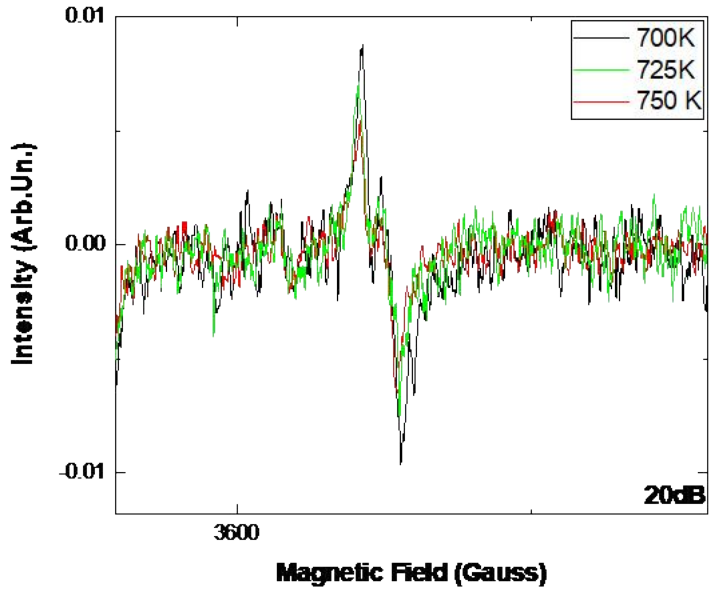

Figure 80b: In this figure we show a H.T. full EPR spectrum of natural marble, a full spectrum of the sample in a range from 525K up to 600K.

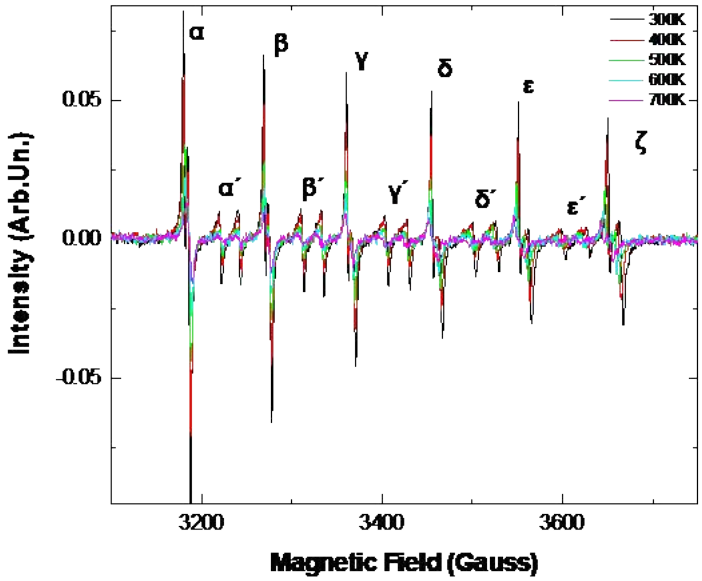

Figure 81: In this figure we show a H.T. full EPR spectrum of natural marble, a full spectrum of the sample in a range from 300K up to 700K.

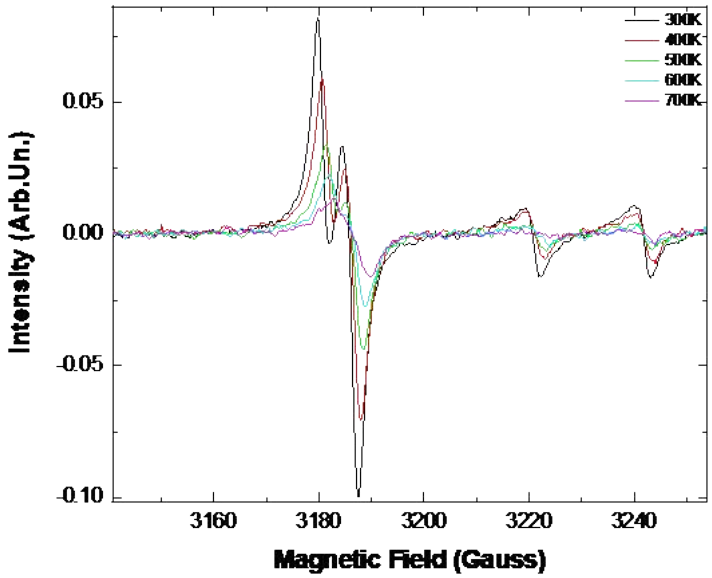

Figure 81a: In this figure we show a H.T. EPR spectrum, of natural marble, in which it's in a temperature range from 300K up to 700K. The spectrum is targeted to the first order transition and to the first doublet of forbidden transitions.

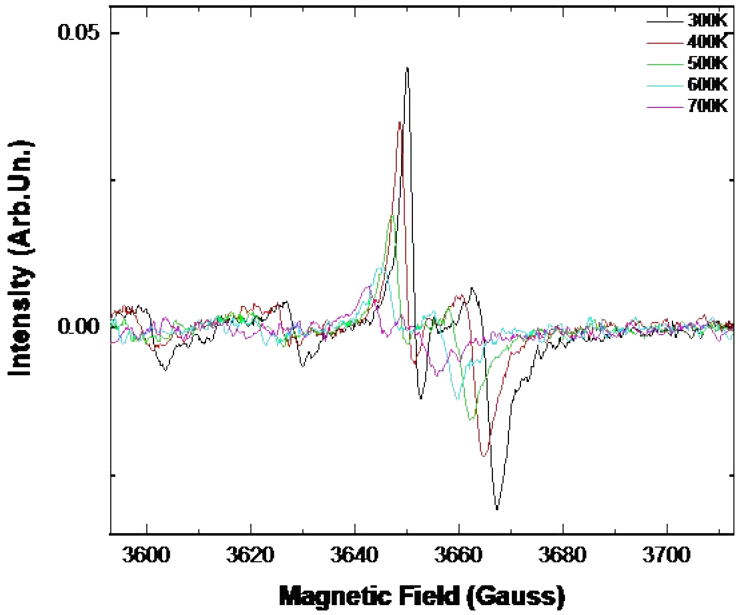

Figure 81b: In this figure we show a H.T. full EPR spectrum of natural marble, a full spectrum of the sample in a range from 300K up to 700K.

In Figure 82 we demonstrate the dependence of linewidth versus temperature. We noticed that with the increase of the temperature the peaks of the first order transitions are changing. The linewidth can change up to 3G over the measured temperature range. We stopped the measuring of this sample because after 750K we don't expect any changes, a proof of that is that from 700K up to 750K the linewidth change is saturated. In Figure 83 we demonstrate the dependence of intensity of each peak versus temperature. We noticed that with the increase of the temperature the peaks of the first order transitions are changing. The intensity can change up to 0.10 units over the measured temperature range. We stopped the measuring of this sample because after 750K we don't expect any changes, a proof of that is that from 700K up to 750K the intensity change is saturated.

In Table 5 all the settings for each of our measurements are recorded, all the data that are given in the spectrums in this thesis are corrected to the same mV and dB in order to be comparable.

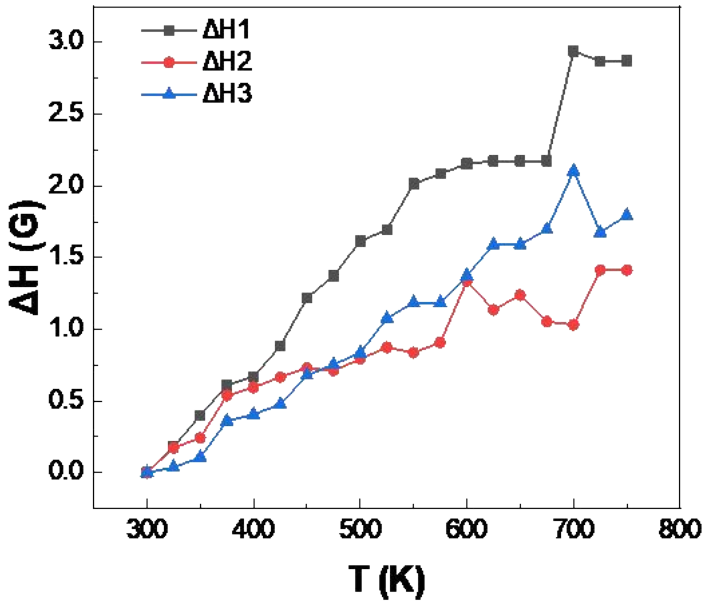

Figure 82: In this Figure are the results of the linewidth change versus temperature from all Figures 75-81 for the first three peaks of (α) as it is mentioned in Figure 81.

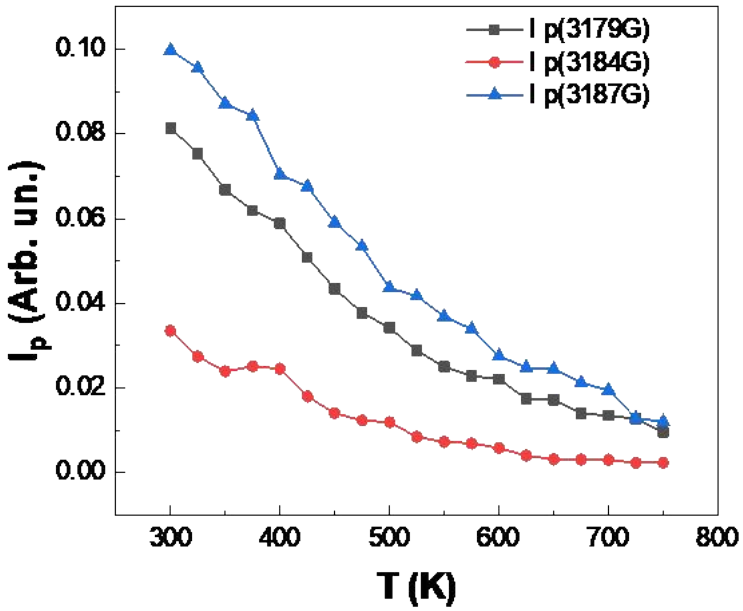

Figure 83: In this Figure are the results of the intensity change versus temperature from all Figures 75-81 for the first three peaks of (α) as it is mentioned in Figure 81.

H.T. Booster		**Field Controller**		**Lock-In Modulation Amplifier**					**Bridge**
Temperature (K)	***N_2 flow***	***Field Center (G)***	***Sweep Width (G)***	***Modulation Amplitude (V)***	***Frequency (kHz)***	***phase (^{o})***	***Sensitivity (mV)***	***Time Constant (ms)***	***MW power source (dB)***
300	0	3400	800	1.552	100	180	5	10	16
325	2	3400	800	1.552	100	180	5	10	16
350	2	3400	800	1.552	100	180	5	10	16
375	2	3400	800	1.552	100	180	5	10	16
400	3	3400	800	1.552	100	180	5	10	16
425	3	3400	800	1.552	100	180	5	10	16
450	3	3400	800	1.552	100	180	5	10	16
475	3	3400	800	1.552	100	180	5	10	16
500	4	3400	800	1.552	100	180	5	10	16
525	4	3400	800	1.552	100	180	5	10	16
550	4	3400	800	1.552	100	180	5	10	16
575	4	3400	800	1.552	100	180	5	10	16
600	4	3400	800	1.552	100	180	1	10	16
625	4	3400	800	1.552	100	180	5	10	17
650	5	3400	800	1.552	100	180	2	10	17
675	5	3400	800	1.552	100	180	2	10	17
700	5	3400	800	1.552	100	180	2	10	17
725	5	3400	800	1.552	100	180	2	10	20
750	5	3400	800	1.552	100	180	2	10	20

Table 5: The settings for all H.T. EPR components are in this Table for the measurements of natural marble in all the range of the temperature.

Summary #1

The method of measuring digitally on High Temperature EPR works. We succeed on measuring Mn^{2+} ions transitions in a range from 300K up to 750K with a step of 25K. All the factors that we needed were well-recorded and the parameters of measurements. In this application we noticed six first-order (sextet) transitions but also some forbidden hyperfine transitions. Those forbidden hyperfine transitions will be seen as doublet separations (m=-3/2, -1/2, 1/2, 3/2, 5/2).

A spin larger than ½ its spectrum reflects interaction with the environment and temperature dependence of the EPR intensity and line-width changes has been examined in Figure 82, 83. Line narrowing phenomena were observed at T>400K and all the transitions where visible up to 3G. No phase transition occurs for $CaCO_3$ matrix in the temperature range at 300K up to 750K.

In Figures 75-81 we show our H.T. EPR spectrums with the changes of the temperature with a step of 25K for each measurement to show the importance of a digitally-stable controlled High Temperature EPR.

4.4.2 APPLICATION #2

Spin domains in superparamagnetic nanoparticles of Fe_2O_3 (S=5/2)

The measurement of those ferromagnetic nanoparticles are an important application in which H.T. EPR can provide unique information that common EPR can't. In those materials that we examined we see changes in three all different factors, i.e. it is much more complex system to investigate than an isolated spin system as the one we measured in Application #1 above. Therefore intensity, line-width and line-shape character are changing. The spectrums for RT will be the same as if they were taken by a common EPR in RT, in lower temperatures the blocking effect is expected to occur in the system of ferromagnetic nanoparticles. Above the blocking temperature Tb thermal fluctuations predominate over anisotropic magnetic interactions and the magnetic moments of the nanoparticles show a superparamagnetic behavior, whereas below Tb a ferromagnetic behavior is observed, corresponding to a steady state. The blocking effect has been observed and discussed for many superparamagnetic systems, the blocking temperature is defined as the temperature at which the relaxation time τ_1 of the magnetic moments equals to the measuring time t_m. In this application we will focus on High Temperatures though where The observed temperature dependence of the linewidth is accounted for by thermal fluctuation induced averaging of the magnetocrystalline anisotropy energy [55].

#1 Fe_2O_3

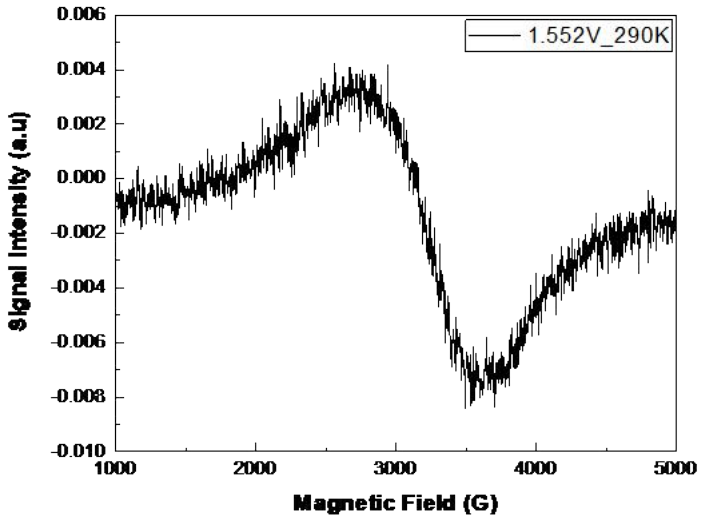

Figure 84: In this figure we show a H.T. EPR spectrum, of ferromagnetic nanoparticle (#1) in room temperature.

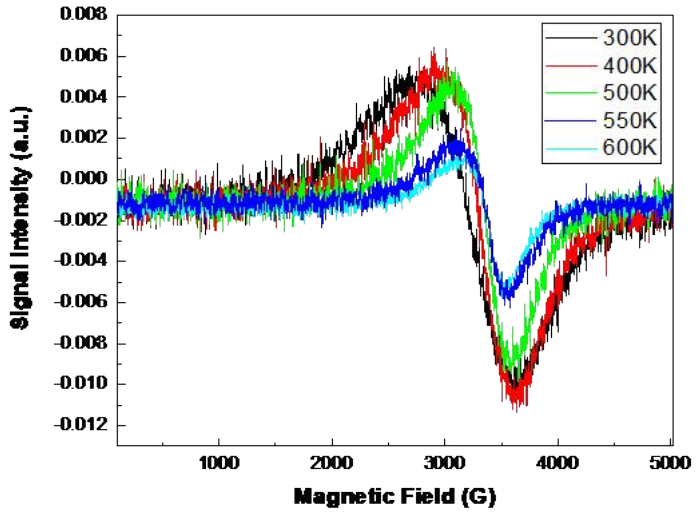

Figure 85: In this figure we show a H.T. EPR spectrum, of ferromagnetic nanoparticle (#1) in temperature range from 300K up to 600K.

#2 Fe_2O_3

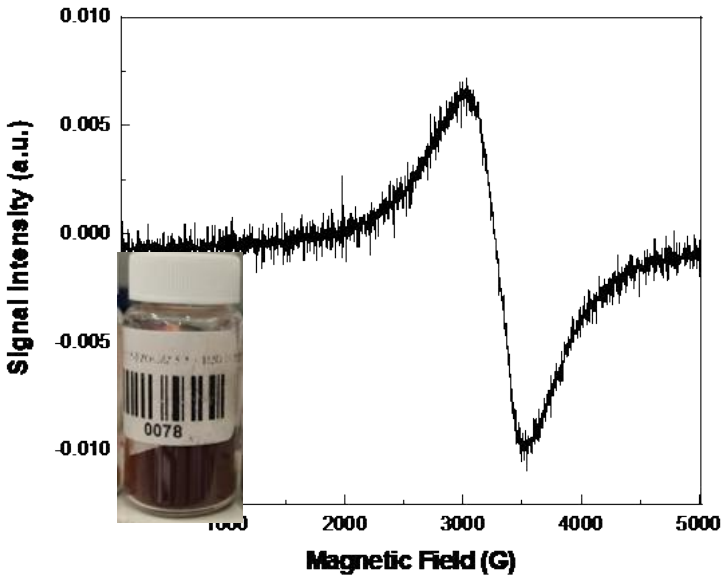

Figure 86: In this figure we show a H.T. EPR spectrum, of ferromagnetic nanoparticle (#2) in room temperature.

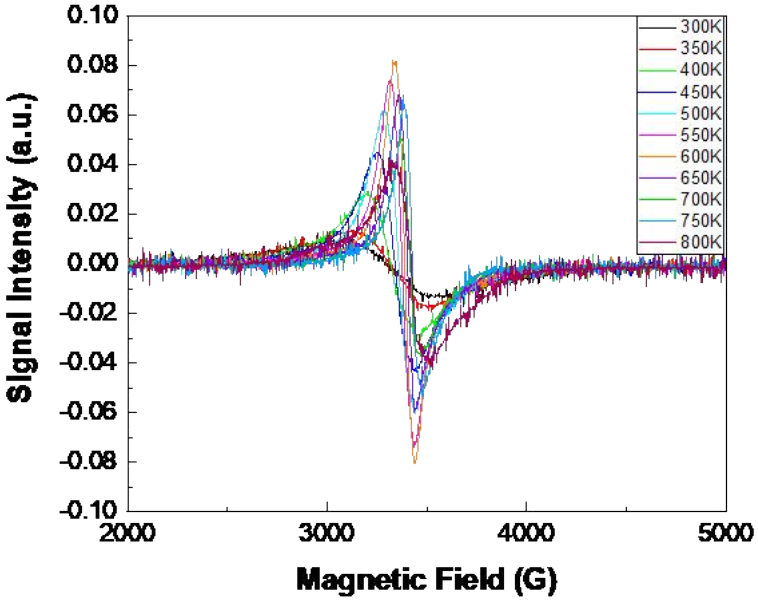

Figure 87: Figure 85: In this figure we show a H.T. EPR spectrum, of ferromagnetic nanoparticle (#1) in temperature range from 300K up to 800K.

#3 Fe_2O_3

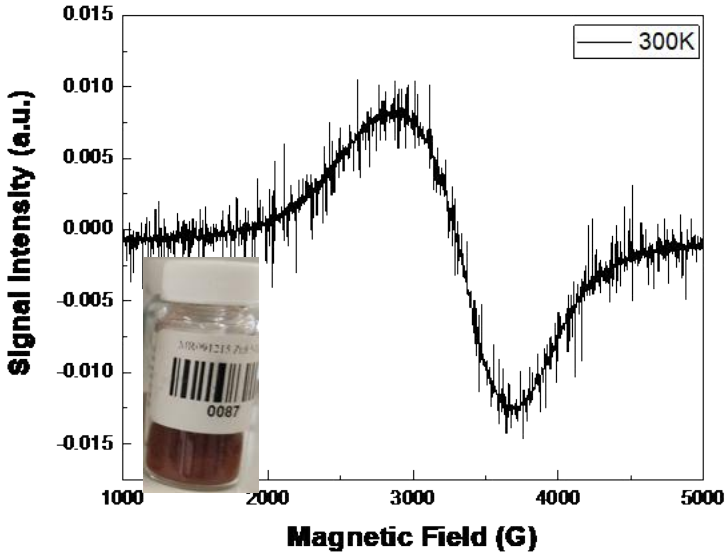

Figure 88: In this figure we show a H.T. EPR spectrum, of ferromagnetic nanoparticle (#3) in room temperature.

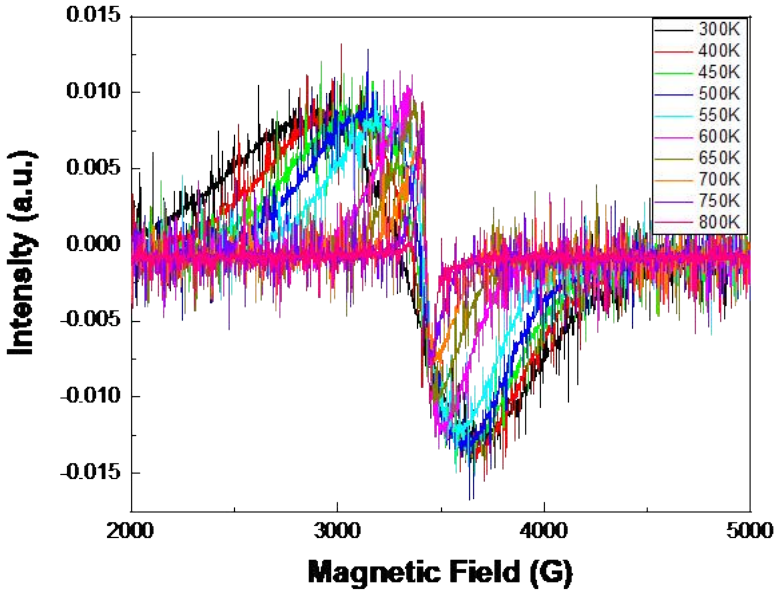

Figure 89: Figure 85: In this figure we show a H.T. EPR spectrum, of ferromagnetic nanoparticle (#1) in temperature range from 300K up to 800K.

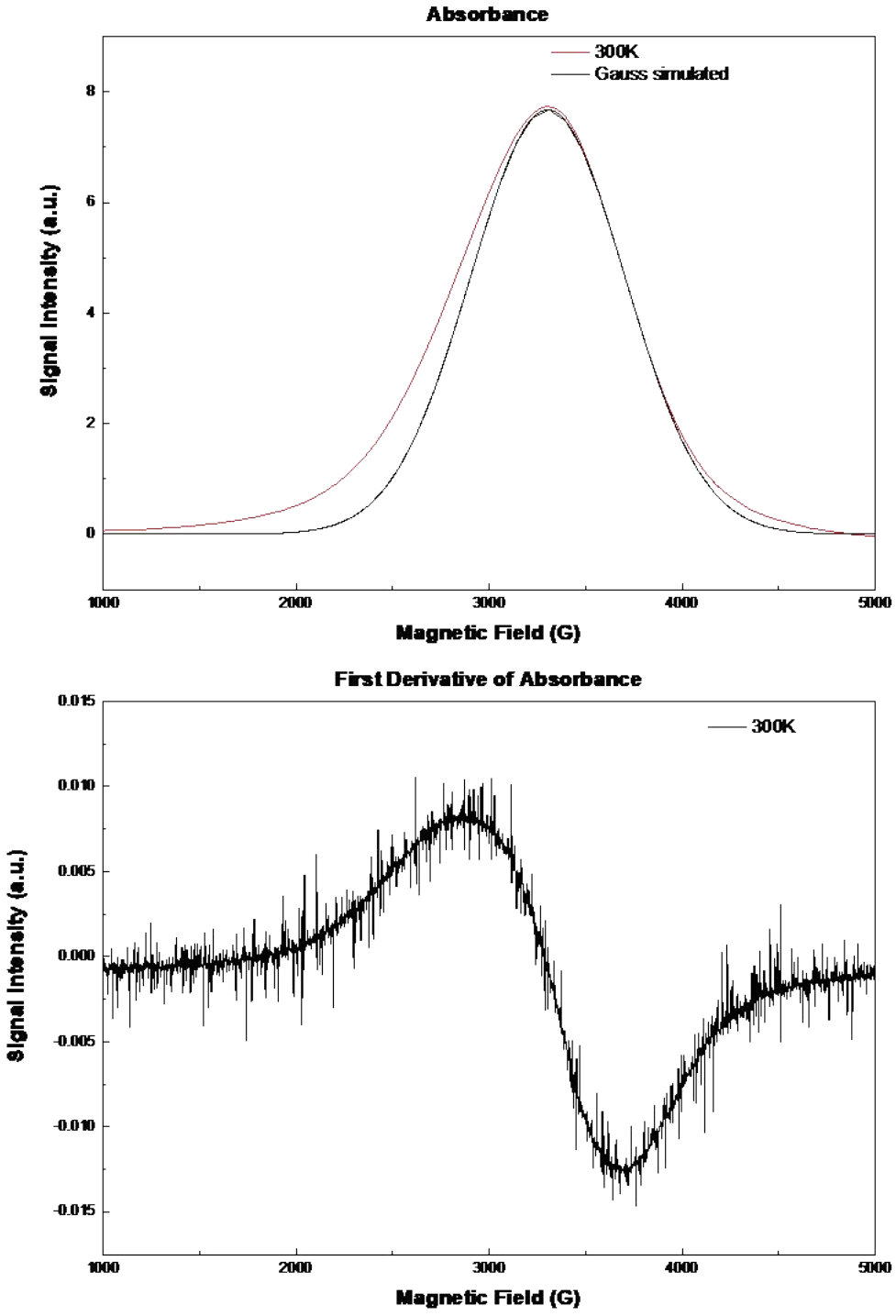

Figure 89: In this Figure we present a simulation of a Gauss curve in Origin in order to find the L/G percentage factor to find the change in line-shape in every temperature change as shown in Table 6.

Sample	Temperature (K)	$I_{(p-p)}$	$\Delta H_{(p-p)}$ (G)	L/G (%)
#1 Fe_2O_3	300	0.01452	889.19	5 / 95
	400	0.01550	693.57	7.3 / 92.7
	500	0.01329	511.63	10.5 / 89.5
	600	0.00612	361.15	12 / 88
#2 Fe_2O_3	300	0.02233	487.01	
	400	0.05649	251.27	
	500	0.12029	173.74	
	600	0.16180	99.86	
	700	0.08733	94.4	
	800	0.07893	181.94	
#3 Fe_2O_3	300	0.0205	787.05	
	400	0.0107	643.87	0.7 / 99.3
	500	0.0215	460.33	
	600	0.0110	166.21	
	700	0.0132	92.34	
	800	0.0191	41.72	

Table 6: The factors that change in the measurements of Fe_2O_3 nanoparticles in all the range of temperature are presented in that table.

H.T. Booster		**Field Controller**		**Lock-In Modulation Amplifier**					**Bridge**
Temperature (K)	***N_2 flow***	***Field Center (G)***	***Sweep Width (G)***	***Modulation Amplitude (V)***	***Frequency (kHz)***	***phase (°)***	***Sensitivity (mV)***	***Time Constant (ms)***	***MW power source (dB)***
300	0	3400	5000	1.552	100	180	1000	10	16
350	2	3400	5000	1.552	100	180	1000	10	16
400	3	3400	5000	1.552	100	180	1000	10	16
450	3	3400	5000	1.552	100	180	1000	10	16
500	4	3400	5000	1.552	100	180	1000	10	16
550	4	3400	5000	1.552	100	180	1000	10	16
600	4	3400	5000	1.552	100	180	1000	10	16
650	5	3400	5000	1.552	100	180	1000	10	17
700	5	3400	5000	1.552	100	180	1000	10	17
750	5	3400	5000	1.552	100	180	1000	10	17
800	5	3400	5000	1.552	100	180	1000	10	17

Table 7: The settings for all H.T. EPR components are in this Table for the measurements for ferromagnetic Fe_2O_3 nanoparticles in all the range of the temperature.

Summary #2

Those models, from the beginning, considered that the magnetic moment would follow an Arrhenius law, with a characteristic relaxation time τ_1. Nevertheless, the determination of τ_1 was solved by Néel [63] in 1949. He supposed that each nanoparticle was formed by rigidly aligned spins that rotate coherently during magnetization reversal, considering the case of uniaxial anisotropy when the energy barrier is much larger than the thermal energy of the system. Characteristic time relaxation to be of the order of 10^{-10} s. When the size of a particle composed by magnetic atoms is small enough, the energy necessary to divide itself into magnetic domains is higher than the energy needed to remain as a single magnetic domain, or monodomain [57]. The magnetic properties of an assembly of monodomain particles is studied within the framework the so-called superparamagnetic theory, in analogy to paramagnetic systems. The first assumption of the superparamagnetic theory is to consider that all the magnetic moments within the particle rotate coherently, i.e., the net magnetic moment can be represented by an single classical vector, with magnitude $\mu = \mu_{at}N$, where μ_{at} is the atomic magnetic moment and N is the number of magnetic atoms that compose such particle. Significant changes in all three factors of importance have been observed. In intensity in line-width, in lineshape as a L/G factor. The change of intensity is a result of maximizing the difference of populations as we mentioned earlier, while the line-shape phenomenon is a result of merging and spin hopping.

4.5 CONLUSIONS

In this thesis a High Temperature EPR set-up completed successfully, with every part of it to be digitally controlled by the user via LabVIEW. This spectrometer can cover a very wide temperature range of 300K up to 1300K and take information about time relaxation, activation energy for multiple systems. Its an important tool in analyzing macroscopic and nanosized materials versus temperature. It is also unique in Greece and a very rare worldwide if we imagine that there are 5-8 in all Europe and around 3-5 in all US. In that thesis we also used it on two different applications, firstly with isolated spins in a matrix, where no spin dynamics phenomena

appear and secondly with ferromagnetic nanoparticles with spin domains and spin dynamics. More specifically we measured natural marble with macroscopic dimensions and we succeed on measuring Mn^{2+} ions transitions in a range from 300K up to 750K with a step of 25K. A spin larger than ½ its spectrum reflects interaction with the environment and temperature dependence of the EPR intensity and line-width changes has been examined and we observed that the wide spectrum in pretty much all the temperatures has a sextet of peaks of first order and five doublet forbidden transitions (m=-3/2, -1/2, 1/2, 3/2, 5/2), therefore we show the importance of a digitally-stable controlled High Temperature EPR. We also did an analysis of the first order transition, for the changes of intensity and linewidth changes versus temperature. In the (second) application of Fe_2O_3 we measured small sized ferromagnetic nanoparticles with spin domains. In those particles the phenomenon of superparamagnetism is appearing. Therefore, with the increase of the temperature all the factors of the line such as intensity, lineshape (L/G factor) and linewidth have changed respectively. The change of intensity is a result of maximizing the difference of populations as we mentioned earlier, while the line-shape phenomenon is a result of merging and spin hopping.

H.T. EPR is a novel tool with many perspectives in a lot of areas of interest such as soft materials. Some of those are in biological systems by measuring them in a temperature range from RT up to 400K, also in liquids, polymers, foams, gels, colloids, granular materials and generally in materials which can be easily deformed by thermal stresses or thermal fluctuations at about room temperature. Also, with HT EPR one can measure carbon-based material which have captured broad interest in many applications (like energy storage and conversion, sensors, enviromental) at a temperature range from RT up to 600K.

References

[1] W. . S. O. Gerlach, "No Title," *Z Phys*, no. 8, pp. 110–11, 1921.

[2] D. L. Fay, S. Akhavan, and V. M. Goldberg, "**済無**No Title No Title No Title," *Angew. Chemie Int. Ed. 6(11), 951–952.*, no. 465, pp. 106–111, 1967.

[3] W. . S. O. Gerlach, "No Title," *Z Phys*, no. 9, pp. 353–355, 1922.

[4] P. Zeeman, "The effect of magnetisation on the nature of light emitted by a substance," *Nature*, vol. 55, no. 1424. p. 347, 1897, doi: 10.1038/055347a0.

[5] Zeeman P., "Dr . P . Zeeman on the Influence of Magndlsm XXXII . On the Influence of Magnetism on the Nature of Light Emitted by a Substance," 1896.

[6] G. E. Uhlenbeck and S. Goudsmit, "Ersetzung der Hypothese vom unmechanischen Zwang durch eine Forderung bezüglich des inneren Verhaltens jedes einzelnen Elektrons," *Naturwissenschaften*, vol. 13, no. 47, pp. 953–954, 1925, doi: 10.1007/BF01558878.

[7] S. Uhlenbeck, G. E.; Goudsmit, "Zuschriften und vorl~iufige Mitteilungen," *Nature*, 1926.

[8] G. Breit and I. I. Rabi, "Mesurement of Nuclear Spin," *Phys. Rev.*, vol. 38, no. 11, p. 2082, 1931.

[9] B. H. Schultz, "A new method of measuring intensities of magnetization," *Physica*, vol. 6, no. 2, pp. 137–144, 1939, doi: 10.1016/S0031-8914(39)80004-0.

[10] E. Zavoisky, "Paramagnetic Relaxation of liquid solutions for perpendicular fields," *J Phys*, no. 9, p. 211, 1945.

[11] E. Zavoisky, "Paramagnetic Resonance Absorption of Microwaves," *J Phys*, no. 9, p. 245, 1945.

[12] E. M. Purcell, "Resonance Absorption by Nuclear Magnetic Moments in a Solid," *Phys. Rev*, vol. 69, 1946.

[13] and P. M. Bloch F, Hansen WW, "Nuclear Induction," *Phys. Rev.*, vol. 738, no. 69, p. 127, 1946.

[14] K. M. Salikhov and N. E. Zavoiskaya, "Zavoisky and the discovery of EPR," *Resonance*, vol. 20, no. 11, pp. 963–968, 2015, doi: 10.1007/s12045-015-0264-6.

[15] YOUNG WS, RASMUSSEN ST, and CUTLER IB, "Determination of an Effective

Viscosity of Powders As a Function of Temperature," pp. 185–202, 1968, doi: 10.1007/978-1-4684-2643-4_10.

[16] R. R. Ernst and W. A. Anderson, "Application of fourier transform spectroscopy to magnetic resonance," *Rev. Sci. Instrum.*, vol. 37, no. 1, pp. 93–102, 1966, doi: 10.1063/1.1719961.

[17] R. J. Blume, "Electron spin relaxation times in sodium-ammonia solutions," *Phys. Rev.*, vol. 109, no. 6, pp. 1867–1873, 1958, doi: 10.1103/PhysRev.109.1867.

[18] T. F. Prisner, "Pulsed High-Frequency EPR DESIGN FOR PULSED HIGH · FIELD EPR," pp. 249–276.

[19] N. J. Turro and J. Y.-C. Chen, "Nitroxides. Applications in Chemistry, Biomedicine, and Materials Science. By Gertz L. Likhtenshtein, Jun Yamauchi, Shin′ichi Nakatsuji, Alex I. Smirnov, and Rui Tamura.," *Angew. Chemie Int. Ed.*, vol. 47, no. 50, pp. 9596–9597, 2008, doi: 10.1002/anie.200885605.

[20] D. Hinderberger and G. Jeschke, "Site-Specific Characterization of Structure and Dynamics of Complex Materials by EPR Spin Probes," *ChemInform*, vol. 39, no. 34, pp. 1529–1537, 2008, doi: 10.1002/chin.200834276.

[21] M. Jeschke, G.; Pannier, "Double Electron-Electron Resonance," vol. 19, pp. 493–512, 2000.

[22] P. P. Borbat and J. H. Freed, "Double-Quantum ESR and Distance Measurements," vol. 19, no. B 1, pp. 383–459, 2002, doi: 10.1007/0-306-47109-4_9.

[23] G. Jeschke, "Determination of the nanostructure of polymer materials by electron paramagnetic resonance spectroscopy," *Macromol. Rapid Commun.*, vol. 23, no. 4, pp. 227–246, 2002, doi: 10.1002/1521-3927(20020301)23:4<227::AID-MARC227>3.0.CO;2-D.

[24] O. Schiemann and T. F. Prisner, "Long-range distance determinations in biomacromolecules by EPR spectroscopy," *Q. Rev. Biophys.*, vol. 40, no. 1, pp. 1–53, 2007, doi: 10.1017/S003358350700460X.

[25] C. Dockter *et al.*, "Refolding of the integral membrane protein light-harvesting complex II monitored by pulse EPR," *Proc. Natl. Acad. Sci. U. S. A.*, vol. 106, no. 44, pp. 18485–18490, 2009, doi: 10.1073/pnas.0906462106.

[26] D. Hinderberger, H. W. Spiess, and G. Jeschke, "Probing how counterion structure and dynamics determine polyelectrolyte solutions using EPR spectroscopy," *Appl. Magn. Reson.*, vol. 37, no. 1, pp. 657–683, 2010, doi: 10.1007/s00723-009-0082-7.

[27] B. K. L. Watkins G.D., "EPR Observation of the Isolated Intersitial Carbon Atom in Silicon," *Phys. Rev. Lett.*, vol. 36, no. 22, pp. 105–112, 2019.

[28] J. Stankowski, O. Huminiecki, and P. B. Sczaniecki, "Fullerene Science and Technology EPR of Graphite and Fullerenes," no. December 2012, pp. 37–41.

[29] T. D. Smith and J. R. Pilbrow, "The determination of structural properties of dimeric transition metal ion complexes from epr spectra," *Coord. Chem. Rev.*, vol. 13, no. 2–3, pp. 173–278, 1974, doi: 10.1016/S0010-8545(00)80255-6.

[30] B. R. Guduri and A. S. Luyt, "Structure and mechanical properties of polycarbonate modified clay nanocomposites," *J. Nanosci. Nanotechnol.*, vol. 8, no. 4, pp. 1880–1885, 2008, doi: 10.1166/jnn.2008.017.

[31] M. Francesca Ottaviani, X. G. Lei, Z. Liu, and N. J. Turro, "Supramolecular structure and dynamics of organic molecules adsorbed on the external surface of MFI zeolites. A direct and indirect computational EPR analysis," *J. Phys. Chem. B*, vol. 105, no. 33, pp. 7954–7962, 2001, doi: 10.1021/jp011110a.

[32] Z. Matuszak, K. J. Reszka, and C. F. Chignell, "Reaction of melatonin and related indoles with hydroxyl radicals: EPR and spin trapping investigations," *Free Radic. Biol. Med.*, vol. 23, no. 3, pp. 367–372, 1997, doi: 10.1016/S0891-5849(96)00614-4.

[33] C. L. Hawkins and M. J. Davies, "Detection and characterisation of radicals in biological materials using EPR methodology," *Biochim. Biophys. Acta - Gen. Subj.*, vol. 1840, no. 2, pp. 708–721, 2014, doi: 10.1016/j.bbagen.2013.03.034.

[34] D. T. Petasis and M. P. Hendrich, *Quantitative interpretation of multifrequency multimode EPR spectra of metal containing proteins, enzymes, and biomimetic complexes*, 1st ed., vol. 563. Elsevier Inc., 2015.

[35] W. Stachowicz, G. Burlińska, J. Michalik, A. Dziedzic-Goclawska, and K. Ostrowski, "Applications of EPR spectroscopy to radiation treated materials in medicine, dosimetry, and agriculture," *Appl. Radiat. Isot.*, vol. 44, no. 1–2, pp. 423–427, 1993, doi: 10.1016/0969-8043(93)90260-H.

[36] M. Polovka, V. Brezová, and A. Staško, "Antioxidant properties of tea investigated by EPR spectroscopy," *Biophys. Chem.*, vol. 106, no. 1, pp. 39–56, 2003, doi: 10.1016/S0301-4622(03)00159-5.

[37] A. Panchenko, H. Dilger, E. Möller, T. Sixt, and E. Roduner, "In situ EPR investigation of polymer electrolyte membrane degradation in fuel cell applications," *J. Power Sources*, vol. 127, no. 1–2, pp. 325–330, 2004, doi: 10.1016/j.jpowsour.2003.09.047.

[38] R. Malkin and A. J. Bearden, "Primary reactions of photosynthesis: photoreduction of a bound chloroplast ferredoxin at low temperature as detected by EPR spectroscopy.," *Proc. Natl. Acad. Sci. U. S. A.*, vol. 68, no. 1, pp. 16–19, 1971, doi: 10.1073/pnas.68.1.16.

[39] T. A. Yager and W. D. Kingery, "Laser-heated high-temperature EPR spectroscopy," *Rev. Sci. Instrum.*, vol. 51, no. 4, pp. 464–466, 1980, doi: 10.1063/1.1136246.

[40] M. J. N. Junk, "Electron Paramagnetic Resonance Theory," 2012. doi: 10.1007/978-3-642-25135-1_2.

[41] L. I. Schiff and H. Snyder, "Theory of the quadratic zeeman effect," *Phys. Rev.*, vol. 55, no. 1, pp. 59–63, 1939, doi: 10.1103/PhysRev.55.59.

[42] and G. R. E. Dave Barr, Sandra S. Eaton, "Workshop on Quantitative EPR," *31st Annu. Int. EPR Symp. Breckenridge, Color.*, p. 125, 2008.

[43] G. E. Brustolon M., *Electron paramagnetic resonance: A Practitioner's Toolkit*. Willey, 2009.

[44] J. H. Van Vleck, "The John-Teller effect and crystalline stark splitting for clusters of the form XY6," *J. Chem. Phys.*, vol. 7, no. 1, pp. 72–84, 1939, doi: 10.1063/1.1750327.

[45] N. Bloembergen, E. M. Purcell, and R. V. Pound, "Relaxation effects in nuclear magnetic resonance absorption," *Phys. Rev.*, vol. 73, no. 7, pp. 679–712, 1948, doi: 10.1103/PhysRev.73.679.

[46] F. Bloch, "Nuclear Induction," *Phys. Rev.*, vol. 70, pp. 4604–73, 1946.

[47] A. A. Manenkov, R. Orbach, and R. P. Hudson, " Spin-Lattice Relaxation in Ionic Solids ," *Phys. Today*, vol. 20, no. 7, pp. 88–88, 1967, doi: 10.1063/1.3034407.

[48] L. Sorin, *Electron Spin Resonance of Paramagnetic Crystals*. 1973.

[49] A. Pool, "2 Nuclear Spin Interactions in Solids (Sx)."

[50] R. de, "On the mechanism of paramagnetic relaxation," *Physica*, vol. 6, no. 1, pp. 33–43, 1939, doi: 10.1016/S0031-8914(39)90282-X.

[51] R. Orbach and P. R. S. L. A, "Spin-lattice relaxation in rare-earth salts," *Proc. R. Soc. London. Ser. A. Math. Phys. Sci.*, vol. 264, no. 1319, pp. 458–484, 1961, doi: 10.1098/rspa.1961.0211.

[52] C. P. Bean and J. D. Livingston, "Superparamagnetism," *J. Appl. Phys.*, vol. 30, no. 4, pp. S120–S129, 1959, doi: 10.1063/1.2185850.

[53] X. Q. Zhao, S. Veintemillas-Verdaguer, O. Bomati-Miguel, M. P. Morales, and H. B. Xu, "Thermal history dependence of the crystal structure of Co fine particles," *Phys. Rev. B - Condens. Matter Mater. Phys.*, vol. 71, no. 2, pp. 1–7, 2005, doi: 10.1103/PhysRevB.71.024106.

[54] E. C. Reynhardt, G. L. High, and J. A. Van Wyk, "Temperature dependence of spin-spin and spin-lattice relaxation times of paramagnetic nitrogen defects in diamond," *J. Chem. Phys.*, vol. 109, no. 19, pp. 8471–8477, 1998, doi: 10.1063/1.477511.

[55] R. Berger, J. C. Bissey, J. Kliava, H. Daubric, and C. Estournès, "Temperature dependence of superparamagnetic resonance of iron oxide nanoparticles," *J. Magn. Magn. Mater.*, vol. 234, no. 3, pp. 535–544, 2001, doi: 10.1016/S0304-8853(01)00347-X.

[56] E. Dormann and V. Jaccarino, "High temperature EPR linewidths in MnO and MnS," *Phys. Lett. A*, vol. 48, no. 2, pp. 81–82, 1974, doi: 10.1016/0375-9601(74)90409-5.

[57] R. Berger, J. Kliava, J. C. Bissey, and V. Baïetto, "Magnetic resonance of superparamagnetic iron-containing nanoparticles in annealed glass," *J. Appl. Phys.*, vol. 87, no. 10, pp. 7389–7396, 2000, doi: 10.1063/1.372998.

[58] R. Berger, J. C. Bissey, and J. Kliava, "Lineshapes in magnetic resonance spectra," *J. Phys. Condens. Matter*, vol. 12, no. 44, pp. 9347–9360, 2000, doi: 10.1088/0953-8984/12/44/315.

[59] J. Kliava and R. Berger, "Size and shape distribution of magnetic nanoparticles in disordered systems: computer simulations of superparamagnetic resonance spectra," *J. Magn. Magn. Mater.*, vol. 205, no. 2, pp. 328–342, 1999, doi: 10.1016/S0304-8853(99)00510-7.

[60] M. Mazúr, M. Valko, and H. Morris, "A simple alignment procedure for the precision

positioning of the sample at arbitrary points of the intracavity space of a TE104 double rectangular cavity," *Rev. Sci. Instrum.*, vol. 68, no. 6, pp. 2514–2517, 1997, doi: 10.1063/1.1148151.

[61] W. T. Park RM, Carroll RM, Bliss P, Burns GW, Desmaris RR, Hall FB, Herzkovitz MB, MacKenzie D, McGuire EF, Reed RP, Sparks LL, *Manual on the Use of Thermocouples in Temperature Measurement: 4th Edition*. 1993.

[62] T. K. Sharma, Om P.; Bhat, "DPPH antioxidant assay revisited.," *J. Food Chem.*, vol. 113, no. 4, pp. 1202–1205, 2009.

[63] Neel L., "Influence des fluctuations thermiques sur l' aimantation de grains ferromagnetiques tres fins," *Comptes Rendus Hebd. Des Seances L Acad. Des Sci.*, vol. 228, no. 8, pp. 664–666, 1949.